学位論文

Measurement of Charged-Current e^+p Deep Inelastic Scattering Cross Sections at $\sqrt{s}=300\,\mathrm{GeV}$

重心系エネルギー300 GeVにおける陽電子・陽子
荷電非弾性散乱断面積の測定

長坂 邦浩

東京都立大学大学院理学研究科物理学専攻

平成10年12月博士(理学)申請

Measurement of Charged-Current e^+p Deep Inelastic Scattering Cross Sections at $\sqrt{s} = 300$ GeV

Kunihiro Nagano

Graduate school
University of Tokyo

Submitted in partial fulfillment
of the requirements for the degree of
Doctor of Science

December 21, 1998

Abstract

The cross sections for the charged current e^+p deep inelastic scattering were measured at $\sqrt{s} = 300\,\mathrm{GeV}$ in the kinematic region $Q^2 > 200\,\mathrm{GeV}^2$. The analysis is based on the $46.6\,\mathrm{pb}^{-1}$ collision data collected by the ZEUS experiment during the running period 1994 to 1997.

The single differential cross sections $d\sigma/dQ^2$, $d\sigma/dx$, and $d\sigma/dy$ were measured. Compared with our previous measurement, both the statistical and systematic errors were reduced. The explored kinematic region has been extended to high Q^2 and high x. The $d\sigma/dQ^2$ was measured up to $Q^2 = 30000\ \mathrm{GeV}^2$ and the $d\sigma/dx$ was measured up to $x = 0.65$.

The double differential cross sections in terms of x and Q^2, $d^2\sigma/dxdQ^2$, were measured. This is the first measurement for e^+p charged current interaction. This kinematic region($Q^2 > 200\,\mathrm{GeV}^2$) has never been explored either by the fixed-target neutrino-beam experiments.

The measured cross sections were compared with the Standard Model predictions obtained using the CTEQ4D, MRSA, and GRV94 parton densities(PDFs) which are evolved according to the Next-to-Leading-Order(NLO) QCD DGLAP equation. The cross sections were consistent with the predictions except for the high x region, $x > 0.1$. The $d\sigma/dx$ exhibited an excess at $x > 0.1$ and the $d^2\sigma/dxdQ^2$ exhibited an excess at high x in a wide range of Q^2. It suggests that the d-quark at high x might be too underestimated in the current parton densities.

The propagator mass was extracted from the measured $d\sigma/dQ^2$ as $M_W = 83.4 \pm 2.8(stat.)\ ^{+1.6}_{-2.1}\ (syst.) \pm 2.7(pdf)\,\mathrm{GeV}$. The value was in agreement with the direct mass measurement at LEP and Tevatron.

Contents

Chapter 1

INTRODUCTION

It is a fundamental interest for human beings to understand the constituents of the world. In today's particle physics view, the world is built of the leptons and quarks [1]. Interactions between them are described by the framework of the gauge field theory. The interactions are mediated by quanta of the gauge field which ensure the local symmetry under the gauge transformation and regulate the property of the interactions in turn. Besides the gravity which we can neglect to be weak in our energy scale, there are three known forces; the electro-magnetic, the weak, and the strong interactions. The electro-magnetic and weak interactions are unified within the Electro-Weak(EW) theory formulated by Glashow, Salam and Weinberg [2]. The strong interaction is described by the Quantum Chromodynamics(QCD), a non-Abelian gauge theory. The combination of the EW theory and the QCD is called as the Standard Model(SM) of today's particle physics.

Scattering experiments provide a way to investigate the structure of an object. Even in our day-life, we are detecting scattered light with our eyes. This type of experiment has contributed much to the particle physics. An example is given by the experiment by Rutherford early in this century. Alpha particles injected on a metal foil were scattered occasionally at large angle. The result led to the discovery of the nucleus. Spatial resolution of the scattering process is determined by the four momentum transferred from the probe Q; the typical size that can be probed is the Compton wavelength(h/Q) of the exchanged particle which mediates the interaction. The smaller spatial resolution is achieved by the larger momentum transfer and hence by the higher energetic collisions.

The proton is the most stable particle among hadrons, and thus was thought first to be an elementary particle together with leptons. However, there were some indications of non point-like feature or structure of the proton. Historically the observation of the anomalous magnetic moment already suggested that the proton has an internal structure. Also, the existence of the resonance state of the nucleon was found in πN scattering, and electron-proton elastic scattering experiment with beam energies of the order of 1 GeV measured the proton form factor, the electric

charge distribution of the proton, as to be 0.8 fm [4]. This led to an idea of composite nucleon model based on 3 fundamental particles by the Sakata group. In the early '60s, the hadrons were known to be well classified under the SU(3) symmetry as postulated by Gell-Mann and Ne'eman. Then, the quarks as the constituents of hadrons were proposed in 1964 independently by Gell-Mann and Zweig as a way of generating the SU(3) separating scheme [3].

The point-like constituents of the proton was first addressed by the SLAC-MIT experiment in the late 60's [5]. They injected 20 GeV electrons to the proton. Unexpected results came out from the deep inelastic scattering(DIS) in which the proton is completely broken up with the high energy electron beam. The first surprise was that the deep inelastic cross section showed only a weak fall off as a function of Q^2. This was contrary to the expectation from the form factor. The most striking result followed after the suggestion of Bjorken [6]. In this deep inelastic region, the structure of the proton can be expressed by the structure functions F_1 and F_2 as a function of two Lorentz invariant variables; usually by the negative of the four momentum transfer squared Q^2, and the Lorentz invariant energy transfer ν. However, the structure functions were found to scale with the Bjorken variable x as defined as the ratio of the Q^2 and ν. This Bjorken scaling established the parton model which explains the deep inelastic scattering as an incoherent sum of the elastic scattering between the electron and the point-like partons which constitute the proton. The Bjorken variable x is interpreted as the momentum fraction of the interacting parton. Callen and Gross pointed out that if the partons have spin-$\frac{1}{2}$, $R \equiv \sigma_L/\sigma_T = 0$ holds, i.e. the ratio of photoabsorption cross sections of longitudinal(σ_L) and transverse(σ_T) virtual photons becomes zero [7]. The experiment resulted in small R. Partons were thus identified as the quarks, leading to the quark-parton model(QPM). Later observation of the logarithmic violation of the Bjorken scaling and of that charged partons carry one half of the proton momentum led the QPM to the QCD, which has the feature of asymptotic freedom, i.e. quarks behave like free particles in the high Q^2 scattering. The remaining half of the proton momentum is attributed to gluons. The strong interactions between partons including gluons violate the Bjorken scaling.

Experiments using high energy neutrino beams as a probe has also been performed aiming at probing the proton by means of weak interaction so that quarks and anti-quarks are distinguished. In 1973, the weak-neutral current interaction was discovered by the Gargemelle collaboration [8]. The unification of electromagnetic and the weak interactions as the EW theory was thus verified. Finally, the intermediates of the weak interactions $W^{\pm}$ and Z^0 were discovered at the CERN proton-antiproton collider.

In '80s, the lepton-nucleon scattering experiments were dedicated to measure the structure of the proton with higher beam energy [9, 10, 11]. The weak structure function of the proton was measured by neutrino-proton scattering experi-

ments [12, 13, 14, 15, 16]. The structure functions are written in terms of parton densities in the proton and their couplings to the gauge boson. The Q^2 dependence of structure functions is expressed as that the parton densities "evolve" with Q^2. QCD can predict how the evolution goes with an equation derived based on the factorization theorem. This formalism is equivalent to a leading log approximation to take leading log terms to all orders. Obtained structure functions from those experiments proved that the proton structure is well described with the parton densities evolved according to the more refined next to leading order QCD evolution equation.

Colliding two beams is the most effective way to step up the scattering energy in order to improve the resolution. HERA is the first collider of electrons and protons. There are two experiments, H1 and ZEUS, at HERA. HERA started the operation with electron-proton collision since May 1992. Since summer 1994, HERA has operated with positron-proton collision. The beam energies were 27.57 GeV for positron and 820 GeV for proton. The center of mass energy of positron-proton collision is 300 GeV, which corresponds to lepton beams with energy of about 50 TeV injecting to a fixed target. The integrated luminosity accumulated by ZEUS is $0.82\,\mathrm{pb}^{-1}$ for e^-p and $46.6\,\mathrm{pb}^{-1}$ for e^+p collisions, respectively.

The large center-of-mass energy of the collision allows a study on the proton structure in a wide kinematic range [17, 18]. The x and Q^2 regions are extended by two orders of magnitude. Both H1 and ZEUS collaborations extracted the structure function F_2 from the data taken in 1992 and 1993 [19, 20]. The strong rise of F_2 in low x region was observed, which simulated a lot of theoretical activities.

In high Q^2 region, both of the EW contributions become visible. The effects of the Z^0 exchange and its interference between γ appear at Q^2 greater than several thousands GeV^2 in the neutral current processes; $ep \to eX$. The charged current process mediated by $W^{\pm}$ boson; $ep \to \nu X$, is first accessible in electron-proton collision. In 1996, both H1 and ZEUS collaborations observed an excess of event rates of the neutral current in the very high Q^2 regions of $Q^2 \gtrsim 15000\,\mathrm{GeV}^2$ with the e^+p data sample collected in 1994-1997 [21, 22]. Possibilities to interpret the excess as an indication of a new physics were discussed both from theoretical and experimental aspects [23]. This may enlarge physics interests of charged current reaction in a corresponding Q^2 region [24, 25, 26], although significance of the excess in neutral current process has decreased in the most recent analysis adding the collisions taken in the year of 1997 [27].

Both H1 and ZEUS collaborations measured the charged current cross section in e^-p and e^+p collisions based on the data taken up to 1994 [28, 29, 30]. The corresponding luminosity of the ZEUS(H1) measurement was 0.27(0.36) and 2.93(2.70) pb^{-1} for e^-p and e^+p, respectively. The cross section showed a dump in high Q^2 region due to the effect of the propagator(W-boson) mass. The extracted mass of the W-boson from this Q^2 dependence of the cross section was in agreement with

the value obtained by direct measurements at LEP and Tevatron. It was the first measurement with finite value in space-like exchange, and is complementary to those direct measurements. Also, a comparison of the Q^2 dependence of the neutral and charged current cross sections was made both collaborations [31, 32]. The result was in agreement with the SM predictions within statistical errors.

In this paper, we present the measurement of the e^+p deep inelastic charged current cross sections in the kinematic region of $Q^2 > 200\,\mathrm{GeV}^2$. The analysis is based on the whole $46.6\,\mathrm{pb}^{-1}$ e^+p data collected by the ZEUS collaboration during the running period from 1994 to 1997, which is 15 times larger than our previous analysis. The large data set allows us not only to derive single differential cross sections as functions of Q^2, x, and y with high precision, but also to measure the double differential cross sections in (x, Q^2), which is the first measurement in this kinematic region.

Following this introduction, the formalism of the deep inelastic scattering is described in the chapter 2. After dedicating the chapter 3 for the description of HERA, the ZEUS detector and the MC simulation, the reconstruction of the kinematics and the event selection in offline analysis are presented in the chapter 4 and 5, respectively. An overview of the method for the cross section measurement used in the analysis is described in the chapter 6. Systematic uncertainties on our measurement are discussed and evaluated in the chapter 7 to present the results in the chapter 8. Our conclusion can be found in the chapter 9.

Chapter 2

DEEP INELASTIC SCATTERING

2.1 Kinematics

First, let us consider a general case that a lepton l with four momentum k collides on a nucleon N with mass m_N and four momentum p. The lepton scatters away(sometimes by being changed to another lepton l') with four momentum of k'. The nucleon becomes a hadronic system X with four momentum of p_h

$$l(k)N(p) \rightarrow l'(k')X(p_h). \tag{2.1}$$

Figure 2.1 shows a schematic diagram of the reaction.
The reaction is mediated by the gauge bosons, γ, Z or W. The four momentum of the exchanged gauge boson(q), i.e. the four momentum transfer of the reaction, is

$$q \equiv k - k' = p_h - p. \tag{2.2}$$

The negative of the four momentum transfer squared(Q^2) is often used to describe the DIS process

$$Q^2 \equiv -q^2. \tag{2.3}$$

Inelasticity of the lepton(y) is defined as;

$$y \equiv \frac{p \cdot q}{p \cdot k}. \tag{2.4}$$

The meaning of y is straightforward in the nucleon's rest frame. It corresponds to a fractional energy transfer to the nucleon. By definition, y takes in the range from 0 to 1.
Bjorken scaling variable x is defined as:

$$x \equiv \frac{Q^2}{2p \cdot q} = \frac{Q^2}{(p+q)^2 - p^2 - q^2} = \frac{Q^2}{(W^2 - m_N{}^2) + Q^2}, \tag{2.5}$$

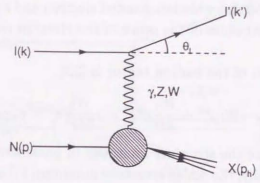

Figure 2.1: A schematic diagram of lepton-nucleon DIS. Scattering angle of the lepton θ_l is defined as shown in the figure throughout this paper.

where W is the mass of the hadronic system X, i.e. $W^2 \equiv {p_h}^2$. x is in the range from 0 to 1 since $W > m_N$ in the above equation. These three variables are usually used to describe the kinematics of DIS process with combinations of e.g. (x, Q^2) or (x, y). They are related each other with a simple formula by neglecting the masses of the lepton and the nucleon,

$$Q^2 = x \cdot y \cdot s, \tag{2.6}$$

where s is the square of the center of mass energy,

$$s \equiv (p+k)^2. \tag{2.7}$$

The energy transfer in the nucleon's rest frame(ν) is defined as:

$$\nu \equiv \frac{p \cdot q}{m_N}. \tag{2.8}$$

2.2 Scattering cross sections

The unpolarized lepton-nucleon deep inelastic scattering cross section can be generalized to

$$d\sigma \sim L_{\mu\nu} \cdot W^{\mu\nu}, \tag{2.9}$$

i.e. factorized into the lepton tensor $L_{\mu\nu}$ and the hadron tensor $W^{\mu\nu}$. The $L_{\mu\nu}$ is the tensor associated to the lepton vertex, and the hadron tensor $W^{\mu\nu}$ serves to describe the structure of the hadron.

For the charged-current DIS process in electron(or positron)-proton collisions, the lepton tensor is written as:

$$L_{\mu\nu} \equiv [\overline{\nu_L}(k')(1-\gamma_\mu^5)e_L(k)][\overline{\nu_L}(k')(1-\gamma_\nu^5)e_L(k)]^* \tag{2.10}$$

$$= k_\mu k'_\nu + k'_\mu k_\nu - g_{\mu\nu} k \cdot k' \pm \varepsilon_{\mu\nu\alpha\beta} k^\alpha k'^\beta \tag{2.11}$$

with the upper and lower signs for the left-handed electron and right-handed positron beam, respectively. Contribution of the order of the electron mass was neglected in the above equation.

The general expression of the hadron tensor is [33]

$$W^{\mu\nu} \equiv -W_1 g^{\mu\nu} + \frac{W_2}{M^2} p^\mu q^\nu - i\frac{W_3}{2M^2}\varepsilon^{\mu\nu\alpha\beta} p_\alpha q_\beta, \tag{2.12}$$

where W_1, W_2, and W_3 are the structure functions to parameterize the structure of the proton.[1] Conventionally, the scaled structure functions(F_i) are used; $F_1 = MW_1$, $F_2 = \nu W_2$, and $F_3 = \nu W_3$.

The cross section of the DIS charged current process $e^\pm p \to \overline{\nu} X$ is expressed by contracting $L_{\mu\nu} W^{\mu\nu}$,

$$\begin{aligned} \frac{d^2\sigma}{dxdQ^2} &= \frac{{G_F}^2}{4\pi x}\left(\frac{{M_W}^2}{{M_W}^2+Q^2}\right)^2 \times \{Y_+(y){F_2}^{CC}(x,Q^2) \\ &- y^2{F_L}^{CC}(x,Q^2) \mp Y_-(y)x{F_3}^{CC}(x,Q^2)\}, \end{aligned} \tag{2.13}$$

where M_W is $W^\pm$ boson mass, and G_F is the Fermi coupling constant. The upper(lower) sign is for the positron(electron) beam. The kinematic factor $Y_\pm$ is given with

$$Y_\pm(y) = 1 \pm (1-y)^2. \tag{2.14}$$

The longitudinal structure function F_L appeared in the above cross section formula is defined as $F_2 - 2xF_1$. The F_L owes the cross section due to an exchange of a longitudinally polarized gauge boson. Hence $F_L = 0$ in the lowest order. The F_3 is the parity violating term. The interference between vector and axial-vector coupling interference is given by this term. The sign changes in the equation 2.13 for electron($-$) and a positron($+$).

Similarly, the DIS cross section for the neutral current $e^\pm p \to e^\pm X$ is written as:

$$\begin{aligned} \frac{d^2\sigma}{dxdQ^2} &= \frac{2\pi\alpha^2}{xQ^4} \times \{Y_+(y){F_2}^{NC}(x,Q^2) \\ &- y^2{F_L}^{NC}(x,Q^2) \mp Y_-(y)x{F_3}^{NC}(x,Q^2)\}, \end{aligned} \tag{2.15}$$

where α is the electromagnetic fine structure constant. The parity violating term F_3 is mainly due to the γ-Z^0 interference. The upper(lower) sign is for the positron(electron).

[1] The contribution from W_4, W_5 and W_6 terms; $\frac{W_4}{M^2}q^\mu q^\nu$, $\frac{W_5}{M^2}(p^\mu q^\nu + q^\mu p^\nu)$, and $\frac{W_6}{M^2}(p^\mu q^\nu - q^\mu p^\nu)$ are dropped since they contribute only to the order of the electron mass.

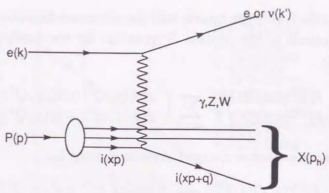

Figure 2.2: A schematic diagram of electron-proton DIS in view of the QPM. The parton i which carries momentum of xp interacts with the electron via the gauge bosons, γ, Z or W.

2.3 The QCD parton model

2.3.1 Quark Parton Model

In the parton model, the deep inelastic scattering(equation 2.1) is regarded as an incoherent sum of elastic scattering of partons of which the proton consist as indicated in figure 2.2. In this picture, the reaction is described by

- the parton density(or, momentum distribution of partons) in the proton, and
- the interaction between the parton and electron.

First of all, the Bjorken variable x in the previous section is interpreted as the fraction of the momentum of the interacting parton with respect to that of the parent proton. To see this, let us denote the momentum fraction as η. After scattering with the electron, the parton has the four momentum of $q' = \eta p + q$;

$$q'^2 = (\eta p + q)^2, \tag{2.16}$$
$$= \eta^2 {m_P}^2 + 2\eta p\cdot q - Q^2, \tag{2.17}$$
$$= {m_q}^2, \tag{2.18}$$

from the assumption of the elastic scattering. By neglecting the parton and proton masses, m_P and m_q,

$$\eta = \frac{Q^2}{2p\cdot q} = x. \tag{2.19}$$

The momentum distribution of the parton in the proton is expressed as $xq(x,Q^2)$, where $q(x,Q^2)$ is the parton density function(PDF). In the Quark Parton Model(QPM),

the parton is identified with the quark, and the structure functions are written with the quark distributions in the proton. Expression for the positron-proton charged current process is:

$$\begin{pmatrix} {F_2}^{CC}(x,Q^2) \\ x{F_3}^{CC}(x,Q^2) \end{pmatrix} = \sum_{i=1,2} \begin{pmatrix} x[d_i(x,Q^2) + \overline{u_i}(x,Q^2)] \\ x[d_i(x,Q^2) - \overline{u_i}(x,Q^2)] \end{pmatrix}, \tag{2.20}$$

and the one in electron-proton charged current process is:

$$\begin{pmatrix} {F_2}^{CC}(x,Q^2) \\ x{F_3}^{CC}(x,Q^2) \end{pmatrix} = \sum_{i=1,2} \begin{pmatrix} x[u_i(x,Q^2) + \overline{d_i}(x,Q^2)] \\ x[u_i(x,Q^2) - \overline{d_i}(x,Q^2)] \end{pmatrix}. \tag{2.21}$$

The u_i is the PDF of the up-type quarks(u, c), and d_i is the PDF of the down-type quarks(d, s) with i running in the two generations. Here we have assumed that there is no significant contribution from t and b quarks in the proton. Also we have assumed that the considering energy is higher than the thresholds for the production of c quark.

Inserting equations 2.20 and 2.21 into the equation 2.13, one gets the cross section as:

$$\frac{d^2\sigma}{dxdQ^2} = \frac{{G_F}^2}{2\pi}\left(\frac{{M_W}^2}{{M_W}^2+Q^2}\right)^2 \times \sum_{i=1,2}[\overline{u_i}(x,Q^2) + (1-y)^2 d_i(x,Q^2)], \tag{2.22}$$

for the positron, and as:

$$\frac{d^2\sigma}{dxdQ^2} = \frac{{G_F}^2}{2\pi}\left(\frac{{M_W}^2}{{M_W}^2+Q^2}\right)^2 \times \sum_{i=1,2}[u_i(x,Q^2) + (1-y)^2 \overline{d_i}(x,Q^2)]. \tag{2.23}$$

for the electron. Figure 2.3 shows the cross sections of electron-proton and of positron-proton DIS both predicted by the SM and measured by HERA experiments before 1995. As shown in the figure, the charged current cross section in e^-p is higher than that in e^+p. There are two reasons; first of them is due to that the density of the u-quark is in general larger than that of the d-quark in the proton. Since the charged current process selects the weak isospin, electrons(positrons) can interact only with positively(negatively) charged quarks. The difference becomes larger at higher Q^2 region as a reflection of larger contribution from quarks with higher x.

The kinematic suppression factor $(1-y)^2$ in the cross sections is a reflection of the V-A nature of the weak interaction. The scattering angle of the electron in the center of mass frame of the electron-quark system, θ^* [2], is related to y with $1-y = \frac{1+\cos\theta^*}{2}$. The helicity conservation imposes an isotropic scattering angle

[2]The angle is defined in the same manner as indicated in the figure 2.1.

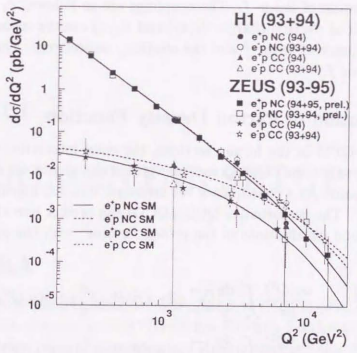

Figure 2.3: NC and CC $d\sigma/dQ^2$ both in electron- and positron-proton collisions.

distribution for the electron and quark(or positron and anti-quark), whereas a dependence proportional to $\frac{(1+\cos\theta^*)^2}{2} = (1-y)^2$ for the electron and anti-quark(or positron and quark) elementary process. Then, the anti-quarks suffer from the suppression with the electron beam while the quarks suffer from it with the positron beam. This is the other reason of the higher cross section in the electron-proton collisions.

In neutral current DIS process, the structure functions include the couplings of quarks to the gauge bosons, apart from the fine structure constant, as [34]:

$$\begin{pmatrix} {F_2}^{NC}(Q^2) \\ x{F_3}^{NC}(Q^2) \end{pmatrix} = \sum_f \begin{pmatrix} xq_f{}^+[e_f{}^2 - 2e_f v_f v_f \chi_Z + (v_f{}^2 + a_f{}^2)(v_e{}^2 + a_e{}^2)\chi_Z{}^2] \\ xq_f{}^-[-2e_f a_f a_e \chi_Z + 4v_e v_f a_f \chi_Z{}^2] \end{pmatrix} \tag{2.24}$$

with

$$q_f{}^{\pm} = q_f(x,Q^2) \pm \overline{q_f}(x,Q^2), \tag{2.25}$$

$$\chi_Z = \frac{1}{4\sin\theta_W{}^2\cos\theta_W{}^2}\frac{Q^2}{Q^2+{M_Z}^2}. \tag{2.26}$$

Here M_Z is the mass of the Z^0 boson, and θ_W is the Weinberg angle. The upper sign is for positron and the lower sign is for electron. $q_f(\overline{q}_f)$ is the quark(anti-quark)

density in the proton of flavor f. The couplings are as follows. e_f is the electric charge in the unit of electron charge. $v_f(a_f)$ and $v_e(a_e)$ are the vector(axial-vector) coupling of the quark of flavor f and the electron, respectively. The sum is taken for all quark flavor f.

2.3.2 Evolution of Parton Density Function

In the naive QPM in the former sections, the color interaction of the partons were not taken into account. Quarks can emit gluons and gluons can split into quark and anti-quark pairs. As a consequence the structure function depends not only on x but also on Q^2. The perturbative QCD(pQCD) can predict how the quark q and gluon g momentum distributions in the proton "evolve" with the interaction scale Q^2.

$$\frac{dq_i(x,Q^2)}{d\ln Q^2} = \frac{\alpha_s(Q^2)}{2\pi}\int_x^1 \frac{dy}{y}[\sum_j q_j(y,Q^2)P_{q_iq_j}(\frac{x}{y}) + g(y,Q^2)P_{q_ig}(\frac{x}{y})] \quad (2.27)$$

$$\frac{dg(x,Q^2)}{d\ln Q^2} = \frac{\alpha_s(Q^2)}{2\pi}\int_x^1 \frac{dy}{y}[\sum_j q_j(y,Q^2)P_{gq_j}(\frac{x}{y}) + g(y,Q^2)P_{gg}(\frac{x}{y})] \quad (2.28)$$

This is known as the Dokshitzer-Gribov-Lipatov-Altarelli-Parisi(DGLAP) equation [35]. The splitting function P_{ij} describes the probability of finding parton i inside the parton j with momentum fraction of x/y.

2.4 Electro-Weak correction

The Born level cross section in the former sections is corrected for the Electro-Weak higher order effects. The corrections are the virtual correction associated with the leptonic vertex and the non-infra-red real photon emission from initial state electron. The measured cross section can be expressed as:

$$\frac{d\sigma^{rad}}{dv} = \int dv' K(v;v')\frac{d\sigma^{Born}}{dv'}. \quad (2.29)$$

The vector v denotes the kinematic variables (x,Q^2). $K(v;v')$ is the radiative kernel. We call the $d\sigma^{rad}/dv$ as radiative cross section. The Born level cross sections were obtained in this paper taking into account these effects.

Chapter 3

EXPERIMENTAL SETUP

3.1 HERA

HERA(Hadron Elektron Ring Anlage) is the first electron-proton colliding accelerator. It was constructed at DESY(Deutches Elektron Synchrotron) in Hamburg, Germany. Principal design parameters are summarized in Table 3.1. One characteristics of HERA beams is the short bunch crossing time(96 nsec) with up to 220 colliding bunches aimed for high luminosity. The center of mass energy of ep collisions is 314 GeV with the electrons of 30 GeV and with the protons of 820 GeV. The maximum reachable Q^2 is 98000 GeV^2 which is higher than those of the previous fixed target experiments by two orders of magnitude.

A schematic layout is shown in Figure 3.1. There are four experimental area. Two of them are dedicated to colliding experiments, the H1 and ZEUS, which locate at the Hall North and Hall South, respectively. The other two are fixed target experiments. HERMES(Hall East) study the nuclear spin structure using the electron beam. HERA-B(Hall West) is a future experiment aimed on b-quark physics using the proton beam.

Electrons and protons are pre-accelerated in the following steps. The electrons(or positrons) are accelerated by a linear accelerator LINAC, by a synchrotron DESY II(to 6 GeV), and by PETRA III(to 14 GeV). The protons from the negative hydrogen ions are accelerated by a linear accelerator, by DESY III(to 7.5 GeV) and by PETRA II(to 40 GeV). These pre-accelerators are also shown in Figure 3.1.

HERA started its operation in May 1992 with electron beams and switched to positron beams to increase the luminosity in August 1994. [1] Since then, HERA has been operated with positrons up to 1997 running period.

Figure 3.2 shows the integrated luminosity of the positron-proton collision data collected by ZEUS during the running period 1994 to 1997. (The luminosity mea-

[1] The electron beams had short lifetimes due to the positively ionized dust in the accelerator ring.

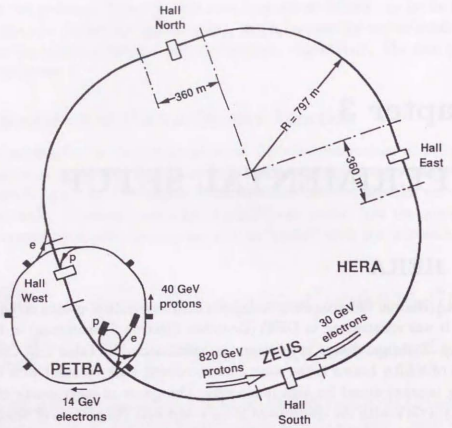

Figure 3.1: Layout of the HERA collider.

Table 3.1: HERA design parameters [17].

	electron ring	proton ring
circumference	6336 m	
nominal energy	30 GeV	820 GeV
c.m. energy	314 GeV	
circulating current	60 mA	160 mA
number of particles/beam	0.8×10^{13}	2.1×10^{13}
number of bunch packets	220	220
number of bunches	210	210
current/bunch	0.3 mA	0.8 mA
time between beam crossings	96 ns	
luminosity	$1.5 \times 10^{31} cm^{-2} s^{-1}$	
specific luminosity	$3.3 \times 10^{29} cm^{-2} s^{-1} mA^{-2}$	
polarization time at E_e=30 GeV	25 min.	

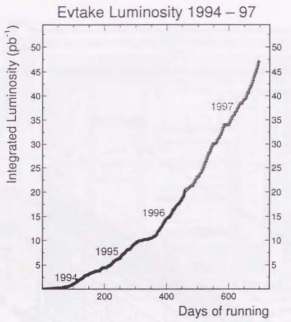

Figure 3.2: Integrated luminosity of e^+p collision data collected by ZEUS during 1994 to 1997.

surement is described in the section 3.4.) This analysis is based on whole of these 46.6 pb^{-1} positron-proton collision data.

3.2 ZEUS Detector

ZEUS [36] is a general-purpose detector for electron-proton collision experiment. It surrounds the interaction point nearly hermetically. A schematic view and a side view of the ZEUS detector are shown in Figures 3.3 and 3.4, respectively.

We define a coordinate system, which associates to the detector, as follows. The proton beam direction is defined to be the positive z direction with the origin at the nominal interaction point. The direction from the origin to the center of the HERA ring is defined as the positive x direction. Then, the y direction is defined according to right hand convention. We also call the proton(electron) beam direction, i.e. the positive(negative) z direction, as the forward(rear) direction. The polar angle θ is defined with respect to the positive z direction. The azimuthal angle ϕ is defined with respect to the positive x direction.

Situated at the most inner part is the tracking system which measures the charged particles' momenta. It consists of the central tracking detector(CTD), the

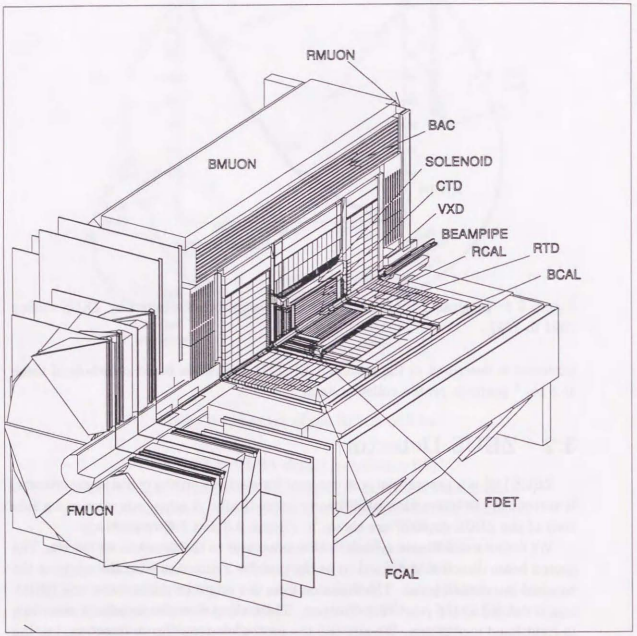

Figure 3.3: Layout of the ZEUS detector.

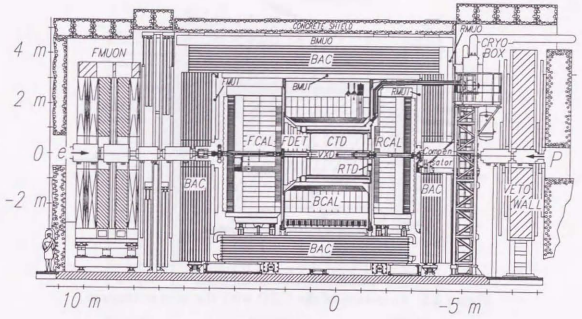

Figure 3.4: Side view of the ZEUS detector.

forward tracking detector(FDET), and the rear tracking detector(RTD). [2] Magnetic field of 1.43 T is provided by the superconducting solenoid magnet located outside the tracking system. The Uranium-Scintillator Calorimeter(CAL) surrounds the tracking detectors. The CAL is mechanically subdivided into three parts, forward calorimeter(FCAL), barrel calorimeter(BCAL), and rear calorimeter(RCAL). The asymmetric momenta of the electron and of the proton beams result in that the ZEUS detector was designed to have deeper calorimeters in the proton beam direction. The CAL is then surrounded by the backing calorimeter(BAC) inside a return yoke of irons which is also used as absorber. The muon tagging system, i.e. the barrel muon detector(BMUON), the rear muon detector(RMUON), and the forward muon spectrometer(FMUON), form the most outer layer. In this analysis, these muon chambers are used to reject the events induced by the cosmic ray or beam-halo muons coming outside the detector. The major components used in this analysis are described in detail in the following sections.

3.2.1 Central Tracking Detector(CTD)

The central tracking detector is a cylindrical drift chamber. It operates under high magnetic field(1.43 T) aimed for high resolution for high momentum tracks. This requires large Lorentz angle of 45°.

[2] The vertex detector(VXD) which had been located inner most was removed after 1995.

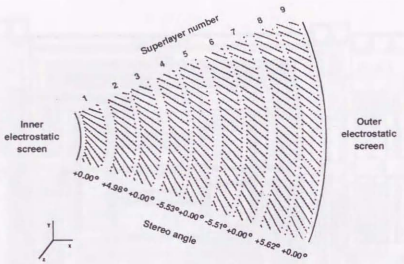

Figure 3.5: An octant of the CTD with the wire structures.

The wire configuration of an octant of the CTD is shown in Figure 3.5. The CTD consists of 9 superlayers(SL) each of which has 8 sense wire layers. Five SLs have wires parallel to the beam line and four SLs have wires with stereo angle of about 5 degree. The coverage of the SL1 is from 11.3° to 168.2° in the polar angle. The coverage of the outermost SL9 is limited as from 36.1° to 142.6°.

All the tracking information used in this analysis are provided by the CTD. The position resolution for a single track is given as 100-120 μm in $r\phi$ direction depending on the polar angle of the track, and is as 1.0-1.4 mm in z-direction measured by the stereo wires. The momentum resolution for tracks traversing all of the 9 SLs is $\sigma(p_T)/p_T = 0.005p_T + 0.016$ with p_T in GeV. Typical resolutions of the extrapolarated tracks to the CAL surface is 0.3 cm for high momentum tracks of $p_T > 5\,\mathrm{GeV}$.

3.2.2 Uranium-Scintillator Calorimeter(CAL)

The CAL was designed to have hermeticity with nearly full solid angle coverage and good hadronic energy resolution by achieving an equal response to the electromagnetic and hadronic particles, i.e $e/h = 1$.

Figure 3.6 shows a side view of the calorimeter together with the inner CTD and solenoid. The CAL covers polar angles from 2.2° to 176.5°. FCAL covers from 2.2° to 39.9°, BCAL covers from 36.7° to 129.1°, and RCAL covers from 128.1° to 176.5°. In total, it has 99.7% solid angle coverage.

Each calorimeter component is longitudinally divided into the electromagnetic(EMC) and hadronic(HAC) sections. The HAC section in FCAL and BCAL is subdivided

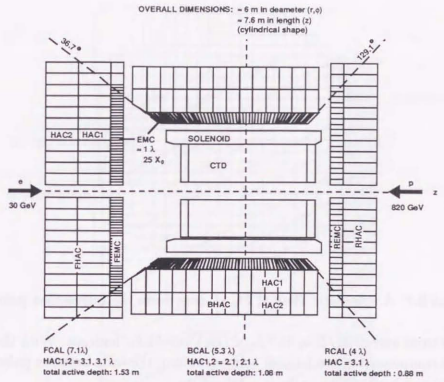

Figure 3.6: A side view of the calorimeter.

further into the HAC1 and the HAC2 sections. Each section consists of cells which are the smallest units of the calorimeter. The size of the cell is $5 \times 20\,\mathrm{cm}^2$($10 \times 20\,\mathrm{cm}^2$ in the RCAL) for the EMC and $20 \times 20\,\mathrm{cm}^2$ for the HAC sections; a HAC cell corresponds to 4(2 in the RCAL) EMC cells in its area. Each cell is made of layers of 3.3 mm thick depleted uranium plates and 2.6 mm thick scintillator plates. Scintillator lights are read out by two wavelength shifters and guided to two photomultiplier tubes.

The FCAL and RCAL have a similar structure. A schematic view of the FCAL as seen from the interaction point is shown in figure 3.7. They consists of 23 modules aligned transversely. Figure 3.8 shows the structure of a FCAL module. Each module is vertically segmented in 23 towers, each of which consists of four EMC, a HAC1 and a HAC2 cells (two EMC and a HAC cells in RCAL). The module number is assigned transversely from 1(left most in figure 3.7) to 23(right most in figure 3.7). The tower number is assigned vertically from 1(lower most in figure 3.7) to 23(upper most in figure 3.7).

The BCAL consists of 32 modules, which are almost projective to the interaction point. Each module is made of the wedge shaped towers aligned in z-direction. Each tower is segmented into four EMC, a HAC1, and a HAC2 cells.

The energy resolution under test beams conditions is $\sigma(E)/E = 18\%/\sqrt{E(\mathrm{GeV})} \oplus$

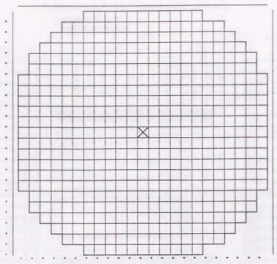

Figure 3.7: A schematic view of FCAL seen from the interaction point.

1% for electrons and $\sigma(E)/E = 35\%/\sqrt{E(\mathrm{GeV})} \oplus 2\%$ for hadrons. With the advantage of the compensation mechanism using uranium, the ratio between pulse heights of electrons and hadrons; i.e. e/h, is attained to:

$$e/h = 1.00 \pm 0.03. \tag{3.1}$$

The timing resolution is less than 1 nsec for energy deposits greater than 4.5 GeV.

3.3 Trigger and Data Acquisition System

The short interval(96 ns) of the HERA colliding bunches and the large size of the event record(10 KB/event) define the requirements for the ZEUS trigger and data acquisition system.

In such a short interval, it is impossible to make a trigger decision. To avoid long dead time, ZEUS adopted a synchronized pipeline readout system. This was the first attempt in high energy experiments.

The large event record requires a high background reduction. The output rate is limited to about 5 Hz, however, the background rate reaches to order of 100 KHz mainly due to interactions between the proton and gas molecule in the beam pipe. To cope with it, ZEUS adopted three level trigger system, FLT(First Level Trigger), SLT(Second Level Trigger), and TLT(Third Level Trigger). The data flow in the ZEUS trigger system is diagramed in Figure 3.9.

3.3.1 First level trigger

The task of the FLT is to reduce the rate to 1 KHz from the 10 MHz bunch crossing rate. This output rate is limited by the size of the digital buffer. (See the

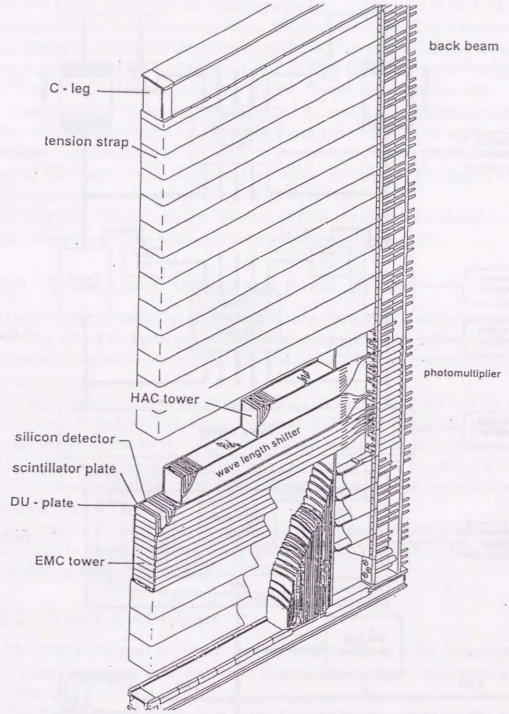

Figure 3.8: Structure of a FCAL module.

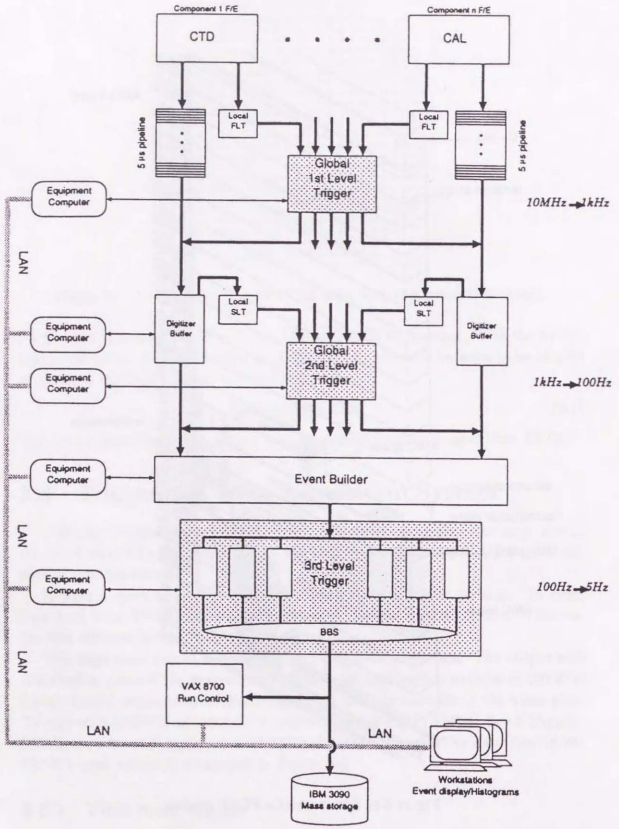

Figure 3.9: A diagram of the data flow in the trigger system.

next section.)

The FLT is devided into the component FLTs and the Global First Level Trigger(GFLT). Each component FLT is designed to send trigger data to the GFLT in 26 crossing intervals. In order to be provided in such a short time, these data are coarse, for example, the calorimeter first level trigger(CFLT) picks 5% of analog data for the trigger signal. Information available at FLT are for example CAL activities($\not{H}_T{}^{FLT}$, $E_T{}^{FLT}$ etc. [3]), CTD tracks(good_TRK^{FLT} etc. [4]), and muon chamber hits.

Then the GFLT makes a trigger decision. To realize a quick examination(in 20 bunch crossing intervals) on various trigger logics, the Memory Look-up Table(MLT) technique is implemented in the GFLT. It can be regarded as a projection(or mapping) of 700 input bits to 64 output bits, which are called as subtriggers or slots. GFLT makes a decision as logical OR of all these slots.

During this time($\simeq 5\mu s$), the raw data of each component are stored in analog or digital pipelines. This allows the low dead time, typically 1-2%.

3.3.2 Second level trigger and Event Builder

Once the GFLT issues an accept signal, then the raw data in the pipeline start to be read out. The digitalized readout data are stored in the buffer, which serves as same as the pipeline at the FLT. The task of the SLT is to reduce the rate from 1 KHz to 100 Hz.

As same as the FLT, the SLT is devided into the component SLT and the Global Second Level Trigger(GSLT). Each component SLT makes use of the readout data to send trigger signals to the GSLT. Information available at SLT are for example CAL energies and timings and CTD tracks and vertex. GSLT consists of a network of CPUs called transputers. The trigger logics are provided as codes written in a high-level computer language.

If a positive decision is made by the GSLT, all detector components send full data stored in the buffer to the Event Builder(EVB). The EVB collects them and constructs an structured [5] event.

3.3.3 Third level trigger

The TLT is designed to reduce the rate from 100 Hz to 5 Hz. This requires a large computing power since evaluation of complicated trigger logics are needed in the reduction.

The TLT is a workstation farm whose total computing power reaches to 1000 MIPS. The advantage of the use of workstations is that the filtering codes can be

[3] The missing transverse momentum and transverse energy calculated at the FLT, respectively.(cf. section 5.2)

[4] The good CTD track at the FLT.(cf. section 5.2)

[5] ADAMO format.

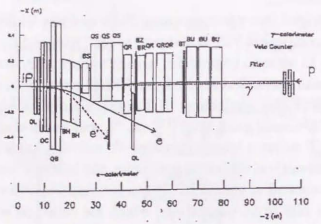

Figure 3.10: Layout of the LUMI detectors, the γ calorimeter and the electron calorimeter.

provided from offline analysis codes.

3.4 Luminosity measurement

The bremsstrahlung process $ep \to e'p\gamma$ is used to measure the luminosity [37]. This process is chosen since the cross section is well known in QED and is sufficiently large. The layout of the luminosity monitor system(LUMI) is shown in Figure 3.10. It consists of two detectors which tag electrons and photons, respectively.

The emitted photons travel in the proton beam pipe from the interaction point by 87 m. Then, they leave it through a copper window and go into the γ calorimeter which is placed at distances of Z from 104 to 107 m. The γ calorimeter is a lead-scintilator sampling type calorimeter. The size of the front surface is 18cm $\times$ 18 cm. The depth is 22 radiation length(X_0). A position detector, which consists of two crossed scintillator layers, is installed at the depth of 7 X_0.

The outgoing electrons are deflected from the beam orbit by the bending magnet due to the small loss of the energy. The electron calorimeter positioned inside the electron ring detects such electrons at 35 m downstream from the interaction point. The size of the front surface is 25 $\times$ 20 cm. The depth is 24 X_0.

In the luminosity measurement, only the event rates counted by the γ calorimeter is used. This is due to that the acceptance of the electron detector is not well understood. The geometrical acceptance of the γ calorimeter was studied by using events taken in the test runs dedicated to the study. In such runs, HERA provided only electrons which are tilted at the interaction point. The acceptance was also checked by using events tagged by the electron calorimeter. It is estimated to be

Year	$\mathcal{L}(\mathrm{pb}^{-1})$	$\delta\mathcal{L}/\mathcal{L}(\%)$
1994	3.0	1.5
1995	6.3	1.1
1996	10.7	1.3
1997	26.6	1.5
total	46.6	1.4

Table 3.2: Measured luminosities year-by-year for 1994 to 1997 positron runs.

99% with a Monte Calro simulation.

The backgrounds are from the bremsstrahlung of beam electrons on the gas molecules. The contamination is estimated using the event rate for the electron pilot bunches and is subtracted statistically as:

$$R_{ep} = R_{tot} - kR_{pilot}. \tag{3.2}$$

R_{tot} is the total count rate and R_{pilot} is the count rate for the electron pilot bunches. k is the ratio of the total electron current to that in the electron pilot bunches.

The overall systematic uncertainty in the luminosity measurement is typically 1-2%. The main contributions with typical errors in the brackets are: the background subtraction(0.3%), the geometrical acceptance(0.4%), the theoretical uncertainty in cross section(0.5%), and the energy scale uncertainty(0.65%).

The measured luminosities are summarized year-by-year in Table 3.4 for 1994 to 1997 positron runs. The error on the total luminosity was estimated as 1.4% according to

$$\frac{\delta\mathcal{L}}{\mathcal{L}} = \frac{\sum_{i=1994}^{1997} \left(\frac{\delta\mathcal{L}}{\mathcal{L}}\right)_i \times \mathcal{L}_i}{\sum_{i=1994}^{1997} \mathcal{L}_i}. \tag{3.3}$$

3.5 Monte Carlo simulation

Precise measurement requires precise understanding of the detector response, the selection efficiency, and the background contribution. In this analysis, we estimate these with the Monte Carlo simulation.

3.5.1 Simulation of DIS

The DJANGO [38] is a Monte Carlo program to simulate the deep inelastic lepton-nucleon scattering. It interfaces between the LEPTO [39] program which describes lepton-nucleon scattering with QCD correction and the HERACLES [40] program which includes the first order electroweak radiative correction. The parton

density function(PDF) used in the simulation can be selected among many parameterizations [41]. The simulation of DIS processes can be in general divided into three steps; the parton level interaction, the QCD cascade, and the hadronization.

The incoming parton is generated at first to collide on the beam electron according to the SM electroweak cross section formula and the parton density. This is the leading order parton level process $V^*q \to q'$. Here V^* denotes generally a vertual vector boson.

The first order QCD effects can be simulated using the exact matrix element(ME). These are the QCD Compton process(QCDC) $V^*q \to qg$ and the boson-gluon fusion process(BGF) process $V^*g \to q\bar{q}$. The MEPS(Matrix Element plus Parton Shower) model as implemented in the LEPTO [39] Monte Carlo program incorporates the higher order effects as Parton Shower(PS) with these first order matrix elements. The Parton Shower(PS) is a model based on the Altarelli-Parisi type splitting functions to generate partons from the hard process. This corresponds to the leading logarithm approximation of the emission.

On the other hand, the Color Dipole Model(CDM) as implemented in the ARIADNE [42] Monte Carlo program is based on the idea to treat a gluon emission from $q\bar{q}$ pair as a radiation from the color dipole between the q and $\bar{q}$. This model incorporates the BGF as an extra process. QCDC is included in the color dipole radiations.

The DJANGO implements both CDM and MEPS models for the simulation of the QCD effects. The iteration of radiation is repeated until the virtuality of the parton reaches to the cut off parameter of $\Lambda_{QCD} \simeq 1\,\mathrm{GeV}$.

Then, the partons are in stage to be simulated to fragment to hadrons. The LUND string model as implemented in the JETSET [43] Monte Carlo program simulates the fragmentation.

3.5.2 Detector Simulation

Generated Monte Carlo events are fed into the detector simulation. The ZEUS detector simulation(named "MOZART") is based on GEANT [44] in the CERN library which is commonly used in high energy experiments.

3.5.3 Monte Carlo Samples

Charged current samples were generated by using DJANGO(version 6.24) Monte Calro program. The CTEQ4D [45] parton density was used. The longitudinal structure function F_L was neglected.

The events with emitted photon show different behavior in the reconstruction of kinematic variables [46]. It is the reason why we used the DJANGO generator which includes the effect. In a presence of photon radiation, the four momentum transfer

q can be defined in two ways, i.e. the q seen from the hadron side($q_{had} \equiv p_h - p$) and the q seen from the lepton side($q_{lep} \equiv k - k'$). The two values(called "hadronic" and "leptonic" four momentum trasfers, respectively) are no longer equal to each other in contrast to the Born scattering case. The hadronic and leptonic scaling variables of x, y, and Q^2 are defined using each corresponding four momentum transfer. In this paper, "true" values to which measured variables are corrected are defined as the "hadronic" quantities.

Two kinds of samples were prepared each with the CDM and MEPS QCD cascade models. The CDM sample was used in the primary analysis and the MEPS sample was used for a systematic check.

Kinematic cuts were applied at the generator level to improve statistics at high Q^2 and high x phase space. It is summarized in the Table 3.3 for the CDM sample. The amount of the MEPS sample is as same as that of the CDM sample. Each sample was divided into four according to the data luminosity of the four years. The detector response was simulated by MOZART describing respective year's detector configuration. The vertex distribution used in the simulation was measured from un-biased low Q^2 NC events [55, 47].

An event, which was generated at (x_{gen}, Q^2_{gen}) and was fed into the MOZART for $year$, has a following weight to be combined:

$$w = \frac{\mathcal{L}^{data}(year)}{\sum_{Q^2_{cut}=10,5000,10000,20000}^{Q^2_{cut}<Q^2_{gen}} \frac{N_{gen}(Q^2_{cut},year)}{\sigma(Q^2_{cut})} + \sum_{x_{cut}=0.1,0.3,0.5}^{x_{cut}<x_{gen}} \frac{N_{gen}(x_{cut},year)}{\sigma(x_{cut})}}, \qquad (3.4)$$

where $\mathcal{L}^{data}(year)$ is the data luminosity of $year$. The sum $\sum_{Q^2_{cut}=10,5000,10000,20000}^{Q^2_{cut}<Q^2_{gen}}$ runs over all the Q^2 enrich samples if Q^2_{cut} is less than the event's Q^2_{gen}. $\sigma(Q^2_{cut})$ is the cross section for the Q^2 enrich sample generated with Q^2_{cut} threshold. $N_{gen}(Q^2_{cut}, year)$ is the number of events which were generated with Q^2_{cut} threshold and were fed into MOZART for $year$. The sum on x_{cut} is done similarly for the x enrich samples.

As possible sources of the background to the charged currents, we consider the photoproductions, the neutral currents, the single W-production, and the di-lepton productions via the Bethe-Heilter processes. Monte Carlo samples were generated in order to evaluate the contribution. Photoproductions(PHPs) denote γp interactions; i.e. emitted quasi-real photons from the electron interacts with the proton. Two types of interactions exist. The direct and the resolved processes are distinguished in the photoproductions at the leading order of the QCD. The photoproduction MC events were generated using the HERWIG [48] generator both for the direct and the resolved processes. In the generation, cuts were applied with the transverse energy of the generated final state hadrons; i.e. transverse energy at the hadron level, as $E_T(had) \geq 20\,\mathrm{GeV}$.

The neutral current MC events were generated using the DJANGO generator with a cut of $E_T > 35\,\mathrm{GeV}$ at the hadron level.

Table 3.3: Cross sections and number of generated events of the CDM charged current MC sample for each generator level cut. Events were generated using the DJANGO 6.24 with CTEQ 4D structure function.

	Q^2_{gen} cut (GeV^2)	x_{gen} cut	σ (pb)	N_{gen} (Kevts)
Q^2 enrich sample	> 10	–	40.5	115
	> 5000	–	25.1	75
	> 10000	–	4.77×10^{-1}	55
	> 20000	–	3.24×10^{-2}	40
x enrich sample	> 10	> 0.1	9.02	75
	> 10	> 0.3	1.10	50
	> 10	> 0.5	1.15×10^{-1}	20

Table 3.4: Cross sections and number of generated events of background MCs.

Process	Generator cut	σ (pb)	N_{gen} (Kevts)
PhP Direct	$E_T > 28\,GeV$	19.9×10^3	2057
PhP Resolved	$E_T > 28\,GeV$	74.0×10^3	2600
NC	$E_T > 35\,GeV$	22.6×10^2	229
$\mu\mu$ elastic	at least one μ: $5° < \theta < 170°$, $P_T > 3\,GeV$	36.8	20
$\mu\mu$ inelastic	at least one μ: $5° < \theta < 170°$, $P_T > 3\,GeV$	70.8	40
$\tau\tau$ elastic		105.8	60
$\tau\tau$ inelastic		71.4	60
W^+		50.3	74

The MC samples for the di-lepton productions were generated using the LPAIR [49] generator both for elastic and in-elastic processes. Di-muon productions and di-tau productions were also generated.
Single W productions were simulated using the EPVEC [50] generator. Table 3.4 shows luminosities of these background MC samples.

Chapter 4

RECONSTRUCTION OF KINEMATICS

4.1 Interaction vertex measurement

The vertex measurement is important for the kinematic reconstruction. The ep interaction vertex at HERA is spread in z direction with a standard deviation of about 15-20 cm. It is due to the proton bunch length. The collision between an electron and a proton which sits in front(back) in the bunch happens at a positive(negative) z position.

In this paper, we use two methods for the vertex measurement. One is to use the CTD tracks and the other is to use the FCAL timing [51, 52]. [1] We can measure x, y, and z positions of the vertex with the CTD tracks and z position of the vertex with the FCAL timing.

Typical resolution of the vertex position measured by the CTD is 0.4 cm in z direction. In transverse plane, the resolution is typically 0.1 cm which is larger than the typical size of both beams. Hence, we don't use the measured vertex positions in x and y directions in this analysis. We set them as the nominal vertex point, i.e. (0,0).

The FCAL timing vertex was calibrated by using NC data events [53]. The resolution improves as the deposited energy increases. It is 9 cm for events with FCAL energy greater than 10 GeV and is 7 cm with FCAL energy greater than 100 GeV.

For the z position of the vertex, either the CTD vertex or the FCAL timing vertex is used in this analysis. Details on this separation will be discussed in the section 5.1.2.

[1] The correlation between the FCAL timing and the vertex position in z direction is given as: produced hadrons arrive earlier(later) to FCAL when the proton is in front(back) in the bunch, i.e. the z vertex position is positive(negative).

4.2 The Jacquet-Blondel method

Kinematics of the charged current event is determined from the hadrons since the neutrino information is not accessible. F. Jacquet and A. Blondel proposed a reconstruction method [54]

$$y_{JB} = \frac{\mathrm{E}-\mathrm{P}_Z}{2\,\mathrm{E}_e}, \tag{4.1}$$

$$Q^2_{JB} = \frac{\not{P}_T{}^2}{1-y_{JB}}, \tag{4.2}$$

$$x_{JB} = \frac{\not{P}_T{}^2}{s y_{JB}(1-y_{JB})}, \tag{4.3}$$

where the four momentum of the event is given as $P=(E,P_X,P_Y,P_Z)$ and the E_e refers the electron beam energy.
$\not{P}_T$ is the absolute value of the missing transverse momentum, $\vec{\not{P}}_T$,

$$\vec{\not{P}}_T = (-P_X,-P_Y), \tag{4.4}$$

$$\not{P}_T = |\vec{\not{P}}_T| = \sqrt{P_X{}^2+P_Y{}^2}, \tag{4.5}$$

whereas the transverse energy of the event, E_T, is defined as:

$$\mathrm{E}_T = \sum_i \sqrt{(P_x{}^i)^2+(P_y{}^i)^2}. \tag{4.6}$$

The advantage of this method is that the particles, which escapes detection through the forward beam pipe, contribute little to $\mathrm{E}-\mathrm{P}_Z$ and $\not{P}_T$, hence the reconstructed kinematic variables.

The angle(γ) and energy(E_q) of the hadronic system are defined as:

$$\cos\gamma = \frac{\not{P}_T{}^2-(\mathrm{E}-\mathrm{P}_Z)^2}{\not{P}_T{}^2+(\mathrm{E}-\mathrm{P}_Z)^2}, \tag{4.7}$$

$$\mathrm{E}_q = \frac{\not{P}_T}{\sin\gamma}. \tag{4.8}$$

In the naive QPM, γ and E_q are equivalent to the scattering angle and energy of the struck quark.

4.3 The double angle hadronic energies

Hadronic energy measurement is the key issue for the CC kinematic reconstruction. Its quality can be checked by using NC events as follows.

The scattered electron angle(θ_e) and energy(E_e) can be measured in NC events as well as the hadronic angle(γ_h) and energy(E_q). [2] Since there are only two independent kinematic variables(e.g. x and Q^2), the kinematics of the neutral current event can be determined in several ways.

In the double angle(DA) method, θ_e and γ_h are used for the kinematic reconstruction as:

$$Q^2_{DA} = 4\mathrm{E}_e^2\frac{\sin\gamma_h(1+\cos\theta_e)}{\sin\gamma_h+\sin\theta_e-\sin(\theta_e+\gamma_h)}, \tag{4.9}$$

$$x_{DA} = \frac{\mathrm{E}_e}{\mathrm{E}_p}\frac{\sin\gamma_h+\sin\theta_e+\sin(\theta_e+\gamma_h)}{\sin\gamma_h+\sin\theta_e-\sin(\theta_e+\gamma_h)}, \tag{4.10}$$

$$y_{DA} = \frac{Q^2_{DA}}{s\,x_{DA}}, \tag{4.11}$$

where E_p is the proton beam energy. This method has an advantage to be less sensitive to the energy measurement. For $Q^2 > 400\,\mathrm{GeV}^2$, both the resolutions of Q^2_{DA} and y_{DA} are approximately constant 5% [55].

The transverse energy($p_T{}^h$) and total energy minus longitudinal momentum (($\mathrm{E}-\mathrm{P}_Z$)^h) of hadrons are then estimated by using the DA variables as:

$$p_T{}^{h,DA} = \sqrt{Q^2_{DA}(1-y_{DA})}, \tag{4.12}$$

$$(\mathrm{E}-\mathrm{P}_Z)^{h,DA} = 2y_{DA}\mathrm{E}_e, \tag{4.13}$$

according to the Jacquet-Blondel formula(equations 4.1, 4.2 and 4.3). These variables provide a good test of the hadronic energy measurement.

4.4 Reconstruction of hadronic energy

4.4.1 Uranium-noise and spark suppression

The ZEUS calorimeter uses uranium as absorber. The radioactivity of the uranium causes background noise. The energy cut of 60(110) MeV for all EMC(HAC) cells was applied to suppress this noise. The threshold is raised to 100(150) MeV for isolated EMC(HAC) cells. These thresholds were determined based on a study using randomly triggered events [56].

Photomultipliers sometimes undergo a discharge. This spark of a PMT results in a large energy imbalance between the two PMTs of the cell. We avoid these effect by removing isolated cells that have an imbalance of

$$\frac{|E_L-E_R|}{E_L+E_R} > 0.8, \tag{4.14}$$

where $\mathrm{E}_L(\mathrm{E}_R)$ is the energy of the left(right) side PMT. This threshold was also determined from the study using randomly triggered events.

[2] The subscript h denotes that the quantity is measured only with hadrons in NC events.

4.4.2 Clustering of energy deposits

The unit of the energy measurement is a calorimeter cell. To obtain global energies like $\not{P}_T$ and $E-P_Z$, it may be the simplest way to sum up these cell energies. Each cell is regarded as an zero-mass energy deposit at its center of gravity position. The energy correction is performed on these global energies.

However, the energy resolution would improve if the energy correction is done for each particle. For this purpose, we perform a clustering of energy deposits to obtain objects which are closer to the real particles as possible. It consists of two stages, the clustering with the cell-island algorithm and that with the cone-island algorithm [57].

The cell-island algorithm connects calorimeter cells. The merging works separately in each calorimeter sections of EMC, HAC1, and HAC2 also separately for the FCAL, BCAL and RCAL. A cell is merged to the cell which has the maximum energy among the nearest adjacent cells, i.e. surrounding cells except for those which locate diagonally. The objects as a consequence of the algorithm are called cell-islands.

Then, the cell-islands are merged under the cone-island algorithm. Two cell-islands are examined whether to be connected or not with a measurement of these opening angle. The objects as a consequence of the algorithm are called cone-islands.

4.4.3 Energy correction

The cone-island is the unit for the energy correction. Three effects are corrected [55, 58].

The first is a correction for the albedo-effect. It arises from the backward scattering particles by hitting materials in front of the calorimeter and the calorimeter itself. Though the amount is small, typically a few percent of incident energy, it induces non negligible effect especially for the $E-P_Z$ measurement. The cone-islands with energy less than 3 GeV were removed if $\theta_{\text{cone-island}} > \gamma_{max}$. Here $\theta_{\text{cone-island}}$ is the polar angle of the cone-island. The γ_{max} was determined by using NC MC events so as not to exclude more than 1% of islands identified as free of the effect. The amount of the removed energy showed a good agreement between NC data and MC, indicating that the MC describes the effect well.

Next, the energy loss in inactive material before reaching to the calorimeter is corrected. The correction factor was parameterized as a function of the radiation length from the interaction point. This factor was determined differently for the "electromagnetic" and "hadronic" cone-islands taking into account for the different behavior in materials. Here the electromagnetic cone-island is defined to consist purely of EMC cells. If not, it is defined as hadronic-islands.

The ratio of the measured and double angle quark energy, E_q/E_q^{DA}, was examined for the last step of the correction for both neutral current data and MC events. It

was found that an additional correction was needed in the FCAL-BCAL and BCAL-RCAL boundaries. The correction factors were determined by fitting E_q/E_q^{DA} as a function of γ_h separately for data and MC. A few percent difference was found between them. Cone-islands in the boundaries are corrected separately for data and MC with the respective correction factors.

The global quantities(e.g. $\not{P}_T$ and $E-P_Z$) are obtained by summing these cone-islands' energies.

4.5 Checks on the hadronic energy measurement and simulation

To check the hadronic energy correction, ${p_T}^h$, $(E-P_Z)^h$ and E_q^h in NC events were compared with the respective double angle values [58, 59]. The NC data were selected with $Q^2_{DA} > 400\,\text{GeV}^2$ from the same e^+p data used in this analysis.

Figure 4.1 shows the ${p_T}^h/{p_T}^{h,DA}$ in bins of γ_h both for NC data and MC. The distributions show a peak around unity, indicating that the ${p_T}^h$ is well corrected. In addition, the agreement between data and MC is good. This indicates that the detection response on ${p_T}^h$ is well reproduced by MC simulation for the relevant γ_h range. Figure 4.2 shows the $E_q^h/E_q^{h,DA}$ in bins of $E_q^{h,DA}$. The data distributions peak around unity and agree with MC in all $E_q^{h,DA}$ bins.

Figure 4.3 shows the gaussian fitted resolution of ${p_T}^h/{p_T}^{h,DA}$ as functions of E_q and γ_h. The agreement between data and MC is good in both plots. The resolution varies only slightly as functions of E_q and γ_h. The behavior is well reproduced with the MC simulation.

The $(E-P_Z)^h$, which is another important quantity in the CC kinematic reconstruction, is also compared with the double angle value. Figure 4.2 shows $(E-P_Z)^h/(E-P_Z)^{h,DA}$ in bins of y_{DA}, which equals to $(E-P_Z)^{h,DA}/2E_e$. It indicates that the $(E-P_Z)^h$ is also well corrected and is well reproduced by Monte Carlo simulation.

Figure 4.5 shows the γ_h, ${p_T}^h$, and $(E-P_Z)^h$ distributions of NC events compared with the Monte Carlo simulation. Good agreement is observed in all distributions.

4.6 Resolutions of charged current kinematics

The quality of the charged current kinematic reconstruction was evaluated using MC events with $Q^2_{true} \geq 200\,\text{GeV}^2$. A cut of $\not{P}_T \geq 7\,\text{GeV}$ was also applied.

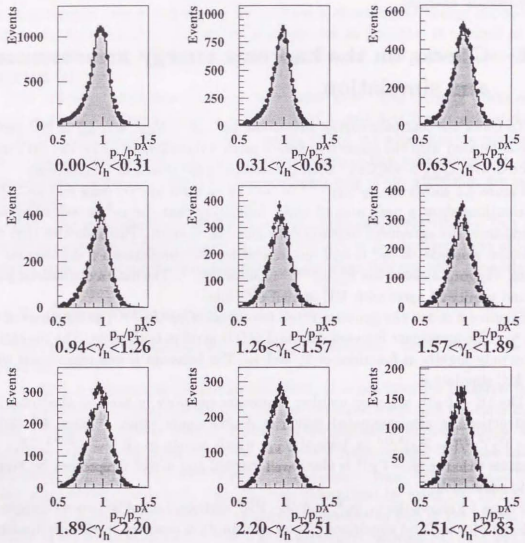

Figure 4.1: Comparison of $p_T{}^h/p_T{}^{h,DA}$ in bins of γ_h [59].

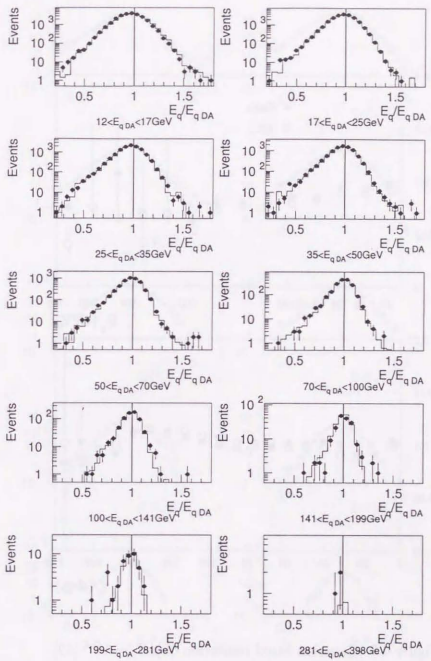

Figure 4.2: Comparison of $E_q^h/E_q^{h,DA}$ in bins of E_q^h [58].

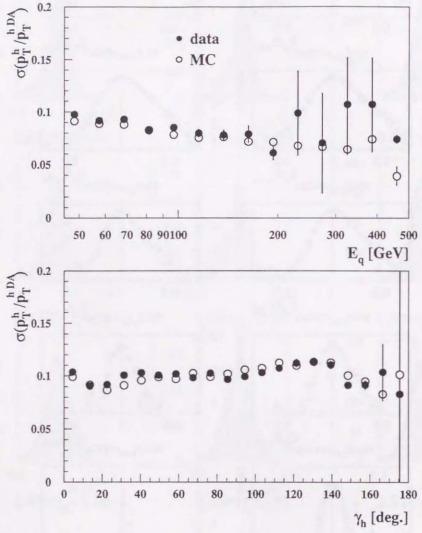

Figure 4.3: Gaussian fitted resolution of $p_T{}^h/p_T{}^{h,DA}$ [59].

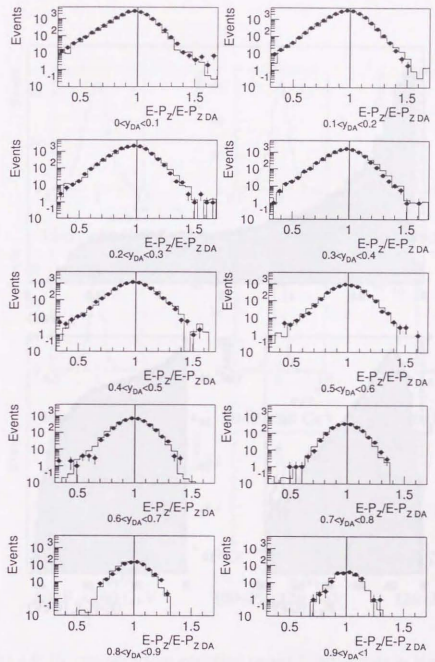

Figure 4.4: Comparison of $(\mathrm{E}-\mathrm{P_Z})^h/(\mathrm{E}-\mathrm{P_Z})^{h,DA}$ in bins of y_{DA} [58].

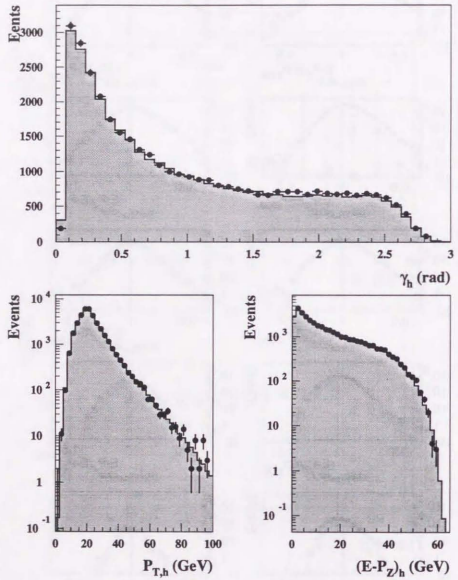

Figure 4.5: Hadron measurement for the NC events [59].

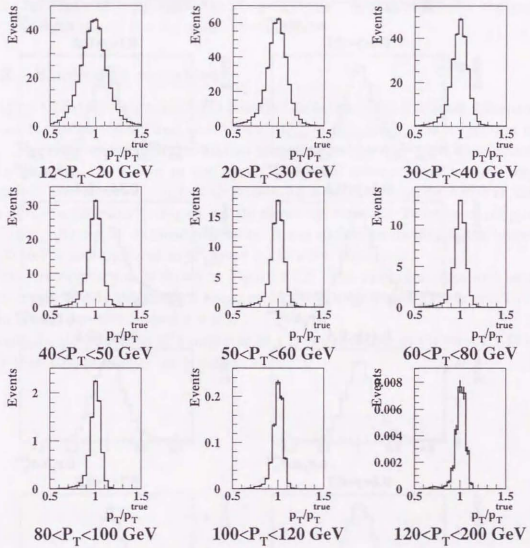

Figure 4.6: $\not{P}_T$ reconstruction evaluated using CC MC events in bins of $\not{P}_T{}^{true}$.

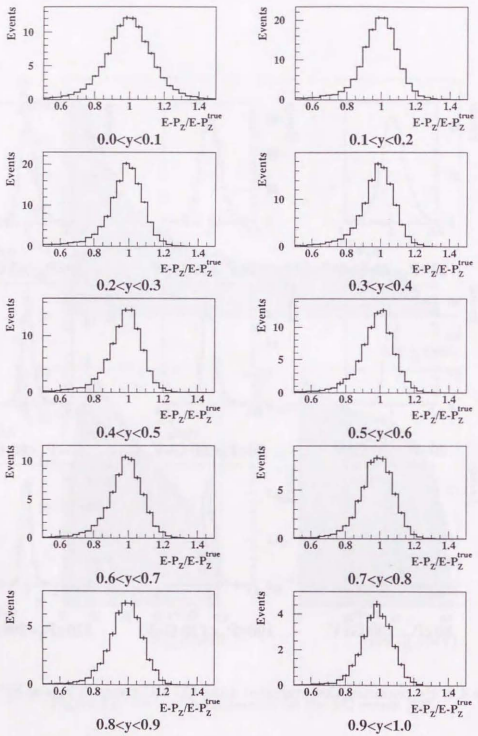

Figure 4.7: $E - P_Z$ reconstruction evaluated using CC MC events in bins of y_{true}.

4.6.1 $\not{P}_T$ and $E - P_Z$ reconstruction

Figures 4.6 and 4.7 show the $\not{P}_T/\not{P}_T{}^{true}$ and $(E - P_Z)/(E - P_Z)^{true}$, respectively. These true values were defined as:

$$\not{P}_T{}^{true} = \sqrt{Q^2_{true}(1 - y_{true})}, \quad (4.15)$$

$$(E - P_Z)^{true} = 2E_e\, y_{true}. \quad (4.16)$$

The resolution of $\not{P}_T$ improves as $\not{P}_T$ goes higher. Typical resolution is about 10%. The resolution of $E - P_Z$ is also about 10%.

4.6.2 Kinematic variables

Figure 4.8 (a) shows the mean and standard deviation of the fractional difference between the reconstructed and true values, $(Q^2_{rec} - Q^2_{true})/Q^2_{true}$, as a function of Q^2_{true}. The mean and standard deviation were obtained by fitting the distribution with a gaussian. As shown in the figure, Q^2 is well reconstructed without any strong bias over the wide range of Q^2 except for a small shift(up to 7-8%) at the lower $Q^2(Q^2 < 1000\,\mathrm{GeV}^2)$. Figure 4.8 (b) shows the standard deviation of $(Q^2_{rec} - Q^2_{true})/Q^2_{true}$ divided by its mean plus unity. It was slightly below 30% at the lowest $Q^2(200\ \mathrm{GeV}^2)$ and improved as Q^2 grows up to a few thousands.

The x reconstruction is shown in Figure 4.6.2. The resolution improved as x grows. It was 30% in the lowest x range($x \simeq 10^{-2}$). It improved to 12% at $x \simeq 10^{-1}$ and to several percents beyond $x > 0.2$.

Similarly, the resolution of y improves as y grows as shown in Figure 4.10. It is better than 10% in most of the y range.

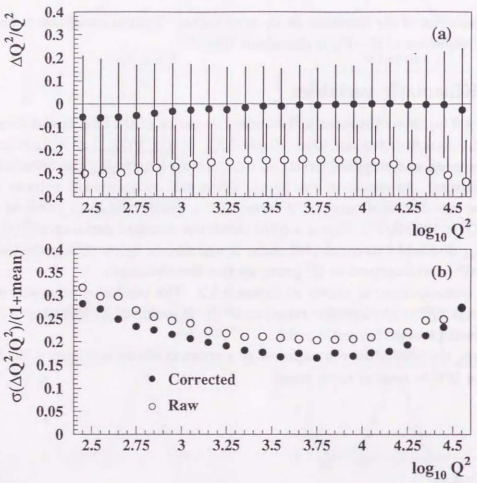

Figure 4.8: Q^2 reconstruction evaluated using CC MC events: (a) mean and standard deviation of $(Q^2_{rec} - Q^2_{true})/Q^2_{true}$, (b) standard deviation divided by (1+mean) for $(Q^2_{rec} - Q^2_{true})/Q^2_{true}$. The closed circles represent the reconstruction from corrected cone-islands and the open circles represent the reconstruction from cells without any energy correction.

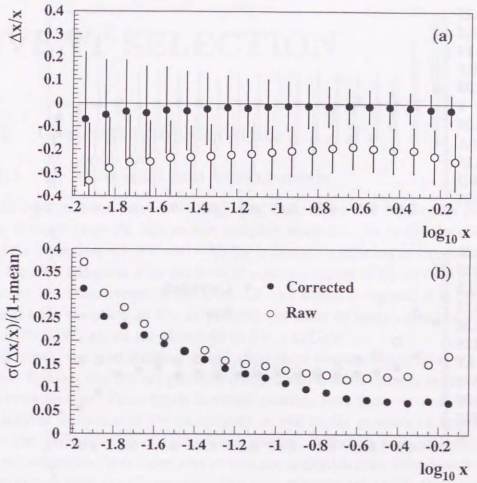

Figure 4.9: x reconstruction evaluated using CC MC events: (a) mean and standard deviation of $(x_{rec} - x_{true})/x_{true}$, (b) standard deviation divided by (1+mean) for $(x_{rec} - x_{true})/x_{true}$. The closed circles represent the reconstruction from corrected cone-islands and the open circles represent the reconstruction from cells without any energy correction.

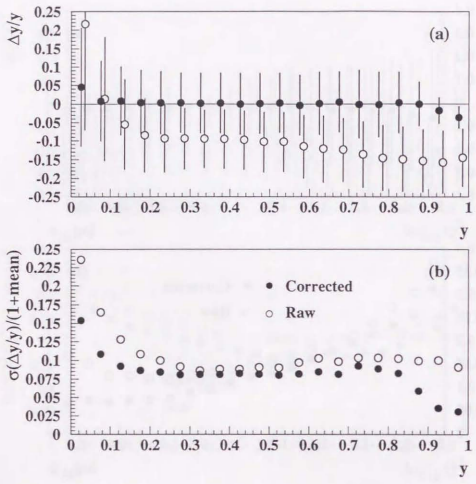

Figure 4.10: y reconstruction evaluated using CC MC events: (a) mean and standard deviation of $(y_{rec} - y_{true})/y_{true}$, (b) standard deviation divided by (1+mean) for $(y_{rec} - y_{true})/y_{true}$. The closed circles represent the reconstruction from corrected cone-islands and the open circles represent the reconstruction from cells without any energy correction.

Chapter 5

EVENT SELECTION

5.1 General consideration

5.1.1 $\not\!\!E_T$ threshold and backgrounds

Charged current event is distinguished from the events from other processes in that it has a large $\not\!\!E_T$ due to the escaping neutrino. As in the Jacquet-Blondel formula (equations 4.1, 4.2, and 4.3), $\not\!\!E_T$ is directly connected to the event kinematics. Figure 5.1 depicts it as the lines of constant values of $\not\!\!E_T$ in the (x, Q^2) plane. In order to obtain events in the lower Q^2 and higher y regions, it is preferable to keep the $\not\!\!E_T$ threshold as low as possible. In order to keep a good acceptance for $Q^2 > 200\,\mathrm{GeV}^2$, we set the threshold as $\not\!\!E_T > 12\,\mathrm{GeV}$.

However, the low threshold would allow more contamination from other ep processes. Possible sources are photoproduction and neutral current events with large transverse energy. These types of events possibly have some amount of $\not\!\!E_T$ due to the limited resolution of the calorimeter or due to the presence of muons resulted from the fragmentation of heavy flavor quarks. Although such probability is low, the contamination from these processes is not negligible since they have much larger cross section than the CC process. The most effective cut to kill them is to require a large $\not\!\!E_T/E_T$ since $\not\!\!E_T$ of such events is likely to be caused by fluctuation in case of a large transverse energy. We set a tighter threshold on $\not\!\!E_T/E_T$ in low $\not\!\!E_T$ region.

Other potential background sources are di-lepton productions via Bethe-Heitler process and single productions of $W^{\pm}$. The momentum of the μ and τ leptons is not correctly measured in the CAL. Once real $W^{\pm}$ boson is produced and decays into leptons, a large $\not\!\!E_T$ may be detected.

Furthermore, there are considerable amount of events with large $\not\!\!E_T$ originated from non-ep collisions. Cosmic ray muons falling on the detector (called "cosmic ray" events) and beam-halo-muons passing through the detector along the z-direction (called "halo-muon" events) can give a large and localized energy deposit by interacting inside the CAL, which results in $\not\!\!E_T$. A fraction of events where the beam

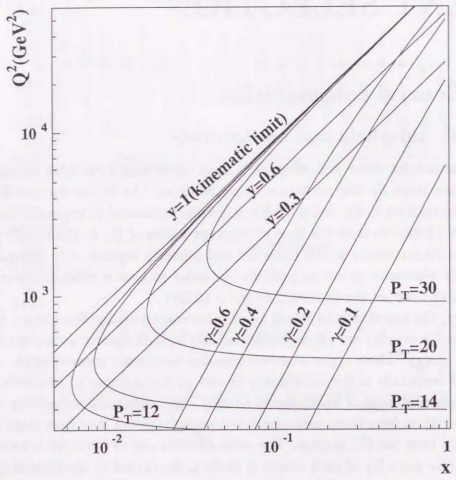

Figure 5.1: $\not\!\!E_T$, γ, and y in the (x, Q^2) kinematic plane. $\not\!\!E_T$ in GeV and γ is in radian.

proton interact with the residual gas inside the beam pipe(called "beam-gas" events) can have large $\not\!\!E_T$. Beam-gas events deposit large energies close to the forward beam pipe, mostly in the inner most ring of the FCAL. We calculated a $\not\!\!E_T$ from cells excluding the FCAL inner most ring($\not\!\!E_T(-1ir)$). It is effective to set a threshold on $\not\!\!E_T(-1ir)$ to kill the beam gas events.

5.1.2 Low γ_0 and high γ_0 events

Charged current events with small hadronic angle γ are experimentally challenging since the hadrons lie close to the forward beam pipe and the track measurement by the CTD becomes difficult. At the same time, such events are interesting since they populate in a specific phase space, high x. Figure 5.1 depicts it as the lines of constant values of γ in the (x, Q^2) plane.

Let us start with qualifying the two vertex finding algorithms, the CTD and FCAL timing vertex reconstructions. Figure 5.2 shows the vertex finding efficiency by the CTD as a function of γ_0 evaluated by using charged current MC events with $Q^2_{true} > 200\,\mathrm{GeV}^2$. γ_0 is the hadronic angle measured from the nominal interaction point

$$\cos\gamma_0 \equiv \frac{(\not\!\!E_T)_0^2 - (\mathrm{E}-\mathrm{P}_Z)_0^2}{(\not\!\!E_T)_0^2 + (\mathrm{E}-\mathrm{P}_Z)_0^2}. \tag{5.1}$$

The suffix 0 for $(\not\!\!E_T)$ and $(\mathrm{E}-\mathrm{P}_Z)$ indicates to be measured from the nominal interaction vertex, i.e. (0,0,0). The efficiency drops at $\gamma_0 < 0.4$. The figure also presents efficiencies of the cuts using or qualifying the CTD tracks(more explanations will come later in the section 5.6.2) which show the same fall off at $\gamma_0 < 0.4$. The quality of the CTD and FCAL timing vertexes are presented in Figure 5.3 as a function of γ_0. As shown in plot (a), the z component of the CTD vertex position tends to be pulled to forward direction in the low γ_0 region. At the same time, the resolution becomes worse as shown in plot (c). On the other hand, the vertex reconstruction from the FCAL timing is not biased even in such low γ region and has a better resolution than the CTD vertex. With these observations, we divide event sample into high γ and low γ events at $\gamma_0 = 0.4$ and impose different selection cuts and different kinematic reconstruction methods.

- For high γ events,
  the CTD vertex position was used for Z_{vtx}. A fiducial cut on this Z_{vtx} was applied. Some requirements based on the CTD tracks were also applied.

- For low γ events,
  the FCAL timing vertex position was used for Z_{vtx}. A fiducial cut on this Z_{vtx} was applied. Any cuts on CTD tracks are not imposed.

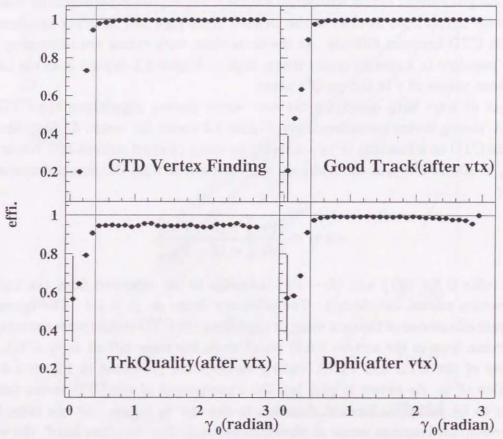

Figure 5.2: Efficiency of the vertex finding by the CTD as a function of γ_0 as well as of cuts related to CTD tracks used in the high γ selection. The switching point of $\gamma_0 = 0.4$ is also indicated. Clear drop of efficiency in the low γ region, $\gamma_0 < 0.4$, is seen in all figures.

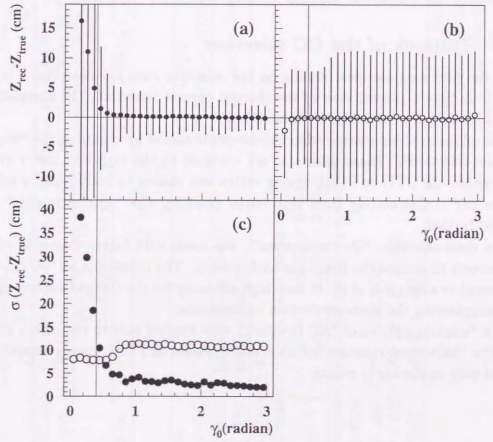

Figure 5.3: Quality of the CTD and FCAL timing vertex reconstructions as a function of γ_0. The means of $Z_{\rm rec} - Z_{\rm true}$ are shown in (a) for the CTD vertex and in (b) for the FCAL timing with the error bars indicating their RMS deviations. These RMS resolutions are also shown in (c) with closed circles for the CTD vertex and with open circles for the FCAL timing vertex.

Since we abandon the effective cuts with CTD tracking quantities, there would be a large amount of non-ep backgrounds in the low γ region. Typical events are the beam-gas and halo-muon events without CTD vertex or even without any CTD tracks. Tight threshold on $\not{P}_T(-1ir)$ was imposed to remove the beam-gas contamination for the low γ sample. Events caused by halo-muons passing through the FCAL along the z direction end up with a narrow shower width in transverse compared with those of charged current events. A few topological cuts on the shower shape inside the FCAL was imposed to eliminate the contribution.

5.1.3 Outlook of the CC selection

In the following sections, details on the selection cuts are described. In this section, we take a general view of the charged current selection. The complete list of the selection is summarized in Table 5.1.

The offline analysis started from the sample obtained by requiring the "trigger" and "pre-selection". These selections are common to the high and low γ events. Then, either the CTD or FCAL timing vertex was chosen to be imposed a fiducial "vertex cut". Calculating from this vertex position, the "kinematic cuts" were imposed further.

The main selection, "$\not{P}_T$ requirement", was made with higher threshold for the low γ events to remove the beam-gas backgrounds. The thresholds on "$\not{P}_T/E_T$ cut" were tuned as a function of $\not{P}_T$ to keep high efficiency for the charged current signals while suppressing the photoproduction backgrounds.

The "tracking cuts" and "NC rejection" were applied only to the high γ events, while the "halo-muon rejection" which is mainly based on FCAL energy deposits was applied only to the low γ events.

Table 5.1: Summary of the charged current selection.

	High γ Selection ($\gamma_0 > 0.4$)	Low γ Selection ($\gamma_0 < 0.4$)
Trigger	FLT(slot_41 .or. slot_42 .or. slot_43 .or. slot_44 .or. slot_60) .and. SLT(EXO_SLT_4) .and. TLT(EXO_TLT_02 .or. EXO_TLT_06)	
Pre-selection	$\not{P}_{T\,miss}^{maxbr} > 7$ GeV .and. $\not{P}_T^{maxbr}(-1ir) > 7$ GeV cleaning cuts for non-ep events	
Vertex cut	$\lvert Z_{CTD}\rvert < 50$ cm	$\lvert Z_{timel}\rvert < 50$ cm
Kinematic cuts	$Q^2 > 200\,\mathrm{GeV}^2$ $y < 0.9$	
$\not{P}_T$ requirement	$\not{P}_T > 12$ GeV $\not{P}_T(-1ir) > 10$ GeV	$\not{P}_T > 14$ GeV $\not{P}_T(-1ir) > 12$ GeV
$\not{P}_T/E_T$ cut	$\not{P}_T/E_T > \begin{cases} 0.40 & \text{for } 20 < \not{P}_T < 30\,\mathrm{GeV} \\ 0.55 & \text{for } \not{P}_T < 20\,\mathrm{GeV} \end{cases}$	$\not{P}_T/E_T > 0.6$ for $\not{P}_T < 30$ GeV
Tracking cuts	No. of good tracks ≥ 1 No. of good tracks $> \frac{1}{4} \times$(No. of all tracks $- 20$) $\lvert\Delta\phi_{CAL-CTD}\rvert < \begin{cases} 2.0\,\text{radian} & \text{for } \not{P}_T > 20\,\mathrm{GeV} \\ 1.0\,\text{radian} & \text{for } \not{P}_T < 20\,\mathrm{GeV} \end{cases}$	
NC rejection	Events are rejected if following conditions are satisfied $E - P_Z > 30$ GeV $E^e > 4$ GeV .and. $E^{come} - E^e < 5$ GeV $\begin{cases} P^e_{trk}/E^e > 0.25 & \text{for } 15° < \theta^e < 164° \\ E^e_T > 2\,\mathrm{GeV} & \text{for } \theta^e > 164° \end{cases}$	
Halo-muon rejection		$N^{Fk}_{HMU} = 0$ for $N^{Fk}_{CTD} = 0$ $E^{EMC}_{FCAL}/E_{FCAL} > 0.1$ $E^{HAC1}_{FCAL}/E_{FCAL} > 0.1$ $E^{HAC2}_{FCAL}/E_{FCAL} < 0.3$ $N^{t}_{wid} > 1$(2) for $N^{Fr}_{mtrk} \geq 1(=0)$ $N^{m}_{wid} > 1$(2) for $N^{Fr}_{mtrk} \geq 1(=0)$ $E_{T\,wid}{}^{t} > 6$(10) GeV for $N^{Fr}_{mtrk} \geq 1(=0)$ RasoE < 0.1 GeV for $N^{Fr}_{mtrk} = 0$

5.2 Trigger

With the same consideration for the low γ events as in the previous section, the basic concept for the charged current trigger is to prepare two logics aiming for the high and low γ events, respectively.

At the FLT, the slot_60 aims to trigger $\not{P}_T$ events. The logic implemented in the slot_60 is as follows:

$$(\not{P}_T{}^{FLT} > 5\,\mathrm{GeV} \ \text{.and.} \ E_T{}^{FLT} > 5\,\mathrm{GeV} \ \text{.and.} \ \text{good\_TRK}^{FLT}) \ \text{.or.} \quad (5.2)$$

$$(\not{P}_T{}^{FLT} > 8\,\mathrm{GeV} \ \text{.and.} \ (\text{any\_TRK}^{FLT} \ \text{.or.} \ E_{FCAL}{}^{FLT} > 10\ \mathrm{GeV})). \quad (5.3)$$

The subscript FLT indicates the value is calculated at the FLT. Note that the resolutions of the quantities at the FLT are worse since they are different from the read out data(see figure 3.9) and are coarsely digitized. $E_T{}^{FLT}$ is calculated excluding FCAL most and second most inner rings.

To keep the trigger rates to be acceptable, it becomes crucial to reject the beam-gas backgrounds. Then the first logic(equation 5.2) is to be read as: if there are some tracks that can be labeled as good, they can be triggered with low threshold of $\not{P}_T$ and E_T since contribution from the beam-gas events would be acceptable. The second logic(equation 5.3) is to be read as: if any tracks are found, or certain amounts of energies are deposited in the FCAL even if no track is found, events can be triggered however with higher $\not{P}_T$ to reduce the beam-gas contributions.

As well as the slot_60, we also let events that pass other slots based on calorimeter energies to be included in the analysis to supplement selection efficiency. The offline analysis requires events to have passed at least one of slots among slot_41, slot_42, slot_43, slot_44, and slot_60. [1] This also enables us to make a cross check on $\not{P}_T$ trigger efficiency as will be described later in the chapter 7. The logics of calorimeter based triggers are as follows:

$$E_T{}^{FLT} > 30\,\mathrm{GeV}\ [\text{slot\_41}] \quad (5.4)$$

$$(E^{FLT} > 15\,\mathrm{GeV}\ \text{.or.}\ E_{EMC}{}^{FLT} > 10\,\mathrm{GeV}\ \text{.or.}\ E_{BEMC}{}^{FLT} > 3.4\,\mathrm{GeV}$$
$$\text{.or.}\ E_{REMC}{}^{FLT} > 2\,\mathrm{GeV})\ \text{.and.}\ (\text{good\_TRK}^{FLT})\ [\text{slot\_42}] \quad (5.5)$$

$$E_T{}^{FLT} > 11.5\,\mathrm{GeV}\ \text{.and.}\ \text{good\_TRK}^{FLT}\ [\text{slot\_43}] \quad (5.6)$$

$$E_{BEMC}{}^{FLT} > 4.8\,\mathrm{GeV}\ \text{.and.}\ (\text{any\_TRK}^{FLT}\ \text{.or.}\ E_{REMC}{}^{FLT} > 3.4\,\mathrm{GeV})\ [\text{slot\_44}] \quad (5.7)$$

[1] Historically, before incorporated in one and was set to the slot_60, the two $\not{P}_T$ logics were implemented separately in the slot_60 and slot_61 in 1994 and in early of 1995 running period. The offline selection requires (slot_60 .or. slot_61) for events taken in such period.

E_{EMC}, E_{BEMC}, and E_{REMC} are EMC energies of whole calorimeter, BCAL, and RCAL, respectively.

At the SLT, a branch named "EXO_SLT_4" is dedicated to the $\not{P}_T$ trigger.

$$(|t_G| < 7\,\mathrm{ns})\ \text{.and.} \quad (5.8)$$

$$((\not{P}_T{}^{SLT} > 6\,\mathrm{GeV}\ \text{.and.}\ E_T{}^{SLT}(-2\mathrm{ir}) > 6\,\mathrm{GeV}\ \text{.and.}\ \text{good\_TRK}^{FLT})\ \text{.or.} \quad (5.9)$$

$$((\not{P}_T{}^{SLT} > 9\,\mathrm{GeV}\ \text{.and.}\ E_T{}^{SLT}(-1\mathrm{ir}) > 8\,\mathrm{GeV}\ \text{.and.}\ E_{FCAL}{}^{SLT} > 20\,\mathrm{GeV})(5.10)$$

$$((\not{P}_T{}^{SLT} > 9\,\mathrm{GeV}\ \text{.and.}\ \not{P}_T{}^{SLT}/\sqrt{E_T{}^{SLT}} > 2.1\ \text{.and.}\ E_{FCAL}{}^{SLT} > 80\,\mathrm{GeV}))(5.11)$$

$\not{P}_T{}^{SLT}$ is calculated from the nominal interaction position. Timing information is available after the SLT; t_G in the equation 5.8 is the timing measured by whole calorimeter cells, and is required to be consistent with ep collision. $E_T(-2\mathrm{ir})$ is a E_T calculated excluding the most and second most inner rings of the FCAL; the logic expressed in equation 5.9 is for the high γ events as similar as in the FLT equation 5.2. The logics in equations 5.10 and 5.11 are for the low γ events. The offline selection requires events to have passed the EXO_SLT_4 at the second level of triggers. [2]

At the TLT, two branches named "EXO_TLT_2" and "EXO_TLT_6" are assigned for $\not{P}_T$ trigger. The EXO_TLT_02 logic is,

$$(\not{P}_T > 6\,\mathrm{GeV})\ \text{.and.}\ (\text{GoodTrack} \geq 1)\ \text{.and.}\ (\text{GoodVertex})\ \text{.and.}$$
$$\text{UDTimeOK}. \quad (5.12)$$

Cosmic rays falling on the detector leave earlier timing in the upside half of the calorimeter than the one in the downside half. The logic "UDTimeOK" requires the time difference between measured in the upside and in the downside halves of the calorimeter is less than 8 ns. The logic of EXO_TLT_06 is as follows.

$$\text{EXO\_SLT\_4 .and.} \quad (5.13)$$

$$\not{P}_T > 8\,\mathrm{GeV}\ \text{.and.}\ (E_{FCAL} > 10\,\mathrm{GeV}\ \text{.or.}\ \text{FLT\_49})\ \text{.and.} \quad (5.14)$$

$$((\text{No.CTD\_Hits} < 2500)\ \text{.or.}\ (\not{P}_T(-1ir) > 10\,\mathrm{GeV}))\ \text{.and.} \quad (5.15)$$

$$(\text{.not. BeamGasVertex})\ \text{.and.} \quad (5.16)$$

$$((\text{.not. TooManyBeamGasTracks}).\text{or.}(\text{GoodVertex}))\ \text{.and.} \quad (5.17)$$

$$\text{UDTimeOK} \quad (5.18)$$

The offline requirement was made to pass either of EXO_TLT_02 or EXO_TLT_06 at the third level trigger stage. [3]

[2] For 1994 data, "DIS-2" is required, instead.

[3] For 1994 data, EXO-2 or DIS-3 is required, instead.

5.3 Pre-selection and cleaning cuts

At beginning $\not\!\!E_T$ and $\not\!\!E_T(-1ir)$ were calculated assuming three interaction points, nominal, CTD, and FCAL timing vertex positions. In this stage, $\not\!\!E_T$ is calculated from cells. Taking the maximum of the three, the following cut was applied.

$$\not\!\!E_T{}_{cell}^{max3v} > 7\,\mathrm{GeV}, \tag{5.19}$$
$$\not\!\!E_T{}^{max3v}(-1ir) > 7\,\mathrm{GeV}, \tag{5.20}$$

where $\not\!\!E_T{}_{cell}^{max3v}$ and $\not\!\!E_T{}^{max3v}(-1ir)$ are the maxima.

Furthermore, cleaning cuts to reject cosmic rays or halo-muon induced events were applied. Details on these algorithms are described in the appendix A.

5.4 Vertex cut

Z-component of the vertex position was taken from either the CTD or FCAL timing reconstructions according to γ_0 while both x and y components were set to zero.

$$\mathrm{Vtx} = (0, 0, Z_{\mathrm{vtx}}), \tag{5.21}$$
$$Z_{\mathrm{vtx}} = \begin{cases} Z_{\mathrm{CTD}} & \gamma_0 > 0.4, \\ Z_{\mathrm{time}} & \gamma_0 < 0.4. \end{cases} \tag{5.22}$$

The z-component of the vertex was required as:

$$|Z_{\mathrm{vtx}}| < 50\,\mathrm{cm}. \tag{5.23}$$

Figure 5.4 shows both the FCAL timing and CTD vertex positions both for the high and low γ events. The upper-right plot is the distribution of the CTD vertex position for the high γ events. It is well reproduced by MC simulations except for the outside of the fiducial region; some events are clustered above MC expectation around $Z_{\mathrm{vtx}} \simeq 100\,\mathrm{cm}$. It turned out that these are the beam-gas events whose $\not\!\!E_T$ was mistakenly reconstructed to be large.

5.5 Kinematic cuts

We restricted the kinematic region for the cross section measurement as:

$$Q^2 > 200\,\mathrm{GeV}^2, \tag{5.24}$$
$$y < 0.9. \tag{5.25}$$

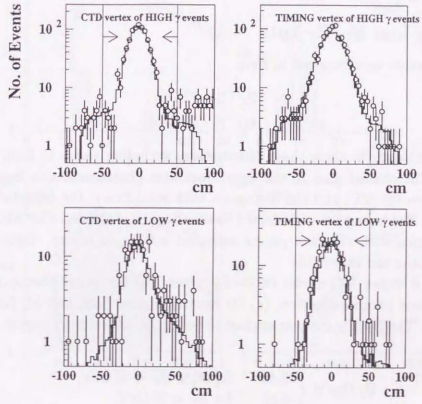

Figure 5.4: Distributions of Z_{vtx} in unit of cm. Upper plots are of the high γ events, and the lower plots are of the low γ events. Left plots show Z_{CTD} and right ones are for Z_{TIME}. The fiducial cut is made for the upper left plot and the lower right plot as indicated in the figure.

The y cut is needed since x and Q^2 resolutions degrade at high y. From the equation 4.2, Q^2 resolution is expressed as:

$$\frac{\Delta Q^2}{Q^2} = \sqrt{4(\frac{\Delta \not{P}_T}{\not{P}_T})^2 + (\frac{\Delta y}{1-y})^2}. \quad (5.26)$$

It is clear that it becomes large near $y \simeq 1$.

5.6 High γ selection

5.6.1 $\not{P}_T$ and $\not{P}_T/E_T$ cuts

High γ events were required to have

$$\not{P}_T > 12\,\text{GeV}, \quad (5.27)$$
$$\not{P}_T(-1ir) > 10\,\text{GeV}. \quad (5.28)$$

Figure 5.5 (a) and (b) show these distributions excluding each cut from the final selection. The shaded area in the figure indicates photoproduction contribution expected from the MC, and the histogram with solid line is the expectation from the CC MC. The histogram with dotted line is the sum of CC and PhP MC samples to be compared with the data points indicated with open circles. Data and MC agree well above the thresholds.

Figure 5.6 shows MC events in $\not{P}_T$-E_T plane; (a) for direct photoproduction, (b) for resolved photoproduction, (c) for neutral current DIS, and (d) for charged current DIS. The $\not{P}_T/E_T$ cut was applied to be tighter at lower $\not{P}_T$ region as shown in the figure,

$$\not{P}_T/E_T > \begin{cases} 0.40 & \text{for } 20 < \not{P}_T < 30\,\text{GeV}, \\ 0.55 & \text{for } \not{P}_T < 20\,\text{GeV}. \end{cases} \quad (5.29)$$

Figure 5.5 (c) and (d) show distributions of $\not{P}_T/E_T$ for the events with $\not{P}_T < 20\,\text{GeV}$ and with $20 < \not{P}_T < 30\,\text{GeV}$, respectively. It is noted that the cut on $\not{P}_T/E_T$ may reject multi-jet CC events. That's why we don't apply the cut for the events where backgrounds are negligible. This will be discussed in more detail in the study of hadronic final state by means of jet counting later in the section 5.9.3.

5.6.2 Tracking cuts

We defined a *good track* as a vertex-fitted track which has an polar angle of $15° < \theta^{trk} < 164°$ and has transverse momentum of $P_T^{trk} > 0.2\,\text{GeV}$. High γ events were required to have at least one good track,

$$\text{No. of good tracks} \geq 1. \quad (5.30)$$

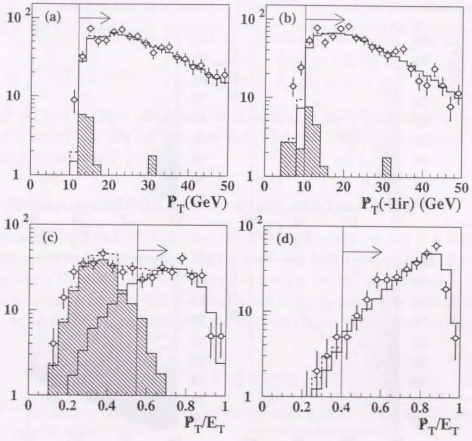

Figure 5.5: Distributions of: (a) $\not{P}_T$, (b) $\not{P}_T(-1ir)$, (c) $\not{P}_T/E_T$ for events with $\not{P}_T < 20\,\text{GeV}$, and (d) $\not{P}_T/E_T$ for events with $20 < \not{P}_T < 30\,\text{GeV}$, excluding only the cut from the final selection. The open circles indicate the data points, and the histogram with the solid line is the expectation from the CC MC normalized to the data luminosity. The shaded area indicates the expected contribution from the photoproduction, and the dotted lines indicates the sum of expectations from CC MCs and PhP MCs.

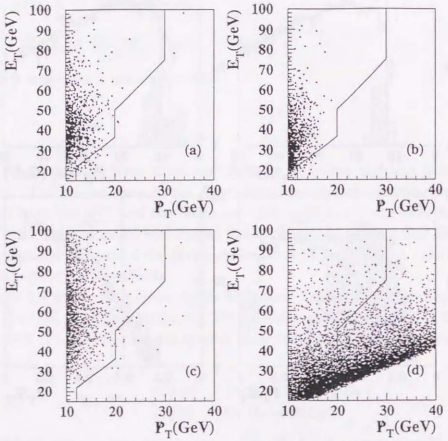

Figure 5.6: MC events in the high γ region are shown in $\not\!\!E_T$-E_T plane. (a) direct PhP, (b) resolved PhP, (c) neutral current DIS, and (d) charged current DIS. A cut of $Q^2 > 200\,\mathrm{GeV}^2$ was applied. Lumiosities for the background MCs are given in Table 3.4. Luminosity of the charged current MC is about 490 pb^{-1}.

Beam-gas events may have many tracks but a few of them are assigned to the primal vertex. These can be removed by

$$\text{No. of good tracks} > \frac{1}{4}\times(\text{No. of all tracks} - 20). \tag{5.31}$$

Figure 5.7 (a) shows events in (No. of good tracks)-(No. of all tracks) plane excluding the cut from the final candidate.

$\Delta\phi_{CAL-CTD}$ is defined as an azimuthal angle difference of $\not\!\!E_T$ directions between measured at the CAL and CTD. Only the good tracks are used in the $\not\!\!E_T$ calculation.

$$|\Delta\phi_{CAL-CTD}| < \begin{cases} 2.0 \text{ radian} & \text{for } \not\!\!E_T > 20\,\mathrm{GeV}, \\ 1.0 \text{ radian} & \text{for } \not\!\!E_T < 20\,\mathrm{GeV}. \end{cases} \tag{5.32}$$

Figure 5.7 (b) and (c) show distributions of $\Delta\phi_{CAL-CTD}$ for the events with $\not\!\!E_T < 20\,\mathrm{GeV}$ and with $\not\!\!E_T > 20\,\mathrm{GeV}$, respectively. This cut is effective to cosmic ray or halo-muon induced events.

5.6.3 Rejection of NC events using electron finder

Events were examined whether they are NC backgrounds or not if a candidate of DIS electron with energy greater than 4 GeV was found [60] and $E - P_Z$ of the event was larger than 30 GeV. Followings are criteria for NC background.
A cone with a radius of $R = \sqrt{\Delta\eta^2 + \Delta\phi^2} = 0.8$ in (η, ϕ)-plane was defined around the electron, and an energy isolation of the electron cluster in this cone was required as:

$$E^{cone} - E^e \leq 5\,\mathrm{GeV}, \tag{5.33}$$

where E^{cone} is the total energy deposited in the cone and E^e is the energy assigned to the electron cluster.
The polar angle of the electron(θ^e) is required to be greater than 15°. If the polar angle of the electron(θ^e) is more than 15° and less than 164°, as the CTD track efficiency is high in the region, only one matching track was required to be found in the cone defined above. The momentum of the matching track measured by the CTD($P^e{}_{trk}$) was required to be consistent with the energy measured in the CAL,

$$P^e{}_{trk}/E^e > 0.25. \tag{5.34}$$

When θ^e is greater than 164°,

$$E^e{}_T > 2\,\mathrm{GeV}, \tag{5.35}$$

was required where $E^e{}_T$ is the transverse energy of the electron candidate.
Events which satisfy the criteria were labeled as NC backgrounds, and hence were rejected.

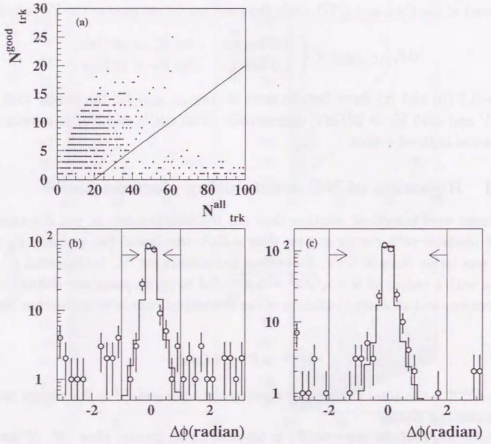

Figure 5.7: Distributions used in the track related cuts. (a) scatter plot in N^{all}_{trk}-N^{good}_{trk} plane, (b) $\Delta\phi$ for the events with $\not\!\!E_T < 20\,\mathrm{GeV}$, and (c) $\Delta\phi$ for the events with $\not\!\!E_T > 20\,\mathrm{GeV}$, excluding each cut from the final selection. The open circles indicate the data points, and the histograms indicate the expectation from the CC MC normalized to the data luminosity.

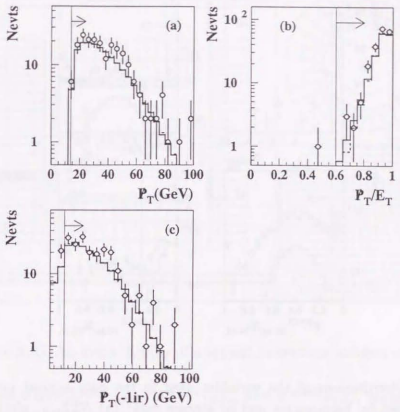

Figure 5.8: Distributions of $\not\!\!E_T$ related variables used in the low γ selection. (a) $\not\!\!E_T$, (b) $\not\!\!E_T/E_T$, and (c) $\not\!\!E_T(-1ir)$. The open circles indicate the data points, while the solid(dashed) lines are of CDM(MEPS) MC sample. The thresholds are indicated as lines and arrows in each of the figures.

5.7 Low γ selection

5.7.1 $\not\!\!E_T$ and $\not\!\!E_T/E_T$ requirements

The thresholds for $\not\!\!E_T$, $\not\!\!E_T(-1ir)$ and $\not\!\!E_T/E_T$ cuts were set higher than the high γ selection as:

$$\not\!\!E_T > 14\,\mathrm{GeV}, \tag{5.36}$$

$$\not\!\!E_T(-1ir) > 12\,\mathrm{GeV}, \tag{5.37}$$

$$\not\!\!E_T/E_T > 0.6 \quad \text{for } \not\!\!E_T < 30\,\mathrm{GeV}. \tag{5.38}$$

Figure 5.8 shows these distributions. Data and MC agree reasonably well.

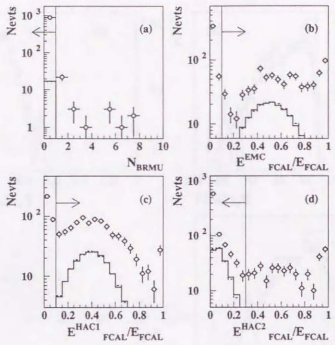

Figure 5.9: Distributions of the variables used in the cuts against non-*ep* backgrounds induced by halo-muons and by cosmic rays: (a) N^{trk}_{BRMU}, plotted only in the case $N^{trk}_{CTD} = 0$, (b) E^{EMC}_{FCAL}/E_{FCAL}, (c) E^{HAC1}_{FCAL}/E_{FCAL}, and (d) E^{HAC2}_{FCAL}/E_{FCAL}. The open circles indicate the data points, and the solid line is the CDM MC sample while the dotted line is the MEPS sample. The MC distributions are normalized to the data luminosity. Cuts were made as indicated as the lines and the arrows in the figures.

5.7.2 Cuts against halo-muons and cosmic-rays

A large amount of background coming into the low γ region was found to be halo-muon and cosmic ray induced events. Figure 5.9 (a) shows the number of tracks reconstructed in the Barrel and Rear Muon Chambers(N^{trk}_{BRMU}) when tracks are not reconstructed in the CTD.

$$N^{trk}_{BRMU} = 0 \quad \text{for } N^{trk}_{CTD} = 0, \tag{5.39}$$

was required to remove cosmic-ray events. Figure 5.9 (b), (c), and (d) show the energy fraction of EMC, HAC1, and HAC2 in the FCAL, respectively.

$$E^{EMC}{}_{FCAL}/E_{FCAL} > 0.1, \tag{5.40}$$
$$E^{HAC1}{}_{FCAL}/E_{FCAL} > 0.1, \tag{5.41}$$
$$E^{HAC2}{}_{FCAL}/E_{FCAL} < 0.3, \tag{5.42}$$

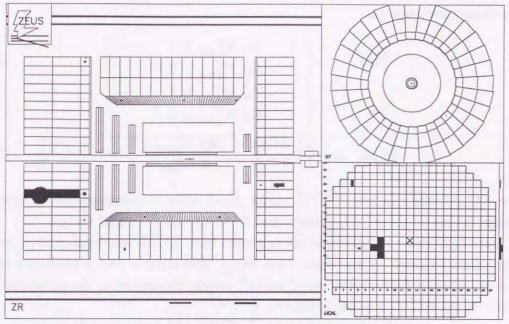

Figure 5.10: An event display of a typical halo-muon induced events.

were required where $E^{EMC}{}_{FCAL}$, $E^{HAC1}{}_{FCAL}$, and $E^{HAC2}{}_{FCAL}$, represent the sum of the energy deposited in the FCAL EMC, HAC1, and HAC2 cells, respectively.

Considerable amount of background still remains in the selected sample even after these requirements. It consists mostly of the halo-muon events. Figure 5.10 shows a typical halo-muon event. To remove them, a cluster of FCAL energy deposits was constructed in a following manner. Treating four EMC cells in the same tower as one cell, the cell which has a maximum transverse energy among all cells was selected as a seed cell. Energy deposit in cells which surround the seed cell were examined. When the energy was smaller than the one of the seed(but larger than 100 MeV), the cell was merged to the seed. The procedure was repeated until the cluster stopped to grow up.

Then, the following variables were defined to qualify the shower width of the cluster:

$$N_{wid}{}^{t} \equiv max|t^i - t^0|, \tag{5.43}$$
$$N_{wid}{}^{m} \equiv max|m^i - m^0|, \tag{5.44}$$
$$E_{Twid}{}^{r} \equiv \sum_i E_T{}^i \cdot \sqrt{(m^i - m^0)^2 + (t^i - t^0)^2}, \tag{5.45}$$

where i runs over all cells which belong to the cluster, t_i is the tower number of the cell, $E_T{}^i$ is the transverse energy in the cell, and the subscript 0 represents the center cell.

As shown in the figure 5.10, the shower width of the halo-muon events is narrow in

transverse; events were required to have sufficiently wide shower width in transverse using these quantities as:

$$N_{wid}{}^{t} > \begin{cases} 1 & \text{for } N^{F}_{mtrk} \geq 1 \\ 2 & \text{for } N^{F}_{mtrk} = 0 \end{cases}, \tag{5.46}$$

$$N_{wid}{}^{m} > \begin{cases} 1 & \text{for } N^{F}_{mtrk} \geq 1 \\ 2 & \text{for } N^{F}_{mtrk} = 0 \end{cases}, \tag{5.47}$$

$$E_{Twid}{}^{t} > \begin{cases} 6\,\text{GeV} & \text{for } N^{F}_{mtrk} \geq 1 \\ 10\,\text{GeV} & \text{for } N^{F}_{mtrk} = 0 \end{cases}, \tag{5.48}$$

where N^{F}_{mtrk} is the number of CTD tracks which have closest approach distance of less than 30 cm to the FCAL cluster, and fit to the CTD primal vertex.

Figure 5.10 also indicates that some events have RCAL energy deposits(usually a mip cluster) caused by the same halo-muon. Denoting x and y positions of the center cell of the FCAL cluster as x^0 and y^0, energy deposited in the corresponding position in the RCAL was calculated as:

$$\text{RasoE} \equiv \sum_{i}^{\sqrt{(x^i-x^0)^2+(y^i-y^0)^2}<30cm} E^i, \tag{5.49}$$

where i runs on all RCAL cells with $x(y)^i$ is the $x(y)$ coordinate of the cell center. A requirement was made as:

$$\text{RasoE} < 0.1\,\text{GeV} \quad \text{for } N^{F}_{mtrk} = 0. \tag{5.50}$$

No requirement on RasoE was imposed when there were any matching tracks to the FCAL cluster.

Figure 5.11 shows these distributions for the $N^{F}_{mtrk} > 0$ sample after all selection cuts except the shower shape cuts. Figure 5.12 shows the same distributions for the $N^{F}_{mtrk} = 0$ sample. It indicates significant backgrounds. This is why we imposed the tighter thresholds for such events. In the figure 5.12 (e), the arrival time measured by RCAL is shown when energy is deposited in the RCAL. The halo-muon contribution is illustrated clearly by the early arriving time to the RCAL; the halo-muons hit from behind the RCAL before reaching to the nominal interaction point, while the time zero is calibrated to be hit in front of the RCAL after interacted at the nominal interaction point. Figure 5.13 shows the same distributions after requiring the shower shape cuts as well as the cut on the RCAL energy associated to the FCAL cluster. Then, the distributions between the data and MC agree well. There is no events left which have energy in the RCAL.

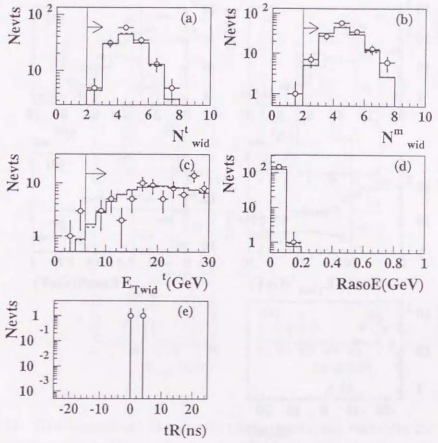

Figure 5.11: Distributions of the shower shape qualifying variables for the events with one or more matching CTD tracks to the FCAL cluster without applying any of the (a) $N_{wid}{}^{t}$, (b) $N_{wid}{}^{m}$ (c) $E_{Twid}{}^{t}$ cuts. The open circles indicate the data, and the solid(dashed) lines are as CDM(MEPS) MC distribution normalized to the data luminosity. Cuts were made as indicated as the lines and the arrows in the figures. (d) RasoE, (e) tR are not used in the cuts; plotted for an illustration.

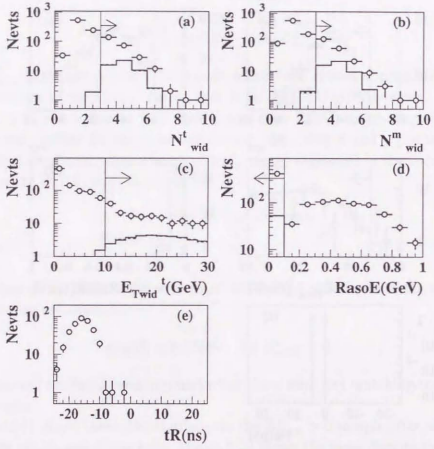

Figure 5.12: Distributions of the shower shape qualifying variables for the events without any matching CTD tracks to the FCAL cluster without applying any of the (a) $N_{wid}{}^t$, (b) $N_{wid}{}^m$ (c) $E_{Twid}{}^t$, (d) RasoE cuts. The open circles indicate the data, and the solid(dashed) lines are as CDM(MEPS) MC distribution normalized to the data luminosity. Cuts were made as indicated as the lines and the arrows in the figures. (c) tR is not used in the cut; plotted for an illustration.

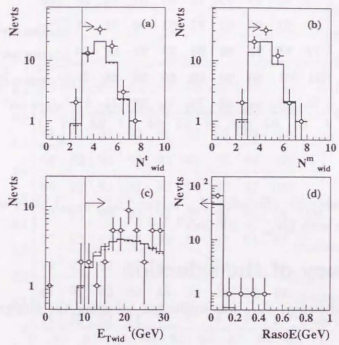

Figure 5.13: Distributions of the shower shape qualifying variables for the events without any matching CTD tracks to the FCAL cluster releasing only the corresponding cut from the final selection. (a) $N_{wid}{}^t$, (b) $N_{wid}{}^m$ (c) $E_{Twid}{}^t$. The open circles indicate the data, and the solid(dashed) lines are as CDM(MEPS) MC distribution normalized to the data luminosity. Cuts were made as indicated as the lines and the arrows in the figures. Since there is no event with energy deposited in RCAL, the timing at the RCAL is not plotted.

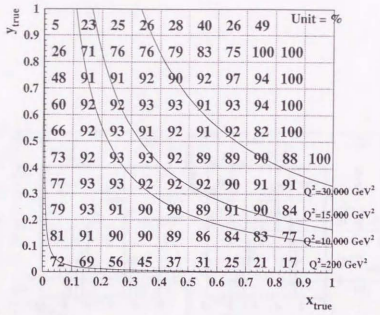

Figure 5.14: The selection efficiency $\mathcal{E}_{sel}$ in the (x_{true}-y_{true}) plain evaluated using the CC MC sample with $Q^2_{true} \geq 200\,\mathrm{GeV}^2$.

5.8 Efficiency of the selection

The selection efficiency, $\mathcal{E}_{sel}$, was evaluated by using the charged current MC sample as:

$$\mathcal{E}_{sel} = \frac{\text{No. of events generated in the bin and passed the CC selection}}{\text{No. of events generated in the bin}}. \quad (5.51)$$

It includes the trigger efficiency.

Figure 5.14 shows $\mathcal{E}_{sel}$ in the x_{true}-y_{true} plane for the events with $Q^2_{true} \geq 200\,\mathrm{GeV}^2$. The efficiency is greater than 90% in almost all kinematic region. The loss of the efficiency at high y_{true} is due to the explicit y cut.

To demonstrate our special treatment for the low γ events is effective, Figure 5.15 shows the selection efficiency if we apply the high γ selection even for low γ events. A big deterioration in efficiency was observed in low γ(high-x and low-y) region, compared with the Figure 5.14.

5.9 Distributions of the selected events

After all the selection cuts described in the former sections, events were visually scanned. Twelve among selected 1100 events were removed as consistent with cosmic

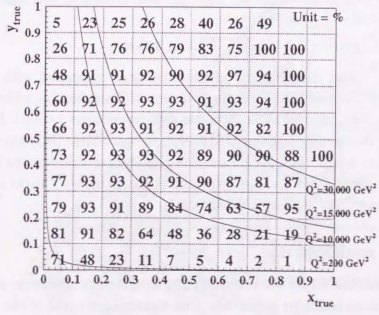

Figure 5.15: The selection efficiency $\mathcal{E}_{sel}$ in the (x_{true}-y_{true}) plane when the high γ selection was applied for all kinematic region. A loss of efficiency is seen in the low γ, i.e. the high x and low y, region.

ray or halo-muon induced events. In total, 1088 events were remained as the final candidates, which consist of 889 high γ events and of 199 low γ events.

5.9.1 Kinematic variables

Figure 5.16 shows the final candidates in the (x, Q^2) kinematic plane. The open circles represent the high γ events and the closed circles represent the low γ events. For an illustration, a line of $\gamma = 0.4$ is also drawn in the figure.

Figure 5.17 shows the distributions of kinematic variables: $\not{P}_T$, γ, $E-P_Z(=y/2E_e)$, Q^2, and x. The data points are superimposed on the sum of the charged current and background MC expectations. The data agreed well with the MC expectation in general, but showed an excess at: high $\not{P}_T$, low γ, high x, and high Q^2.

5.9.2 CAL energies and CTD tracks

Figure 5.18 shows distributions of CAL energies compared with expectations both from the CDM and MEPS charged current MC samples by adding those from the background MC samples. The data are well reproduced by both MCs.

Figure 5.19 shows distributions of CTD related variables. Only the high γ events contribute to the figure. The MEPS sample gives better descriptions for the multiplicities of the vertex fitted and good tracks. The data shows a slight shift to higher multiplicity of all CTD tracks than both MCs.

5.9.3 Jet multiplicity

Jets were searched for by the longitudinally invariant k_T clustering algorithm [61]. In contrast to cone-based jet algorithm, this clustering algorithm has an advantage that it can avoid umbigities in the choice of the jet seed and in the the treatment for overlapped jets. The transverse energy($E_T{}^{jet}$), pseudo-rapidity(η^{jet}), and azimuthal angle(ϕ^{jet}) of the jet were defined according to the Snowmass convention as:

$$E_T{}^{jet} = \sum_i E_T{}^i, \tag{5.52}$$

$$\eta^{jet} = \frac{1}{E_T{}^{jet}} \sum_i E_T{}^i \eta^i, \tag{5.53}$$

$$\phi^{jet} = \frac{1}{E_T{}^{jet}} \sum_i E_T{}^i \phi^i. \tag{5.54}$$

The sums run over all energy corrected cone-islands which are assigned to the jet. For the further analysis, only jets with $E_T{}^{jet} > 6\,\mathrm{GeV}$ and with $\eta^{jet} < 2.5$ are considered.

Figure 5.20 shows the jet multiplicity, the inclusive $E_T{}^{jet}$ and η^{jet} distributions compared with the MC expectations from the CDM and MEPS models. The data

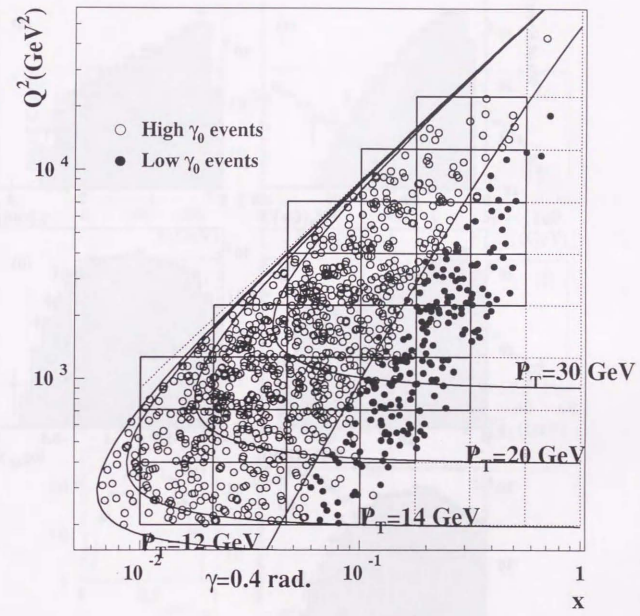

Figure 5.16: Scatter plot of the selected 1088 CC candidates in (x, Q^2) plane. The open circles represent the 889 high γ events and the closed circles represent the 199 low γ events. Various $\not{P}_T$ lines are also drawn: the $\not{P}_T = 12(14)$ GeV is the threshold for high(low) γ selection and the $\not{P}_T = 20$ GeV is that for the definition of low $\not{P}_T$ region where the tight photoproduction cuts are applied. The $\gamma = 0.4$ line is also drawn for an illustration of the switching point for high and low γ selections. The dotted lines denote the bin boundaries for the cross section measurements of $d\sigma/dQ^2$ and $d\sigma/dx$. The bins used for the double differential cross section measurement are indicated with the solid lines. (This will be explained detail in the section 6.2.)

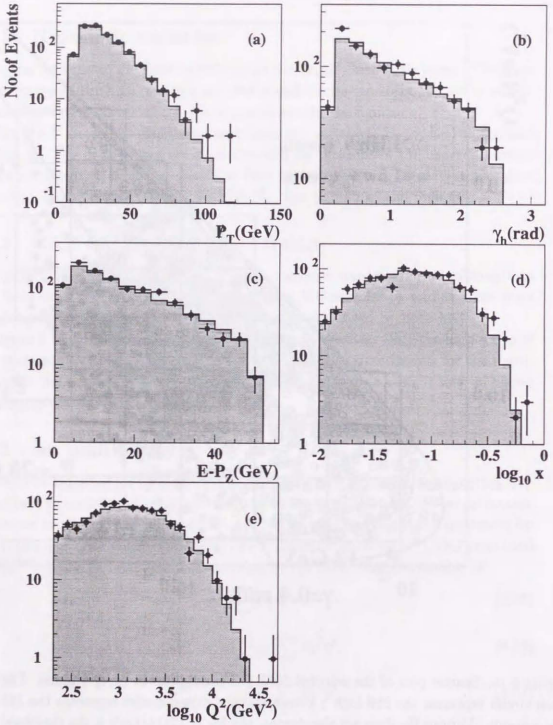

Figure 5.17: Distributions of kinematic variables. The closed circles represent the selected CC candidates and the histograms represent the sum of the CC and background MC expectations. MCs are normalized to the data luminosity of 46.6 pb^{-1}.

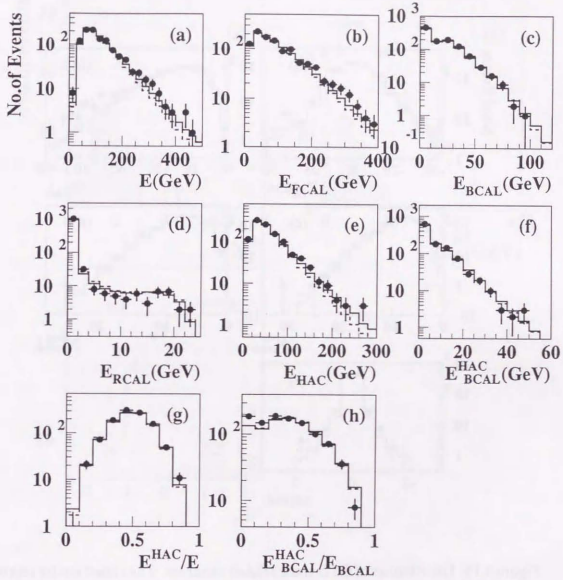

Figure 5.18: Distribution of various CAL energies. The closed circles represent the selected CC candidates and the solid(dashed) lines represent the expectation of the CDM(MEPS) MC sample. MCs are normalized to the data luminosity of 46.6 pb^{-1}.

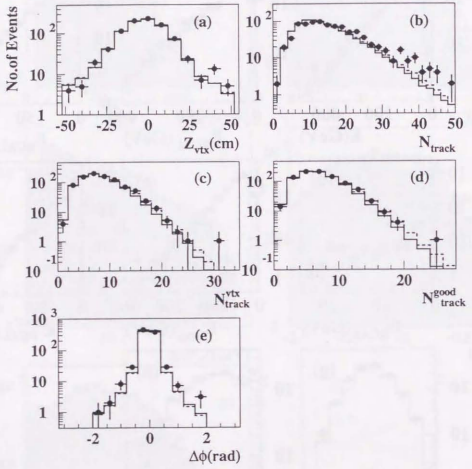

Figure 5.19: Distribution of CTD track related variables. The closed circles represent the selected CC candidates and the solid(dashed) lines represent the expectation of the CDM(MEPS) MC sample. MCs are normalized to the data luminosity of 46.6 pb^{-1}.

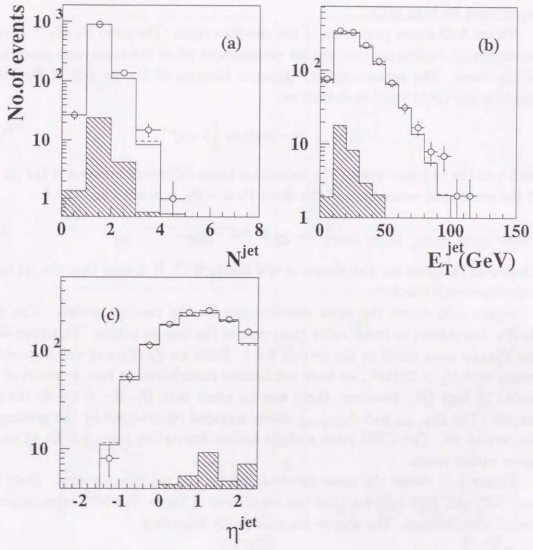

Figure 5.20: Jet properties of the final CC candidates compared with MC simulations both by the CDM and MEPS parton shower models. (a) jet multiplicity, (b) inclusive $E_T{}^{jet}$, (c) inclusive η^{jet} distributions. The open circles indicate the data points. The shaded area indicates the expectation from background MCs. The histograms with solid(dashed) line indicate the sum of CDM(MEPS) and background MC expectations.

suggests more multi-jet events than both MCs. The η^{jet} has an excess at the forward region of $2.0 < \eta^{jet} < 2.5$. To study further, events are classified to four samples, i.e. no-jet, one-jet, two-jet, and multi-jet samples.

Figure 5.21 shows kinematic quantities of the no-jet events. All events are clustered in low γ region. Both of the event rate and the event kinematics are well reproduced by both MCs.

Figure 5.22 shows properties of the one-jet events. The ratio $\not{P}_T/E_T{}^{jet}$ clusters around unity, indicating that the jet owes almost all of the transverse momentum of the event. The pseudo-rapidity distance between of the jet and of the struck quark(in the QPM view) is defined as:

$$\Delta\eta_{\gamma-jet} \equiv -\log(\tan\frac{\gamma}{2}) - \eta^{jet}, \tag{5.55}$$

with γ as the hadronic angle. The azimuthal angle difference between of the jet and of the transverse momentum of the event $P_T \equiv -\not{P}_T$ is defined as:

$$\Delta\phi_{P_T-jet} \equiv \phi_{P_T} - \phi_{jet}. \tag{5.56}$$

These two variables are also shown in the Figure 5.22. It is seen that the jet represents the struck quark.

Figure 5.23 shows the same distributions for the two-jets events. The ratio $\not{P}_T/E_T$ has shifted to lower value than that of the one-jet events. This correlation has already been noted in the section 5.6.1. Since no $\not{P}_T/E_T$ cut was imposed for events with $\not{P}_T > 30$ GeV, we have not limited sensitivities to two- or multi-jet CC events at high Q^2. However, there was no event with $\not{P}_T/E_T < 0.4$ in the final sample. The $\Delta\eta_{\gamma-jet}$ and $\Delta\phi_{P_T-jet}$ shows smeared correlations by the presence of the second jet. The CDM gives a slight better description though both of models agree within errors.

Figure 5.23 shows the same distributions for the multi-jets events. Both Figures 5.23 and 5.24 indicate that the event rate is higher the MC expectations in overall distributions. The shapes are reasonably described.

5.9.4 Large Rapidity Gap events

The usual DIS events have energy deposits near the forward beam pipe. It comes from the energy flow between the proton remnant and struck quark by the color connection. However, it was observed about 10% of NC-DIS events has a large rapidity area in the forward direction where no energy flow is observed [62]. This type of events, called as "large rapidity gap(LRG) events", are understood as mainly contributed from diffractive processes [63]. It is interesting whether the LRG events are also observed in charged current process or not.

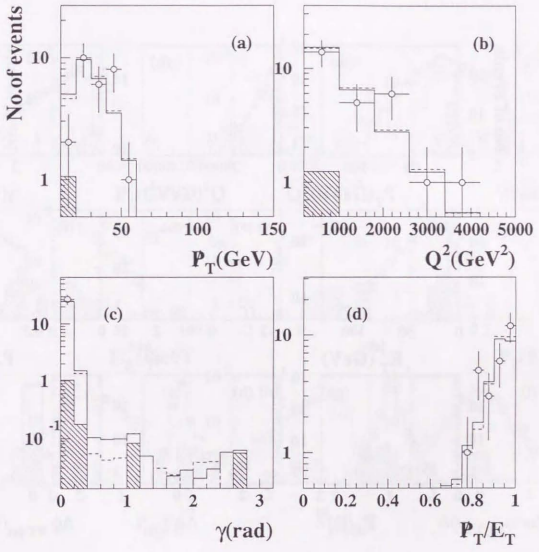

Figure 5.21: Event kinematics of the no-jet events compared with MC simulations both by the CDM and MEPS parton shower models. (a) $\not{P}_T$, (b) Q^2, (c) γ, (d) $\not{P}_T/E_T$. The open circles indicate the data points. The shaded area indicates the expectation from background MCs. The histograms with solid(dashed) line indicate the sum of CDM(MEPS) and background MC expectations.

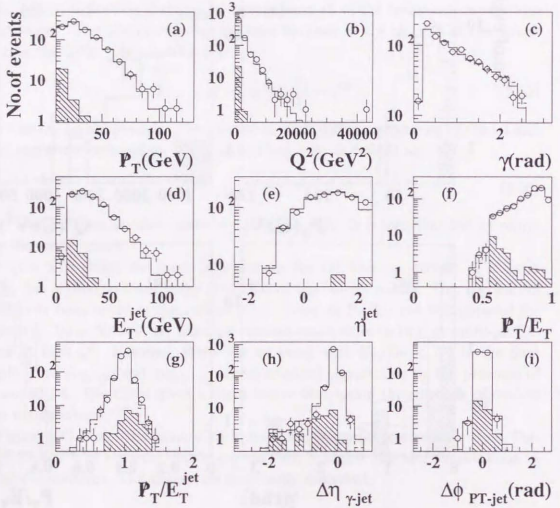

Figure 5.22: Kinematics and jet properties of the one-jet events compared with MC simulations both by CDM and MEPS parton shower models. (a) $\not\!\!E_T$, (b) Q^2, (c) γ, (d) $E_T{}^{jet}$, (e) η^{jet}, (f) $\not\!\!E_T/E_T$, (g) $\not\!\!E_T/E_T{}^{jet}$, (h) $\Delta\eta_{\gamma-jet}$, (i) $\Delta\phi_{P_T-jet}$. The open circles indicate the data points. The shaded area indicates the expectation from background MCs. The histograms with solid(dashed) line indicate the sum of CDM(MEPS) and background MC expectations.

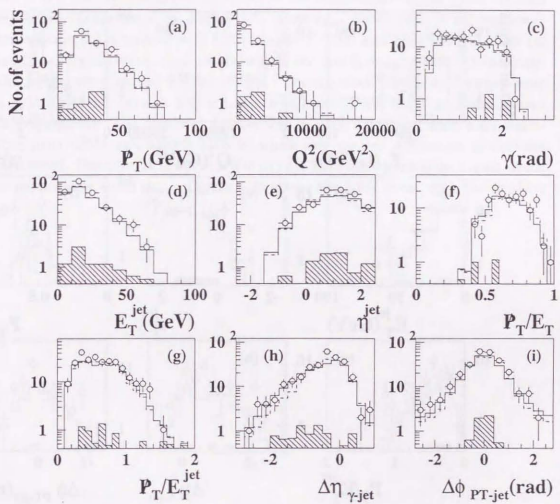

Figure 5.23: Kinematics and jet properties of the two-jet events compared with MC simulations both by CDM and MEPS parton shower models. (a) $\not\!\!E_T$, (b) Q^2, (c) γ, (d) $E_T{}^{jet}$, (e) η^{jet}, (f) $\not\!\!E_T/E_T$, (g) $\not\!\!E_T/E_T{}^{jet}$, (h) $\Delta\eta_{\gamma-jet}$, (i) $\Delta\phi_{P_T-jet}$. The open circles indicate the data points. The shaded area indicates the expectation from background MCs. The histograms with solid(dashed) line indicate the sum of CDM(MEPS) and background MC expectations.

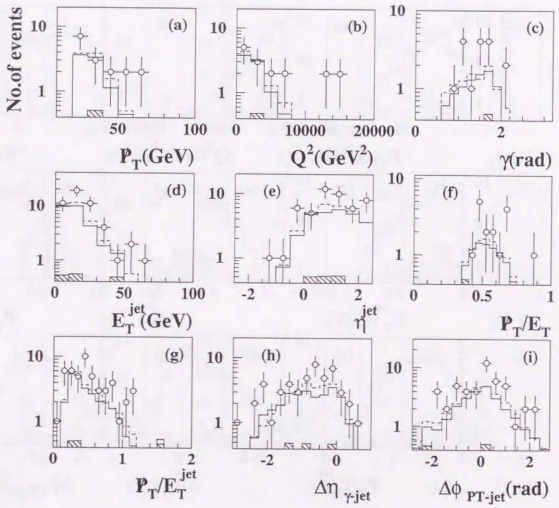

Figure 5.24: Kinematics and jet properties of the multi-jet events compared with MC simulations both by CDM and MEPS parton shower models. (a) $\not\!\!P_T$, (b) Q^2, (c) γ, (d) $E_T{}^{jet}$, (e) η^{jet}, (f) $\not\!\!P_T/E_T$, (g) $\not\!\!P_T/E_T{}^{jet}$, (h) $\Delta\eta_{\gamma-jet}$, (i) $\Delta\phi_{P_T-jet}$. The open circles indicate the data points. The shaded area indicates the expectation from background MCs. The histograms with solid(dashed) line indicate the sum of CDM(MEPS) and background MC expectations.

The maximum pseudo-rapidity among all calorimeter cells with energy of greater than 400 MeV is denoted as η_{max}. We defined the LRG event as:

$$\eta_{max} < 2.5, \tag{5.57}$$

$$\cos\theta_h \equiv \frac{\sum_i {P_Z}^i}{\sum_i E^i} < 0.75, \tag{5.58}$$

where $E^i({P_Z}^i)$ is the energy(z-component of the momentum) of cell i and the sum runs over all calorimeter cells. Figure 5.25 shows η_{max} distribution in (a) and $\cos\theta_h$ distribution in (b) compared with both models of CDM and MEPS. Figure 5.25 (c) shows the charged current final candidates in the ($\cos\theta_h$-η_{max}) plane. As indicated in the figure, we observed 8 LRG events. The expected numbers of events were $5.31 \pm 0.21(3.88 \pm 0.18)$ and 1.83 ± 1.34 events from CDM(MEPS) and background MCs, respectively. The observed number was in good agreement with both expectations from CDM and MEPS MCs in which any explicit diffraction models are implemented. However, it is worth while to note that there were some events which have particularly small η_{max}. Figure 5.26 shows the LRG event with the smallest η_{max}.

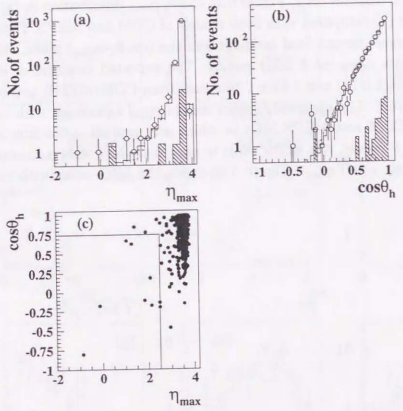

Figure 5.25: Distributions of the LRG defining variables: (a) η_{max} and (b) $\cos\theta_h$. The open circles indicate the data. The shaded area indicates expectation from background MCs. The histograms with solid(dotted) line indicate the sum of expectations of CDM(MEPS) and background MCs. Plot (c) shows the CC final candidates in $\cos\theta_h$-η_{max}. The box cut: $\eta_{max} < 2.5$ and $\cos\theta_h < 0.75$ shown in the figure gives the definition of LRG event. Eight events passed the criteria.

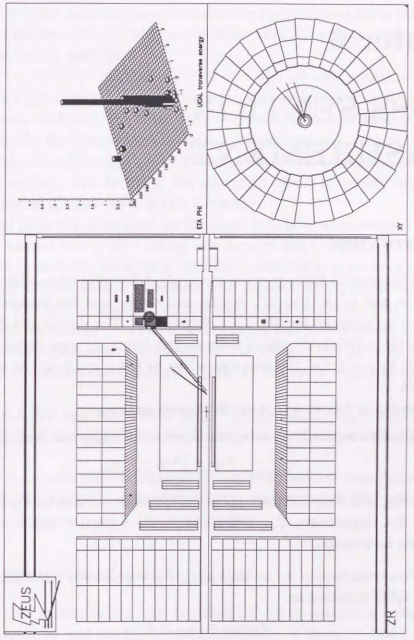

Figure 5.26: The LRG event with the smallest η_{max}. It has $\eta_{max} = -0.86$, $\cos\theta_h = -0.8$, $\not{P}_T = 15.1\,\mathrm{GeV}$, and $Q^2 = 1520\,\mathrm{GeV}^2$.

Chapter 6

CROSS SECTION MEASUREMENT

6.1 Overview

What we measure in this paper are the single differential cross sections as functions of Q^2, x, and y, i.e. $d\sigma/dQ^2$, $d\sigma/dx$, and $d\sigma/dy$, and the double differential cross sections in terms of (x, Q^2), i.e. $d^2\sigma/dxdQ^2$. The $d\sigma/dx$ and $d\sigma/dy$ were defined with $Q^2 \geq 200\,\mathrm{GeV}^2$. All of them except for $d\sigma/dy$ were defined to be extrapolated up to $y = 1$; i.e. the acceptance loss by the $y < 0.9$ cut(see section 5.5) was corrected.

We proceeded as follows to obtain these cross sections.

1. The radiative cross section integrated over a bin σ_{RAD} was derived as:

$$\sigma_{RAD} = \frac{\mathcal{C}_{acc} \times (\mathrm{N}_{obs} - \mathrm{N}_{BG})}{\mathcal{L}^{data}}, \tag{6.1}$$

   where N_{obs} and N_{BG} are the numbers of the observed and background events in the bin, respectively. $\mathcal{C}_{acc}$ is the acceptance correction factor, and $\mathcal{L}^{data}$ is the data luminosity.

2. The Born cross section in the bin σ_{BORN} was obtained by correcting the effect of the QED radiation as:

$$\sigma_{BORN} = \mathcal{C}_{rad} \times \sigma_{RAD}, \tag{6.2}$$

   where the $\mathcal{C}_{rad}$ is the radiative correction factor.

3. Then, the integrated cross section was converted to the differential one at the reference point e.g. for $d^2\sigma/dxdQ^2$ as:

$$\frac{d^2\sigma}{dxdQ^2}\Big|_{\text{ref-point}} = \frac{\sigma_{BORN}}{\sigma^{SM}_{BORN}} \times \frac{d^2\sigma}{dxdQ^2}^{SM}_{BORN}\Big|_{\text{ref-point}}, \tag{6.3}$$

   where the subscript SM represents the SM predictions.

6.2 Resolutions and bin definitions

Resolution of the kinematic variables and the statistics of the data sample are to be considered in defining the bin width. Too fine bins will let larger event migrations and lack of statistics, and too coarse bins will lose the sensitivity of the measurement. We took the widths of bins to be typically wider than one standard deviation of the kinematic variable's resolution.

From $Q^2 = 400\,\mathrm{GeV}^2$ to $28000\ \mathrm{GeV}^2$, 7 bins was set with logarithmically equal widths. In addition, we set the lowest bin from $Q^2 = 200\,\mathrm{GeV}^2$ to $Q^2 = 400\,\mathrm{GeV}^2$ and the highest bin from $Q^2 = 28000\,\mathrm{GeV}^2$ to $Q^2 = 60000\,\mathrm{GeV}^2$. Reason for the special treatment for the lowest region is that considerable amount with an order of 10% contamination of backgrounds are clustered in the lowest Q^2 region, as it is shown in the next section. The fact that the resolution of the kinematic reconstruction becomes worse as Q^2 gets lower is also a reason.

The lower limit of x to be used for the cross section measurements of $d\sigma/dx$ and $d^2\sigma/dxdQ^2$ was set to $x = 10^{-2}$ taking into account the threshold of the $\not{P}_T$ cut as shown in the figure 5.16. Since the x resolution improves as x grows as already seen in the section 4.6, we defined three bins with logarithmically equal widths from x 10^{-2} to 10^{-1} and four bins with logarithmically equal widths from 10^{-1} to 10^{0}.

For $d\sigma/dy$, we divided y to two from 0.0 to 0.2 and to five from 0.2 to 0.9 with equal bin width respectively. We set smaller bin width in the low y region from 0.0 to 0.2 since the cross section changes rapidly in the low y region as shown in the chapter 8.

Figures 6.1, 6.2, and 6.3 present $(Q^2_{rec} - Q^2_{true})/Q^2_{true}$, $(x_{rec} - x_{true})/x_{true}$, and $(y_{rec} - y_{true})/y_{true}$ in each of the bins for the events which pass the CC selection, respectively.

Bins for the double differential cross section measurement were defined with the same x and Q^2 boundaries as used in the the $d\sigma/dx$ and $d\sigma/dQ^2$ measurements. Figure 5.16 represents those in the (x, Q^2) plane.

6.3 Background subtraction

The amount of the background contamination was evaluated using the background MC samples, and was subtracted statistically. It was estimated to be at most 2-3% in all kinematic region except for the lowest Q^2 region $200 < Q^2 < 400\,\mathrm{GeV}^2$. A summary is given in the table 6.1 for the $d\sigma/dQ^2$ measurement.

The NC contribution is well removed. The single W production contributes in all Q^2 region, however, can be neglected due to the small production cross section. Backgrounds from the photoproduction and di-lepton production become large at lower Q^2; the photoproduction gives the largest contribution of about 10% contamination at the lowest Q^2.

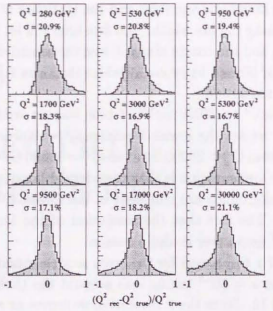

Figure 6.1: Resolutions of the measured Q^2, $(Q^2_{rec} - Q^2_{true})/Q^2_{true}$, in each bins of Q^2_{true}. The lines indicate the bin boundaries.

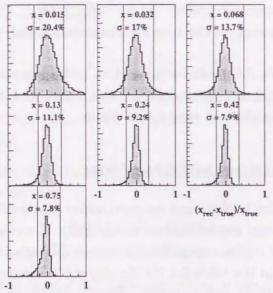

Figure 6.2: Resolutions of the measured x, $(x_{rec} - x_{true})/x_{true}$, in each bins of x_{true}. The lines indicate the bin boundaries.

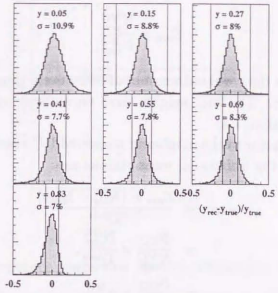

Figure 6.3: Resolutions of the measured y, $(y_{rec} - y_{true})/y_{true}$, in each bins of y_{true}. The lines indicate the bin boundaries.

Table 6.1: The background contamination in each of Q^2 bins.

Q^2_{min}	200.	400.	711.	1265.	2249.	4000.	7113.	12649.	22494.
Q^2_{max}	400.	711.	1265.	2249.	4000.	7113.	12649.	22494.	60000.
N_{obs}	138	173	248	204	174	91	46	13	1
PhP	10.7	2.2	0.9	-	0.9	-	0.4	-	-
NC-DIS	-	-	-	0.4	0.4	-	-	-	-
di-lepton	5.4	2.5	0.4	0.6	0.06	0.08	-	-	-
$W^{\pm}$	0.4	0.6	0.9	1.3	1.0	0.6	0.3	0.11	0.01
total BGs	16.5	5.3	2.3	2.3	2.4	0.6	0.7	0.11	0.01

6.4 Acceptance correction

We adopt the bin-by-bin acceptance correction. The acceptance correction factor C_{acc} was evaluated using the charged current MC samples as:

$$C_{acc} = \frac{N^{MC}_{gen}}{N^{MC}_{exp}}. \tag{6.4}$$

The $N^{MC}_{gen(exp)}$ denotes the weighted number of MC events generated(expected to be measured) in the bin. The MC weights were normalized to the data luminosity according to the equation 3.4.
By multiplying this factor to the number of measured CC events, the radiative cross section integrated in the bin, σ_{RAD}, was obtained as:

$$\sigma_{RAD} = \frac{C_{acc} \times (N_{obs} - N_{BG})}{\mathcal{L}^{data}}, \tag{6.5}$$

$$= \frac{N_{CC}}{N^{MC}_{exp}} \times \frac{N^{MC}_{gen}}{\mathcal{L}^{data}}, \tag{6.6}$$

$$= \frac{N_{CC}}{N^{MC}_{exp}} \times \sigma^{MC}_{RAD}, \tag{6.7}$$

where $N_{CC} \equiv N_{obs} - N_{BG}$ is the number of events after background was subtracted, and $\mathcal{L}^{data}$ is the data luminosity. The $\sigma^{MC}_{RAD} \equiv \frac{N^{MC}_{gen}}{\mathcal{L}^{data}}$ is the SM radiative cross section evaluated using the MC events.

In addition to the acceptance correction factor, two quantities are used to qualify the correction.
The purity $\mathcal{P}$ is defined as:

$$\mathcal{P} = \frac{\text{No. of events generated and measured in the same bin}}{\text{No. of events measured in the bin}}. \tag{6.8}$$

Higher of purity indicates smaller contribution from the migration into a bin.
The efficiency $\mathcal{E}$ is defined as:

$$\mathcal{E} = \frac{\text{No. of events generated and measured in the same bin}}{\text{No. of events generated in the bin}}, \tag{6.9}$$

$$= \mathcal{E}_{sel} \times \mathcal{E}_{mig}, \tag{6.10}$$

where $\mathcal{E}_{sel}$ is the selection efficiency as defined in the section 5.8, and $\mathcal{E}_{mig}$ is the migration efficiency defined as:

$$\mathcal{E}_{mig} = \frac{\text{No. of events generated and measured in the same bin}}{\text{No. of events generated in the bin and passed the CC selection}}. \tag{6.11}$$

The migration efficiency qualifies the migration from the bin after the event is selected. The higher efficiency indicates the higher selection efficiency and the smaller

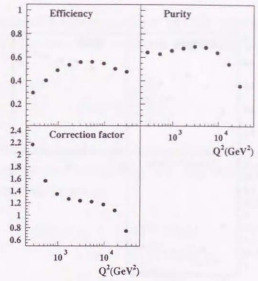

Figure 6.4: The acceptance correction factors, efficiencies and purities for the $d\sigma/dQ^2$ measurement.

event migration from the bin.
The purity and efficiency are related to the acceptance correction factor as:

$$C_{acc} = \frac{\mathcal{P}}{\mathcal{E}}. \tag{6.12}$$

Both high efficiency and high purity provide a good measurement; with high selection efficiency and small migrations.

Figure 6.4 shows the acceptance correction factors, efficiencies, and purities for the $d\sigma/dQ^2$ measurement. The purities are better than 0.6 except for the high Q^2 region of $Q^2 \geq 10000\,\text{GeV}^2$. The behavior can be understood as a reflection of the steep fall off of the cross section in the high Q^2 region which lets more migrations from the lower. The acceptance correction is lower than unity at the highest Q^2 as a consequence of the migration. The efficiency becomes lower at lower Q^2 reflecting the loss of the selection efficiency. Figure 6.5 presents the factors for the $d\sigma/dx$ measurement. The efficiency is reduced in both the lower and higher regions. This leads to large correction factors of close to three at the highest x and close to two at the lowest x. The purity is kept to be higher than 65% in all kinematic region, and improves up to 90% at the higher x region.

Figure 6.6 presents the factors for the $d\sigma/dy$ measurement. The purities are better than 0.6 in all region. The efficiency goes lower as y goes higher; down to 20% at the highest y bin.

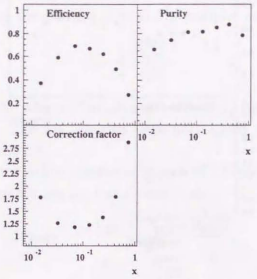

Figure 6.5: The acceptance correction factors, efficiencies and purities for the $d\sigma/dx$ measurement.

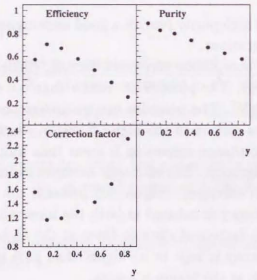

Figure 6.6: The acceptance correction factors, efficiencies and purities for the $d\sigma/dy$ measurement.

6.5 Radiative correction

The Born level cross section integrated over the bin was obtained by correcting for the effect of the QED radiation. The radiative correction factor $\mathcal{C}_{rad}$ was evaluated as:

$$\mathcal{C}_{rad} = \frac{\sigma^{SM}_{BORN}}{\sigma^{SM}_{RAD}}, \tag{6.13}$$

where σ^{SM}_{BORN} is the SM Born level cross section integrated over the bin, and σ^{SM}_{RAD} is the SM radiative cross section integrated over the bin. The measured Born level cross section, σ_{BORN}, was obtained as:

$$\sigma_{BORN} = \mathcal{C}_{rad} \times \sigma_{RAD}, \tag{6.14}$$

$$= \frac{\sigma_{RAD}}{\sigma^{SM}_{RAD}} \times \sigma^{SM}_{BORN}. \tag{6.15}$$

We evaluated the radiative cross section using the same MC events as used in the acceptance calculation; i.e. $\sigma^{SM}_{RAD} = \sigma^{MC}_{RAD}$. Inserting equation 6.7,

$$\sigma_{BORN} = \frac{N_{CC}}{N^{MC}_{exp}} \times \sigma^{SM}_{BORN}. \tag{6.16}$$

6.6 Bin centering correction

The Born cross section integrated over a bin as obtained in the former section was converted to the differential one at a reference point in the bin. We took the bin center for the reference point; logarithmic center was chosen for the $d\sigma/dQ^2$, $d\sigma/dx$, and $d^2\sigma/dxdQ^2$ measurements, and linear center was chosen for the $d\sigma/dy$ measurement except for the highest Q^2 and the highest x bins. The reference point for the highest Q^2 was taken so that the logarithmic distance to the previous reference point is equal to the one at other points. [1] The reference point for the highest x was chosen as 0.65, while the logarithmic center is 0.75. This is to reduce a systematic effect in the bin centering correction induced by PDF assumption, which will be described in more detail in the section 7.7.

The bin centering correction factor, $\mathcal{C}_{cnt}$, is defined as:

$$\mathcal{C}_{cnt} = \frac{\frac{d^2\sigma}{dxdQ^2}^{SM}_{BORN}|_{(x_0,Q^2{}_0)}}{\sigma^{SM}_{BORN}}, \tag{6.17}$$

for instance for the $d^2\sigma/dxdQ^2$ measurement. Here $\frac{d^2\sigma}{dxdQ^2}^{SM}_{BORN}|_{(x_0,Q^2{}_0)}$ is the SM Born level cross section at the bin center of $(x_0, Q^2{}_0)$. Thus, the differential cross

[1] The logarithmic distance between the lowest and the second lowest Q^2 points is a little bit wider.

section at the bin center is measured as:

$$\frac{d^2\sigma}{dxdQ^2}_{BORN}|_{(x_0,Q^2_0)} = \sigma_{BORN} \times \mathcal{C}_{cnt}, \quad (6.18)$$

$$= \frac{\sigma_{BORN}}{\sigma^{SM}_{BORN}} \times \frac{d^2\sigma}{dxdQ^2}^{SM}_{BORN}|_{(x_0,Q^2_0)}, \quad (6.19)$$

$$= \frac{\sigma_{RAD}}{\sigma^{SM}_{RAD}} \times \frac{d^2\sigma}{dxdQ^2}^{SM}_{BORN}|_{(x_0,Q^2_0)}, \quad (6.20)$$

$$= \frac{N_{CC}}{N^{MC}_{exp}} \times \frac{d^2\sigma}{dxdQ^2}^{SM}_{BORN}|_{(x_0,Q^2_0)}, \quad (6.21)$$

The Born cross sections of both the integrated and differential are calculated using the program LEPTO with the CTEQ 4D structure function.

Chapter 7

SYSTEMATIC ERRORS

7.1 Overview

We considered following systematic sources.

- uncertainty in the data:
  - absolute energy scale of the CAL.
  - trigger efficiency.
  - CTD vertex finding efficiency.
  - thresholds of cuts.
- uncertainty in the background evaluation:
  - photoproduction backgrounds.
- systematic bias from the method of cross section measurement:
  - choice of parton density function.
  - parton cascade modeling.

These items are discussed and evaluated in the following sections.

7.2 Energy scale of the calorimeter

One of the major systematic errors arises from the uncertainty of the absolute energy scale of the calorimeter. Error propagates to larger in the high Q^2 and high x kinematic regions, where the distribution is steeply falling off.

With a large amount of data collected in the previous years, we could perform in-situ calibration of the energy scale by studying the energy balance between the

electron and hadrons in the high Q^2 neutral current events [55]. It led to the current best knowledge of the energy scale to be within 2%.

We can in general estimate the systematic effect from this source changing the energy scale of our data by $\pm 2\%$ as:

$$\delta_{\pm} \equiv \frac{N_{\pm}^{data} - N_0^{data}}{N_0^{data}}. \tag{7.1}$$

N^{data} is the number of data events. The subscript $+(-)$ represents the trial to shift the energy scale by +(-)2%, while 0 denotes the nominal. In this paper, however, the uncertainty was estimated by changing the energy scale of the MC events since our current data statistics is not enough for the purpose. The systematic error from the energy scale uncertainty, $\pm\delta^{\text{e-scale}}(syst.)$, was evaluated as:

$$+\delta^{\text{e-scale}}(syst.) \equiv \max(\delta_{\pm}), \tag{7.2}$$
$$-\delta^{\text{e-scale}}(syst.) \equiv \min(\delta_{\pm}), \tag{7.3}$$

where

$$\delta_{\pm} \equiv \frac{N_{\pm}^{MC} - N_0^{MC}}{N_0^{MC}}. \tag{7.4}$$

N^{MC} indicates the number of expected MC events. Figure 7.1 shows the estimated systematic errors for the single differential measurements as a function of (a) Q^2, (b) x, and (c) y. The statistical errors are smaller than the size of the symbols. The errors are within 5% in majority of the kinematic space. It, however, grows rapidly as Q^2 or x grows beyond a few thousands of Q^2 or $x = 0.1$. Largest is in the highest Q^2 region up to about 40% and about 30% in the highest x region. While for the $d\sigma/dy$ measurement, the errors are well controlled up to about 10% at the highest y.

7.3 Efficiency of the trigger at first level

Resolutions of the quantities calculated at the FLT are limited since only a part of information is available within the short time interval. This results in a slow turn-on of the trigger efficiency at the FLT. Since $\not{P}_T{}^{FLT}$ is calculated with a vector sum, the resolution is worse. We checked a possible systematic effect, i.e. whether the MC simulates reasonably the trigger efficiency. [1]

Since the $\not{P}_T{}^{FLT}$ thresholds are different for samples with or without good_TRK^{FLT}, we evaluated the efficiency separately. Firstly, the efficiency of the slot_60 for events

[1] At the SLT and TLT, the quantity used in the trigger selection is calculated from the read out data, so, we can assume that the efficiencies for them are well understood.

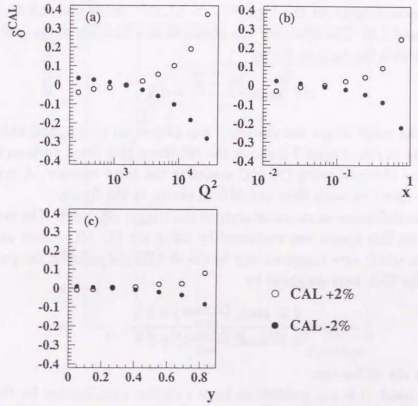

Figure 7.1: Systematic error on the single differential cross section measurements from the uncertainty of the absolute energy scale of the calorimeter. (a) for $d\sigma/dQ^2$, (b) for $d\sigma/dx$, and (c) for $d\sigma/dy$. The open(closed) circles are the case if the energy scale is higher(lower) by 2% than nominal.

with good_TRK^{FLT} was evaluated by using the data sample triggered by another logic as:

$$\mathcal{E}_{eff}^{\text{slot\_60}} = \frac{\text{No. of events which pass "TLT .and. SLT. and. FLT(slot\_42) .and. FLT(slot\_60)"}}{\text{No. of events which pass "TLT .and. SLT. and. FLT(slot\_42)"}}. \tag{7.5}$$

The sample used in the check was obtained by the preselection, the vertex cut, the tracking cuts, the NC rejection, and the halo-muon rejection.(see table 5.1) $\not{E}_T/E_T > 0.4$ was also imposed. The good_TRK^{FLT} condition inside the slot_42 allows us an examination on the logic "$\not{E}_T > 5\,\text{GeV}$" inside the slot_60 (see the equations 5.2 and 5.5). The efficiency was obtained as a function of the (offline) $\not{E}_T$, and was fitted with the turn-on curve,

$$0.5 \cdot \tanh(\frac{\not{E}_T - p}{q}) + 0.5. \tag{7.6}$$

The p refers the point where the efficiency has turned on to 0.5, and the q refers the slope of the curve. Figure 7.2 shows the efficiency and fitted turn-on curve as well as the ones obtained using CC MC events in the same manner. A systematic difference was found between data and MC as shown in the figure.

We took the difference as an uncertainty in the trigger efficiency. The systematic error arises from this source was evaluated by using the CC MC events as follows. The MC events which were triggered only by the slot_60 and satisfied the good_TRK condition at the FLT were weighted by

$$w = \frac{0.5 \cdot \tanh(\frac{\not{E}_T - p_{data}}{q_{data}}) + 0.5.}{0.5 \cdot \tanh(\frac{\not{E}_T - p_{MC}}{q_{MC}}) + 0.5.}, \tag{7.7}$$

where $\not{E}_T$ was the offline one.
On the other hand, it is not possible to have a similar examination for the events without good_TRK^{FLT} (see equation 5.3) since the total number of the event in the sample was not so large. Thus, the MC events, which were triggered only by the slot_60 and did not satisfy the good_TRK^{FLT}, were weighted by

$$w = \frac{0.5 \cdot \tanh(\frac{\not{E}_T - (p_{data}+3)}{q_{data}}) + 0.5.}{0.5 \cdot \tanh(\frac{\not{E}_T - (p_{MC}+3)}{q_{MC}}) + 0.5.}, \tag{7.8}$$

where p_{MC} and q_{MC} are the same values as used in equation 7.7. This means that we shifted the turn-on point(p) by 3 GeV for such events considering the difference of the thresholds(5 GeV and 8 GeV).

The acceptance correction factors were re-calculated using the weights. The difference was found to be 1.5% at largest at the highest-x and lowest-Q^2 bin in the double differential measurement. We neglected the systematic error from an uncertainty in the trigger efficiency.

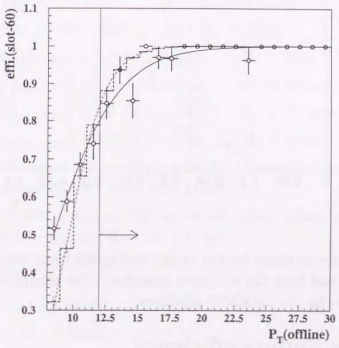

Figure 7.2: The turn-on curve for the trigger efficiency of the slot-60 at the FLT estimated both by the data and MC using independently triggered sample. The open circles and the solid line represent the efficiency and the turn-on curve determined using data, respectively. The dotted histogram and dotted line represent the efficiency and fitted curve determined using MC, respectively.

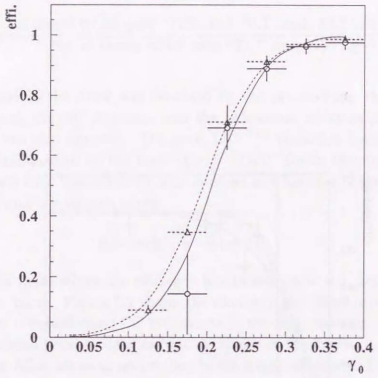

Figure 7.3: The turn-on curve for the vertex finding efficiency estimated from the data(open circles) and from the MC(open triangles). The solid(dashed) line is the fitted turn-on curve for the data(MC) efficiency.

7.4 Vertex finding efficiency

The vertex finding efficiency by the CTD was checked using the final candidates at the low γ region. The results are shown in figure 7.3. It is compared with the efficiency curve evaluated by using MCs. (same as shown in figure 5.2) Although a slight systematic difference was found between the two turn-on curves, the difference becomes smaller at higher γ_0, and the efficiency is sufficiently high at the boundary of $\gamma_0 = 0.4$ where we start to require CTD vertex. From this observation, we neglected the uncertainty from this source.

7.5 Threshold values of cuts

The systematic effect by setting a specific value for the threshold can be evaluated as a variation of correction factor moving the threshold to some amount in MC distribution. We shifted the threshold with typically 10% as follows.

High γ selection :

H1a $\not{E}_T > 12 + 1.2\,\mathrm{GeV}$

H1b $\not{E}_T > 12 - 1.2\,\mathrm{GeV}$

H2a Definition of the "good track": $P_T^{trk} > 0.2\,\mathrm{GeV}$, $\theta^{trk} > 15 + 5°$

H2b Definition of the "good track": $P_T^{trk} > 0.2 + 0.1\,\mathrm{GeV}$, $\theta^{trk} > 15°$

H2c Definition of the "good track": $P_T^{trk} > 0.2 + 0.1\,\mathrm{GeV}$, $\theta^{trk} > 15 + 5°$

H3a $\not{E}_T/E_T > 0.40 + 0.04 \qquad 20 < \not{E}_T < 30\,\mathrm{GeV}$

H3b $\not{E}_T/E_T > 0.40 - 0.04 \qquad 20 < \not{E}_T < 30\,\mathrm{GeV}$

H4a $|\Delta\phi_{CAL-CTD}| < 2.0 + 0.2$ radian $\qquad \not{E}_T > 20\,\mathrm{GeV}$

H4b $|\Delta\phi_{CAL-CTD}| < 2.0 - 0.2$ radian $\qquad \not{E}_T > 20\,\mathrm{GeV}$

H5a $|\Delta\phi_{CAL-CTD}| < 1.0 + 0.1$ radian $\qquad \not{E}_T < 20\,\mathrm{GeV}$

H5b $|\Delta\phi_{CAL-CTD}| < 1.0 - 0.1$ radian $\qquad \not{E}_T < 20\,\mathrm{GeV}$

H6a Definition of the low $\not{E}_T$ where the tighter photoproduction rejections should be applied: $\not{E}_T < 20 + 1\,\mathrm{GeV}$.

H6b Definition of the low $\not{E}_T$ where the tighter photoproduction rejections should be applied: $\not{E}_T < 20 - 1\,\mathrm{GeV}$.

Low γ selection :

L1a $\not{E}_T > 14 + 1.4\,\mathrm{GeV}$.

L1b $\not{E}_T > 14 - 1.4\,\mathrm{GeV}$.

L2a $\not{E}_T(-1ir) > 12 + 1.2\,\mathrm{GeV}$.

L2b $\not{E}_T(-1ir) > 12 - 1.2\,\mathrm{GeV}$.

The systematic error from this source was evaluated for instance for the "H1" trial as:

$$+\delta^{\mathrm{H1}}(syst.) \equiv \max(|\delta_{\mathrm{H1a}}|, |\delta_{\mathrm{H1b}}|), \tag{7.9}$$

$$-\delta^{\mathrm{H1}}(syst.) \equiv -\max(|\delta_{\mathrm{H1a}}|, |\delta_{\mathrm{H1b}}|), \tag{7.10}$$

where

$$\delta_{H1a(b)} \equiv \frac{C_{acc}^{H1a(b)} - C_{acc}^{0}}{C_{acc}^{0}}. \tag{7.11}$$

$C_{acc}^{H1a(b)}$ denotes the acceptance correction factor derived with the trial H1a(b). The subscript 0 denotes the nominal case.

Among these checks, trials on $\not{E}_T/E_T$(H3a,H3b), good track definitions(H2a,H2b,H2c), and $\Delta\phi_{CAL-CTD}$(H4a,H4b,H5a,H5b) in the high γ selection were found to give negligible, i.e. less than 1%, effects in all kinematic regions for both the single and the double differential measurements.

For the $d\sigma/dx$ measurement, about 1% effects were observed by the other shifts. At most 2% change was found by the shift of $\not{E}_T$ cut in the high γ selection(H1a,H1b).

For the $d\sigma/dy$ measurement, both the shift of the $\not{E}_T$ and $\not{E}_T(-1ir)$ cuts used in the low γ selection(L1a,L1b,L2a,L2b) induced 2-3% effect at the lowest y bin. The shift of the $\not{E}_T$ cut in the high γ selection(H1a,H1b) and of the low $\not{E}_T$ (H6a,H6b) gave 2-5% and 2% differences in higher y region($y \geq 0.5$), respectively.

The variation of the the $\not{E}_T$ cut for the high γ events(H1a,H1b) affected most for the measurements of $d\sigma/dQ^2$ and $d^2\sigma/dxdQ^2$. The effect was about 8% in the lowest Q^2 region in the single differential measurement and was about 10% at the lowest x bin in the lowest Q^2 region in the double differential measurement. It indicates that the $\not{E}_T$ cut is made at where the distribution is steeply changed. To make it sure that these numbers are not overestimated and are to be included in the systematic errors, whole analysis was repeated with the variated $\not{E}_T$ thresholds. The cross sections with these new thresholds showed similar systematic differences between the nominal cross section within statistical error; we decided to add the $\not{E}_T$ effects in the systematic errors as well.

7.6 Photoproduction backgrounds at lowest Q^2 region

The contamination of backgrounds was estimated to become about 10% in the lowest Q^2 region, while it is at 2-3% in other phase space. Dominant contribution in the region is from photoproduction events; the evaluation on the photoproduction backgrounds was checked using the measured $\not{E}_T/E_T$ distribution which was obtained by loosen the $\not{E}_T/E_T$ cut from the final selection.

Figure 7.4 (a) shows the obtained $\not{E}_T/E_T$ distribution in the lowest Q^2 region. The expected contributions both from the direct and resolved photoproduction processes are also plotted. Introducing two normalization factors f_{dir} and f_{res} each for the direct and resolved photoproduction MCs, the measured distribution was examined whether it is reasonably described as the sum of the charged current, photoproduction, and other background MC distributions or not. Chi-squared to be minimized was defined as follows:

$$\chi^2 \equiv \sum_{\text{bin}=i} \frac{(\text{DATA} - f_{dir}\cdot\text{DIR} - f_{res}\cdot\text{RES} - \text{DILEP} - \text{W} - f_{CC}\cdot CC)^2}{(\delta\text{DATA})^2 + f_{dir}{}^2(\delta\text{DIR})^2 + f_{res}{}^2(\delta\text{RES})^2 + (\delta\text{DILEP})^2 + (\delta\text{W})^2 + f_{CC}{}^2(\delta\text{CC})^2}, \tag{7.12}$$

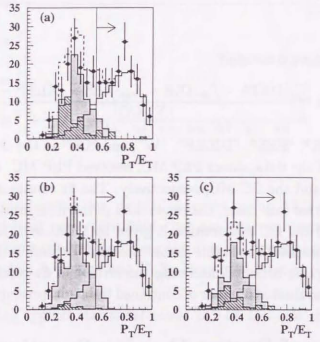

Figure 7.4: $\not{E}_T/E_T$ distributions. (a) the nominal, (b) fitted in full range, and (c) fitted in 0.3-0.8 range. The histogram with solid line is the CC MC. The histogram with shades is the resolved PhP, and the one hatched with declined lines is the direct PhP. Dashed line indicates the sum of all MCs.

Table 7.1: Results of the $\not\!\!E_T/E_T$ fit. Nominal denotes the one used in the nominal analysis. N_{PHP} in $\not\!\!E_T/E_T > 0.55$ denotes the number of PhP backgrounds into the signal region estimated with the fit result.

Fit condition	f_{dir}	f_{res}	N_{PHP} in $\not\!\!E_T/E_T > 0.55$
Nominal	1.	1.	10.7($\pm$3.26)
CDM, full range fit	0.15 ± 0.68	1.17 ± 0.32	8.35 ± 1.24
CDM, (0.3-0.8) fit	0.56 ± 0.49	0.80 ± 0.25	7.56 ± 1.11
MEPS, full range fit	0.12 ± 0.71	0.98 ± 0.31	7.00 ± 1.26
MEPS, (0.3-0.8) fit	0.46 ± 0.47	0.67 ± 0.25	6.27 ± 1.19

with the normalization constraint,

$$f_{CC} \equiv \frac{\sum_i (\mathrm{DATA} - f_{dir}\cdot\mathrm{DIR} - f_{res}\cdot\mathrm{RES} - \mathrm{DILEP} - \mathrm{W})}{\sum_i \mathrm{CC}}. \qquad (7.13)$$

The "DATA", "DIR", "RES", "DILEP", "W", and "CC" in the above equations are the distributions of the data, direct PhP MC, resolved PhP MC, the di-lepton MC, the single W MC, and the CC MC, respectively. The fit results are summarized in the table 7.1. We tried four cases, the range used in the fit is limited from 0.3 to 0.8 or not limited, and the CC distribution is given by CDM or MEPS samples. The number inside the bracket in the table in the "nominal" column is the statistical error of the photoproduction MCs. Considering the error and fit results, we put $\pm$40% uncertainty on the evaluated number of contained the photoproduction backgrounds.

7.7 Choice of Parton Density Function

We have assumed a specific parton density function, CTEQ 4D, in all procedures of the cross section measurement; i.e the acceptance correction, the radiative correction, and the bin centering correction. Possible systematic effect from this assumption was checked by applying other PDFs; we used the MRSA [64] and GRV 94 [65] parton densities for the purpose. [2]

First, systematic effect on the acceptance correction was investigated by re-weighting the MC events according to the cross section ratio between the CTEQ 4D and MRSA or GRV94 parton densities. Differences in the derived acceptance correction factors between using the nominal and re-weighted MCs were found to be small, less than 1%, in all kinematic regions for the single differential measurements, and typically less than 1% and at most 2% for the double differential measurement

[2] We will mention on the case when the PDF is "modified" to enlarge d-quark density at high x region later in the section 8.3.2.

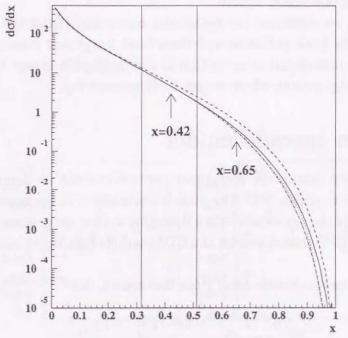

Figure 7.5: SM predictions for $d\sigma/dx$ obtained using CTEQ 4D(solid line), MRSA(dash-dotted line), and GRV 94(dotted line) parton densities. The dashed line indicates our simple trial on modifying the d-quark density according to the d/u correction suggested by A. Bodek and U. K. Yang.(See later in the section 8.3.2.)

regions. Considering typical statistical errors of our MC, we concluded that the effect is negligible.

The uncertainty in the radiative correction arising from the PDF assumption was evaluated from direct calculations using the program HECTOR [66]. Differences in the radiative correction factors by changing PDFs were found to be within 0.1%, which is an order of typical Monte Carlo integration error, in all kinematic regions. With these checks, we neglected an uncertainty from the PDF assumption in the both of radiative and Born level integrated cross sections.

The bin centering correction factor is the ratio between the differential and integrated cross sections. The correction factor depends on the shape of the differential cross section in a bin, and hence is sensitive to the PDF. A check was made with the two PDFs, and it was turned out that the effect is small(typically less than 0.5%) in all kinematic region except only for the highest x bin $0.562 < x < 1$ in the $d\sigma/dx$ measurement. Figure 7.5 shows the SM predictions for $d\sigma/dx$ obtained using CTEQ 4D, MESA, and GRV 94 parton densities. As shown in the figure, the cross section differs with different PDFs as x goes higher in the region $0.562 < x < 1.0$.

At $x = 0.65$ where the cross section measured in this analysis, MRSA and GRV 94 gave 2.5% different correction factors.

To summarize, we evaluated the systematic uncertainty from the PDF assumption as negligible in both radiative and Born level integrated cross sections. The uncertainty in the differential cross section is also negligible except for the highest x bin in $d\sigma/dx$ measurement where we set 2.5% uncertainty.

7.8 Parton cascade model

There might be a bias in the acceptance correction since we determine the correction factors with a specific MC. The main uncertainty is in the model on hadronic system. To estimate the systematic effect from this source, we prepared another MC sample with the MEPS model besides the CDM sample as already mentioned in the section 3.5.3.

We evaluated the systematic error from this source, $\pm\delta^{\text{QCD-cascade}}(syst.)$, as:

$$+\delta^{\text{QCD-cascade}}(syst.) \equiv |\delta|, \tag{7.14}$$

$$-\delta^{\text{QCD-cascade}}(syst.) \equiv -|\delta|, \tag{7.15}$$

where

$$\delta \equiv \frac{\mathcal{C}_{acc}^{MEPS} - \mathcal{C}_{acc}^{CDM}}{\mathcal{C}_{acc}^{CDM}}. \tag{7.16}$$

$\mathcal{C}_{acc}^{MEPS}$ and $\mathcal{C}_{acc}^{CDM}$ are the acceptance correction factors derived by using the MEPS and CDM samples, respectively. Figure 7.6 shows the systematic effect from this source in the single differential measurements with symbols of closed circles. It is shown that the effect is within a few percent in most of the phase space. However, the systematic error becomes about 5% in the lowest x and the highest y regions, and about 7.5% in the lowest and the highest Q^2 regions. The open circles in the figure indicate the systematic differences in the efficiency, and the open stars indicate the ones in the purity. As shown in the figure, the systematic differences in the correction factors are mainly due to differences in the efficiency.

7.9 Summary of systematic checks

The total systematic error, which would shift the cross section in positive(negative) direction, was evaluated as a quadratic sum of errors in positive(negative) direction

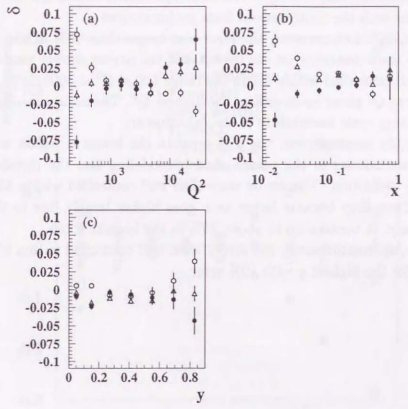

Figure 7.6: Systematic error on the single differential cross section measurements from the modeling of the parton cascading are indicated with symbols of closed circles. (a) for $d\sigma/dQ^2$, (b) for $d\sigma/dx$, (c) for $d\sigma/dy$. The open circles show systematic differences in efficiency, and the closed stars show the ones in purity.

from each sources.

$$+\delta(syst.) \equiv \sqrt{\sum_{i=\text{source}} (+\delta^i(syst.))^2}, \tag{7.17}$$

$$-\delta(syst.) \equiv -\sqrt{\sum_{i=\text{source}} (-\delta^i(syst.))^2}, \tag{7.18}$$

Figures 7.7, 7.8, and 7.9 summarize the systematic errors in $d\sigma/dQ^2$, $d\sigma/dx$, and $d\sigma/dy$ measurements, respectively. The total systematic errors are shown in the figures together with the contributions from major sources.

For the $d\sigma/dQ^2$ measurement, the error was larger than 10% at the lowest Q^2 mainly due to the dependence on the $\not{E}_T$ cut and the parton shower modeling. The errors were well controlled within 5% in the range $400 < Q^2 < 3000\,\text{GeV}^2$, and then became larger as Q^2 grew; up to 40% at the highest Q^2. The main contribution here is from the energy scale uncertainty of the calorimeter.

For the $d\sigma/dx$ measurement, the 8 % error in the lowest x region was mainly due to the uncertainties in the parton shower modeling and the threshold effect for the low $\not{E}_T$ definition. The errors were then well controlled within 5% up to x around 0.1. Then they became larger as x goes higher largely due to the energy scale uncertainty. It became up to about 25% in the highest x bin.

For the $d\sigma/dy$ measurement, the errors were well controlled within 5% in all y range except for the highest y with 10% error.

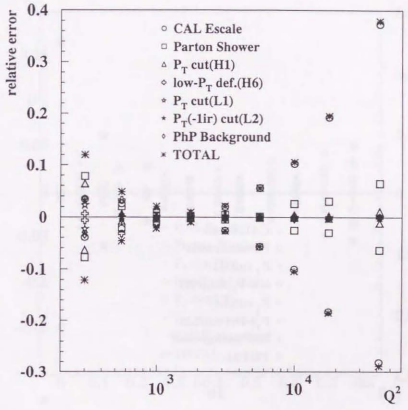

Figure 7.7: Summary of the systematic errors on the $d\sigma/dQ^2$ measurement.

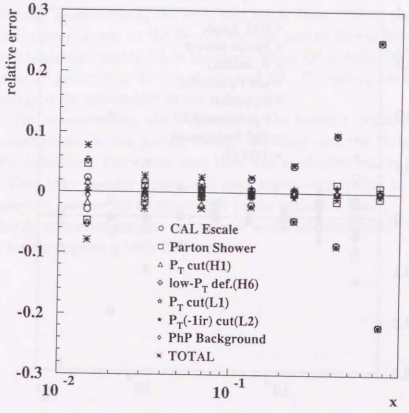

Figure 7.8: Summary of the systematic errors on the $d\sigma/dx$ measurement.

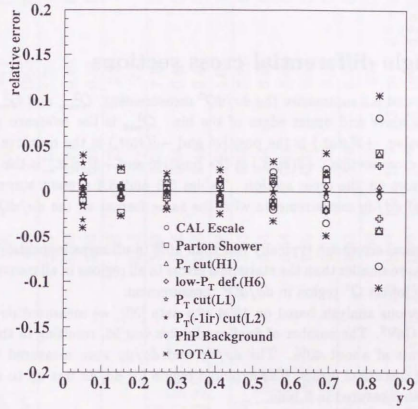

Figure 7.9: Summary of the systematic errors on the $d\sigma/dy$ measurement.

Chapter 8

RESULTS AND DISCUSSIONS

8.1 Single differential cross sections

Tables 8.1 and 8.2 summarize the $d\sigma/dQ^2$ measurement. Q^2_{min} and Q^2_{max} in the tables are the lower and upper edges of the bin. Q^2_{mid} is the reference point for the $d\sigma/dQ^2$ value. $+\delta(stat.)$ is the positive and $-\delta(stat.)$ is the negative statistic errors on the cross section. $+\delta(syst.)$ is the positive and $-\delta(syst.)$ is the negative systematic errors on the cross section. Tables 8.3 and 8.4 present summaries of the $d\sigma/dx$ and $d\sigma/dy$ measurements with the same format as the $d\sigma/dQ^2$ tables, respectively.

The statistical errors are typically less than 10% in all measurements. The systematic errors are smaller than the statistical errors in all regions in all measurements except for the lowest Q^2 region in $d\sigma/dQ^2$ measurement.

In our previous analysis based on 1994 e^+p data [30], we measured $d\sigma/dQ^2$ up to $Q^2 = 6500\,\mathrm{GeV}^2$. The number of final candidates was 56, resulting in the typical statistical errors of about 40%. The $d\sigma/dx$ and $d\sigma/dy$ were measured with the similar size of statistical errors. The explored region for $d\sigma/dx$ was up to $x = 0.25$. The $d\sigma/dy$ was measured in 5 bins.

Compared with this previous measurement, both the statistical and the systematic errors were reduced in all measurements in this analysis. In addition, this analysis has extended the explored kinematic region. The maximum Q^2 among the final candidates was greater than 40000 GeV^2 and $d\sigma/dQ^2$ was measured up to $Q^2 = 30000\,\mathrm{GeV}^2$. We have improved the efficiency to the low γ region, hence the the high x region by including events which have no vertex reconstruction by the tracking detectors. The $d\sigma/dx$ was measured in this analysis up to $x = 0.65$. The $d\sigma/dy$ was measured in 7 bins.

Table 8.1: Summary of the single differential cross section measurement as a function of Q^2(1).

Q^2_{min} [GeV^2]	200	400	711	1265	2249
Q^2_{max} [GeV^2]	400	711	1265	2249	4000
$\mathcal{C}_{acc}$	2.17	1.56	1.35	1.26	1.24
$\mathcal{E}$	0.30	0.40	0.49	0.54	0.56
$\mathcal{P}$	0.64	0.63	0.66	0.68	0.69
N_{obs}	138	173	248	204	174
N_{bg}	16.5	5.3	2.3	2.3	2.4
σ_{rad} [pb]	5.65	5.63	7.10	5.47	4.55
$+\delta\sigma_{rad}(stat.)$ [pb]	0.55	0.44	0.46	0.39	0.35
$-\delta\sigma_{rad}(stat.)$ [pb]	0.55	0.44	0.46	0.39	0.35
$\mathcal{C}_{rad}$	0.98	1.00	1.02	1.03	1.04
σ_{Born} [pb]	5.53	5.64	7.22	5.66	4.75
$+\delta\sigma_{Born}(stat.)$ [pb]	0.54	0.44	0.46	0.40	0.37
$-\delta\sigma_{Born}(stat.)$ [pb]	0.54	0.44	0.46	0.40	0.37
$+\delta\sigma_{Born}(syst.)$ [pb]	0.66	0.27	0.15	0.05	0.10
$-\delta\sigma_{Born}(syst.)$ [pb]	0.67	0.26	0.16	0.05	0.13
σ^{SM}_{Born} [pb]	5.53	5.76	6.34	5.97	4.53
Q^2_{mid} [GeV^2]	280	530	950	1700	3000
$d\sigma_{Born}/dQ^2$ [pb/GeV^2]	2.9×10^{-2}	1.9×10^{-2}	1.3×10^{-2}	5.9×10^{-3}	2.8×10^{-3}
$+\delta d\sigma_{Born}/dQ^2(stat.)$ [pb/GeV^2]	2.8×10^{-3}	1.5×10^{-3}	8.6×10^{-4}	4.2×10^{-4}	2.1×10^{-4}
$-\delta d\sigma_{Born}/dQ^2(stat.)$ [pb/GeV^2]	2.8×10^{-3}	1.5×10^{-3}	8.6×10^{-4}	4.2×10^{-4}	2.1×10^{-4}
$+\delta d\sigma_{Born}/dQ^2(syst.)$ [pb/GeV^2]	3.4×10^{-3}	9.0×10^{-4}	2.8×10^{-4}	5.6×10^{-5}	5.9×10^{-5}
$-\delta d\sigma_{Born}/dQ^2(syst.)$ [pb/GeV^2]	3.5×10^{-3}	8.7×10^{-4}	2.9×10^{-4}	5.6×10^{-5}	7.5×10^{-5}

Table 8.2: Summary of the single differential cross section measurement as a function of Q^2(II).

Q^2_{min} [GeV^2]	4000	7113	12649	22494
Q^2_{max} [GeV^2]	7113	12649	22494	60000
$\mathcal{C}_{acc}$	1.22	1.17	1.08	0.75
$\mathcal{E}$	0.56	0.55	0.50	0.48
$\mathcal{P}$	0.69	0.64	0.54	0.36
N_{obs}	91	46	13	1
N_{bg}	0.64	0.72	0.11	0.014
σ_{rad} [pb]	2.37	1.14	0.30	0.016
$+\delta\sigma_{rad}(stat.)$ [pb]	0.25	0.17	0.11	0.037
$-\delta\sigma_{rad}(stat.)$ [pb]	0.25	0.17	0.08	0.013
$\mathcal{C}_{rad}$	1.08	1.09	1.11	1.11
σ_{Born} [pb]	2.55	1.24	0.33	0.018
$+\delta\sigma_{Born}(stat.)$ [pb]	0.27	0.19	0.12	0.041
$-\delta\sigma_{Born}(stat.)$ [pb]	0.27	0.19	0.09	0.015
$+\delta\sigma_{Born}(syst.)$ [pb]	0.14	0.13	0.06	0.007
$-\delta\sigma_{Born}(syst.)$ [pb]	0.15	0.13	0.06	0.005
σ^{SM}_{Born} [pb]	2.56	0.96	0.20	0.017
Q^2_{mid} [GeV^2]	5300	9500	17000	30000
$d\sigma_{Born}/dQ^2$ [pb/GeV^{-2}]	8.4×10^{-4}	2.2×10^{-4}	2.9×10^{-5}	7.0×10^{-7}
$+\delta d\sigma_{Born}/dQ^2$(stat.) [pb/GeV^{-2}]	8.8×10^{-5}	3.3×10^{-5}	1.1×10^{-5}	1.6×10^{-6}
$-\delta d\sigma_{Born}/dQ^2$(stat.) [pb/GeV^{-2}]	8.8×10^{-5}	3.3×10^{-5}	8.0×10^{-6}	6.0×10^{-7}
$+\delta d\sigma_{Born}/dQ^2$(syst.) [pb/GeV^{-2}]	4.7×10^{-5}	2.3×10^{-5}	5.6×10^{-6}	3.0×10^{-7}
$-\delta d\sigma_{Born}/dQ^2$(syst.) [pb/GeV^{-2}]	4.8×10^{-5}	2.3×10^{-5}	5.4×10^{-6}	2.0×10^{-7}

Table 8.3: Summary of the single differential cross section measurement as a function of x.

x_{min}	0.010	0.021	0.046	0.100	0.178	0.316	0.562
x_{max}	0.021	0.046	0.100	0.178	0.316	0.562	1.000
$\mathcal{C}_{acc}$	1.77	1.26	1.18	1.22	1.38	1.78	2.87
$\mathcal{E}$	0.37	0.59	0.69	0.67	0.62	0.49	0.27
$\mathcal{P}$	0.66	0.74	0.81	0.82	0.85	0.88	0.78
N_{obs}	132	249	308	201	124	45	4
N_{bg}	4.0	7.4	10.0	2.9	0.6	0.06	0.00
σ_{rad} [pb]	4.87	6.53	7.53	5.20	3.64	1.72	0.25
$+\delta\sigma_{rad}(stat.)$ [pb]	0.44	0.43	0.45	0.37	0.33	0.26	0.19
$-\delta\sigma_{rad}(stat.)$ [pb]	0.44	0.43	0.45	0.37	0.33	0.26	0.12
$\mathcal{C}_{rad}$	1.01	1.01	1.02	1.03	1.06	1.09	1.13
σ_{Born} [pb]	4.94	6.58	7.65	5.35	3.87	1.87	0.28
$+\delta\sigma_{Born}(stat.)$ [pb]	0.45	0.43	0.45	0.38	0.35	0.28	0.22
$-\delta\sigma_{Born}(stat.)$ [pb]	0.45	0.43	0.45	0.38	0.35	0.28	0.13
$+\delta\sigma_{Born}(syst.)$ [pb]	0.38	0.19	0.20	0.14	0.18	0.18	0.07
$-\delta\sigma_{Born}(syst.)$ [pb]	0.39	0.18	0.21	0.13	0.18	0.16	0.06
σ^{SM}_{Born} [pb]	4.59	6.80	7.81	5.19	3.33	1.15	0.08
x_{mid}	0.015	0.032	0.068	0.130	0.240	0.420	0.650
$d\sigma_{Born}/dx$ [pb]	4.4×10^2	2.7×10^2	1.5×10^2	7.3×10^1	2.8×10^1	7.4×10^0	1.2×10^0
$+\delta d\sigma_{Born}/dx$(stat.) [pb]	3.9×10^1	1.8×10^1	8.8×10^0	5.2×10^0	2.5×10^0	1.1×10^0	9.8×10^{-1}
$-\delta d\sigma_{Born}/dx$(stat.) [pb]	3.9×10^1	1.8×10^1	8.8×10^0	5.2×10^0	2.5×10^0	1.1×10^0	6.0×10^{-1}
$+\delta d\sigma_{Born}/dx$(syst.) [pb]	3.4×10^1	7.7×10^0	3.9×10^0	1.9×10^0	1.3×10^0	7.2×10^{-1}	3.1×10^{-1}
$-\delta d\sigma_{Born}/dx$(syst.) [pb]	3.4×10^1	7.5×10^0	4.0×10^0	1.7×10^0	1.3×10^0	6.5×10^{-1}	2.8×10^{-1}

Table 8.4: Summary of the single differential cross section measurement as a function of y.

y_{min}	0.00	0.10	0.20	0.34	0.48	0.62	0.76
y_{max}	0.10	0.20	0.34	0.48	0.62	0.76	0.90
$\mathcal{C}_{acc}$	1.56	1.17	1.19	1.29	1.41	1.67	2.29
$\mathcal{E}$	0.57	0.71	0.67	0.58	0.48	0.38	0.25
$\mathcal{P}$	0.89	0.83	0.80	0.74	0.68	0.63	0.58
N_{obs}	192	246	242	180	123	64	41
N_{bg}	7.3	5.2	2.6	5.0	3.8	2.1	1.1
σ_{rad} [pb]	6.16	6.05	6.12	4.83	3.62	2.22	1.96
$+\delta\sigma_{rad}(stat.)$ [pb]	0.46	0.40	0.40	0.37	0.34	0.29	0.32
$-\delta\sigma_{rad}(stat.)$ [pb]	0.46	0.40	0.40	0.37	0.34	0.29	0.32
$\mathcal{C}_{rad}$	1.02	1.00	1.01	1.02	1.04	1.04	1.08
σ_{Born} [pb]	6.26	6.04	6.19	4.91	3.76	2.31	2.11
$+\delta\sigma_{Born}(stat.)$ [pb]	0.47	0.40	0.40	0.38	0.35	0.30	0.34
$-\delta\sigma_{Born}(stat.)$ [pb]	0.47	0.40	0.40	0.38	0.35	0.30	0.34
$+\delta\sigma_{Born}(syst.)$ [pb]	0.25	0.16	0.12	0.12	0.12	0.10	0.22
$-\delta\sigma_{Born}(syst.)$ [pb]	0.25	0.16	0.12	0.12	0.12	0.11	0.22
σ^{SM}_{Born} [pb]	5.86	5.82	6.06	4.41	3.40	2.69	2.27
y_{mid}	0.05	0.15	0.27	0.41	0.55	0.69	0.83
$d\sigma_{Born}/dy$ [pb]	73.9	60.7	44.2	34.9	26.3	16.2	14.9
$+\delta d\sigma_{Born}/dy(stat.)$ [pb]	5.6	4.0	2.9	2.7	2.5	2.1	2.4
$-\delta d\sigma_{Born}/dy(stat.)$ [pb]	5.6	4.0	2.9	2.7	2.5	2.1	2.4
$+\delta d\sigma_{Born}/dy(syst.)$ [pb]	2.9	1.6	0.9	0.8	0.9	0.7	1.6
$-\delta d\sigma_{Born}/dy(syst.)$ [pb]	3.0	1.6	0.9	0.8	0.8	0.8	1.6

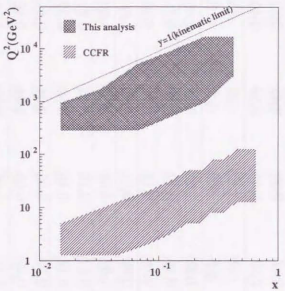

Figure 8.1: Kinematic regions surveyed by this measurement(e^+p) and by the CCFR experiment(νN) [15].

8.2 Double differential cross sections

We present the reduced double differential cross section, $\overline{\sigma}$, which is defined as:

$$\overline{\sigma} \equiv x \frac{d^2\sigma}{dxdQ^2} \frac{2\pi}{{G_F}^2} \left(\frac{{M_W}^2}{{M_W}^2 + Q^2} \right)^{-2}. \tag{8.1}$$

In this conversion, the Particle Data Group's [67] values were used for M_W(80.33 GeV) and $G_F(1.16639 \times 10^{-5}\text{GeV}^{-2})$.

In the QPM, the reduced cross section is expressed in terms of the parton densities as:

$$\overline{\sigma} = x \sum_{i=1,2} [\overline{u_i}(x, Q^2) + (1-y)^2 d_i(x, Q^2)]. \tag{8.2}$$

Tables 8.5, 8.6, 8.7, and 8.8 present a summary of the double differential measurement. The statistical errors are typically 15%. The systematic errors are smaller than the statistical errors in almost all kinematic region.

This is the first measurement of the double differential cross sections for e^+p charged current interaction. In addition, this kinematic region($Q^2 > 200\,\text{GeV}^2$) has never been explored either by the fixed-target neutrino-beam experiments. Figure 8.1 presents the kinematic regions surveyed by this measurement and by the CCFR [15], which is the experiment for νN scattering with the highest center of mass energy.

Table 8.5: Summary of the double differential cross section measurement(I).

x_{min}	0.010	0.021	0.046	0.010	0.021	0.046	0.100	0.010
x_{max}	0.021	0.046	0.100	0.021	0.046	0.100	0.178	0.021
Q^2_{min} [GeV^2]	200	200	200	400	400	400	400	711
Q^2_{max} [GeV^2]	400	400	400	711	711	711	711	1265
$\mathcal{C}_{acc}$	1.56	1.24	1.41	1.58	1.14	1.14	1.30	1.98
$\mathcal{E}$	0.33	0.44	0.41	0.29	0.47	0.52	0.45	0.20
$\mathcal{P}$	0.51	0.54	0.59	0.46	0.53	0.60	0.58	0.40
N_{obs}	47	42	27	43	51	45	20	35
N_{bg}	2.0	4.7	5.9	1.6	0.8	1.0	0.5	0.3
σ_{rad} [pb]	1.51	0.99	0.64	1.40	1.23	1.08	0.54	1.48
$+\delta\sigma_{rad}(stat.)$ [pb]	0.23	0.17	0.16	0.22	0.18	0.17	0.16	0.25
$-\delta\sigma_{rad}(stat.)$ [pb]	0.23	0.17	0.16	0.22	0.18	0.17	0.12	0.25
$\mathcal{C}_{rad}$	0.95	0.98	0.99	1.01	0.99	0.97	0.99	1.06
σ_{Born} [pb]	1.43	0.97	0.64	1.41	1.22	1.04	0.54	1.56
$+\delta\sigma_{Born}(stat.)$ [pb]	0.22	0.17	0.16	0.22	0.17	0.16	0.15	0.27
$-\delta\sigma_{Born}(stat.)$ [pb]	0.22	0.17	0.16	0.22	0.17	0.16	0.12	0.27
$+\delta\sigma_{Born}(syst.)$ [pb]	0.14	0.10	0.23	0.13	0.19	0.05	0.04	0.16
$-\delta\sigma_{Born}(syst.)$ [pb]	0.14	0.10	0.23	0.12	0.19	0.05	0.04	0.16
σ^{SM}_{Born} [pb]	1.19	1.01	0.77	1.44	1.33	1.06	0.55	1.54
x_{mid}	0.015	0.032	0.068	0.015	0.032	0.068	0.130	0.015
Q^2_{mid} [GeV^2]	280	280	280	530	530	530	530	950
$\overline{\sigma}$	1.2×10^{0}	8.2×10^{-1}	5.4×10^{-1}	8.4×10^{-1}	7.2×10^{-1}	6.2×10^{-1}	4.3×10^{-1}	6.7×10^{-1}
$+\delta\overline{\sigma}(stat.)$	1.9×10^{-1}	1.4×10^{-1}	1.3×10^{-1}	1.3×10^{-1}	1.0×10^{-1}	9.4×10^{-2}	1.2×10^{-1}	1.1×10^{-1}
$-\delta\overline{\sigma}(stat.)$	1.9×10^{-1}	1.4×10^{-1}	1.3×10^{-1}	1.3×10^{-1}	1.0×10^{-1}	9.4×10^{-2}	9.8×10^{-2}	1.1×10^{-1}
$+\delta\overline{\sigma}(syst.)$	1.2×10^{-1}	8.1×10^{-2}	2.0×10^{-1}	7.8×10^{-2}	1.1×10^{-1}	2.9×10^{-2}	3.2×10^{-2}	6.8×10^{-2}
$-\delta\overline{\sigma}(syst.)$	1.2×10^{-1}	8.4×10^{-2}	2.0×10^{-1}	7.1×10^{-2}	1.1×10^{-1}	3.2×10^{-2}	3.2×10^{-2}	7.0×10^{-2}

Table 8.6: Summary of the double differential cross section measurement(II).

x_{min}	0.021	0.046	0.100	0.178	0.021	0.046	0.100	0.178
x_{max}	0.046	0.100	0.178	0.316	0.046	0.100	0.178	0.316
Q^2_{min} [GeV^2]	711	711	711	711	1265	1265	1265	1265
Q^2_{max} [GeV^2]	1265	1265	1265	1265	2249	2249	2249	2249
$\mathcal{C}_{acc}$	1.14	1.12	1.19	1.49	1.32	1.09	1.14	1.21
$\mathcal{E}$	0.47	0.56	0.54	0.43	0.38	0.56	0.59	0.56
$\mathcal{P}$	0.54	0.63	0.64	0.64	0.50	0.61	0.67	0.68
N_{obs}	88	69	42	14	58	64	41	28
N_{bg}	0.4	0.5	0.2	0.0	0.9	1.1	0.3	0.3
σ_{rad} [pb]	2.13	1.65	1.06	0.45	1.61	1.47	0.99	0.72
$+\delta\sigma_{rad}(stat.)$ [pb]	0.23	0.20	0.17	0.15	0.22	0.19	0.16	0.14
$-\delta\sigma_{rad}(stat.)$ [pb]	0.23	0.20	0.17	0.12	0.22	0.19	0.16	0.14
$\mathcal{C}_{rad}$	1.00	0.98	1.03	1.05	1.02	1.03	1.03	1.04
σ_{Born} [pb]	2.12	1.61	1.09	0.47	1.65	1.52	1.02	0.75
$+\delta\sigma_{Born}(stat.)$ [pb]	0.23	0.20	0.17	0.16	0.22	0.19	0.16	0.14
$-\delta\sigma_{Born}(stat.)$ [pb]	0.23	0.20	0.17	0.12	0.22	0.19	0.16	0.14
$+\delta\sigma_{Born}(syst.)$ [pb]	0.12	0.04	0.05	0.02	0.11	0.09	0.04	0.07
$-\delta\sigma_{Born}(syst.)$ [pb]	0.13	0.04	0.05	0.02	0.11	0.09	0.04	0.07
σ^{SM}_{Born} [pb]	1.76	1.50	0.81	0.45	1.89	1.82	1.05	0.60
x_{mid}	0.032	0.068	0.130	0.240	0.032	0.068	0.130	0.240
Q^2_{mid} [GeV^2]	950	950	950	950	1700	1700	1700	1700
$\overline{\sigma}$	8.0×10^{-1}	6.0×10^{-1}	5.5×10^{-1}	2.3×10^{-1}	4.3×10^{-1}	3.9×10^{-1}	3.5×10^{-1}	2.5×10^{-1}
$+\delta\overline{\sigma}(stat.)$	8.6×10^{-2}	7.4×10^{-2}	8.6×10^{-2}	7.9×10^{-2}	5.7×10^{-2}	5.0×10^{-2}	5.6×10^{-2}	4.8×10^{-2}
$-\delta\overline{\sigma}(stat.)$	8.6×10^{-2}	7.4×10^{-2}	8.6×10^{-2}	6.0×10^{-2}	5.7×10^{-2}	5.0×10^{-2}	5.6×10^{-2}	4.8×10^{-2}
$+\delta\overline{\sigma}(syst.)$	4.6×10^{-2}	1.6×10^{-2}	2.5×10^{-2}	7.8×10^{-3}	3.0×10^{-2}	2.3×10^{-2}	1.3×10^{-2}	2.5×10^{-2}
$-\delta\overline{\sigma}(syst.)$	4.8×10^{-2}	1.6×10^{-2}	2.5×10^{-2}	7.9×10^{-3}	2.9×10^{-2}	2.3×10^{-2}	1.3×10^{-2}	2.5×10^{-2}

Table 8.7: Summary of the double differential cross section measurement(III).

x_{min}	0.046	0.100	0.178	0.316	0.046	0.100	0.178	0.316
x_{max}	0.100	0.178	0.316	0.562	0.100	0.178	0.316	0.562
Q^2_{min} [GeV^2]	2249	2249	2249	2249	4000	4000	4000	4000
Q^2_{max} [GeV^2]	4000	4000	4000	4000	7113	7113	7113	7113
$\mathcal{C}_{acc}$	1.13	1.12	1.16	1.33	1.45	1.10	1.14	1.18
$\mathcal{E}$	0.52	0.60	0.61	0.54	0.29	0.55	0.63	0.62
$\mathcal{P}$	0.58	0.67	0.71	0.72	0.43	0.61	0.71	0.73
N_{obs}	80	42	27	15	22	36	25	8
N_{bg}	1.1	0.2	0.1	0.0	0.4	0.2	0.1	0.0
σ_{rad} [pb]	1.92	1.01	0.67	0.43	0.67	0.85	0.61	0.20
$+\delta\sigma_{rad}(stat.)$ [pb]	0.22	0.16	0.13	0.14	0.18	0.14	0.15	0.10
$-\delta\sigma_{rad}(stat.)$ [pb]	0.22	0.16	0.13	0.11	0.15	0.14	0.12	0.07
$\mathcal{C}_{rad}$	1.04	1.03	1.07	1.07	1.09	1.06	1.08	1.09
σ_{Born} [pb]	1.99	1.04	0.72	0.46	0.73	0.90	0.66	0.22
$+\delta\sigma_{Born}(stat.)$ [pb]	0.23	0.16	0.14	0.15	0.20	0.15	0.16	0.11
$-\delta\sigma_{Born}(stat.)$ [pb]	0.23	0.16	0.14	0.12	0.16	0.15	0.13	0.08
$+\delta\sigma_{Born}(syst.)$ [pb]	0.04	0.07	0.02	0.04	0.05	0.11	0.05	0.02
$-\delta\sigma_{Born}(syst.)$ [pb]	0.08	0.07	0.03	0.04	0.05	0.11	0.04	0.02
σ^{SM}_{Born} [pb]	1.72	1.11	0.68	0.22	0.88	0.86	0.59	0.21
x_{mid}	0.068	0.130	0.240	0.420	0.068	0.130	0.240	0.420
Q^2_{mid} [GeV^2]	3000	3000	3000	3000	5300	5300	5300	5300
$\overline{\sigma}$	3.9×10^{-1}	2.7×10^{-1}	1.8×10^{-1}	1.1×10^{-1}	1.8×10^{-1}	2.1×10^{-1}	1.5×10^{-1}	4.8×10^{-2}
$+\delta\overline{\sigma}(stat.)$	4.4×10^{-2}	4.3×10^{-2}	3.5×10^{-2}	3.7×10^{-2}	4.7×10^{-2}	3.5×10^{-2}	3.6×10^{-2}	2.4×10^{-2}
$-\delta\overline{\sigma}(stat.)$	4.4×10^{-2}	4.3×10^{-2}	3.5×10^{-2}	2.9×10^{-2}	3.8×10^{-2}	3.5×10^{-2}	3.0×10^{-2}	1.7×10^{-2}
$+\delta\overline{\sigma}(syst.)$	7.0×10^{-3}	2.0×10^{-2}	4.6×10^{-3}	9.8×10^{-3}	1.1×10^{-2}	2.5×10^{-2}	1.0×10^{-2}	3.9×10^{-3}
$-\delta\overline{\sigma}(syst.)$	1.6×10^{-2}	1.9×10^{-2}	7.8×10^{-3}	9.5×10^{-3}	1.2×10^{-2}	2.4×10^{-2}	8.1×10^{-3}	3.7×10^{-3}

Table 8.8: Summary of the double differential cross section measurement(IV).

x_{min}	0.100	0.178	0.316	0.178	0.316
x_{max}	0.178	0.316	0.562	0.316	0.562
Q^2_{min} [GeV^2]	7113	7113	7113	12649	12649
Q^2_{max} [GeV^2]	12649	12649	12649	22494	22494
$\mathcal{C}_{acc}$	1.20	1.06	1.12	1.03	0.99
$\mathcal{E}$	0.36	0.60	0.64	0.39	0.63
$\mathcal{P}$	0.44	0.64	0.72	0.40	0.63
N_{obs}	15	19	9	5	7
N_{bg}	0.6	0.1	0.0	0.1	0.0
σ_{rad} [pb]	0.37	0.43	0.22	0.11	0.15
$+\delta\sigma_{rad}(stat.)$ [pb]	0.13	0.12	0.10	0.07	0.08
$-\delta\sigma_{rad}(stat.)$ [pb]	0.10	0.10	0.07	0.05	0.05
$\mathcal{C}_{rad}$	1.08	1.09	1.09	1.11	1.12
σ_{Born} [pb]	0.40	0.47	0.23	0.12	0.17
$+\delta\sigma_{Born}(stat.)$ [pb]	0.14	0.13	0.11	0.08	0.09
$-\delta\sigma_{Born}(stat.)$ [pb]	0.11	0.11	0.08	0.05	0.06
$+\delta\sigma_{Born}(syst.)$ [pb]	0.07	0.05	0.03	0.03	0.03
$-\delta\sigma_{Born}(syst.)$ [pb]	0.08	0.05	0.02	0.02	0.03
σ^{SM}_{Born} [pb]	0.39	0.35	0.15	0.11	0.06
x_{mid}	0.130	0.240	0.420	0.240	0.420
Q^2_{mid} [GeV^2]	9500	9500	9500	17000	17000
$\overline{\sigma}$	1.0×10^{-1}	1.1×10^{-1}	5.3×10^{-2}	3.4×10^{-2}	4.6×10^{-2}
$+\delta\overline{\sigma}(stat.)$	3.6×10^{-2}	3.1×10^{-2}	2.4×10^{-2}	2.3×10^{-2}	2.5×10^{-2}
$-\delta\overline{\sigma}(stat.)$	2.8×10^{-2}	2.5×10^{-2}	1.7×10^{-2}	1.5×10^{-2}	1.7×10^{-2}
$+\delta\overline{\sigma}(syst.)$	1.8×10^{-2}	1.2×10^{-2}	6.2×10^{-3}	8.5×10^{-3}	9.2×10^{-3}
$-\delta\overline{\sigma}(syst.)$	2.0×10^{-2}	1.2×10^{-2}	5.5×10^{-3}	6.9×10^{-3}	7.5×10^{-3}

8.3 Comparison with the Standard Model predictions

8.3.1 Single differential cross sections

The measured cross sections were compared with the Standard Model predictions obtained using the CTEQ4D, MRSA, and GRV94 parton densities. These PDFs were evolved according to the Next-to-Leading-Order(NLO) QCD DGLAP equation. Since the parton densities are obtained by QCD fits to experimental data, they have uncertainties due to the errors of such experiments. To estimate this uncertainty, we performed a NLO QCD fit [68] to ZEUS and fixed target F_2 structure function data measured in lower Q^2 region. The uncertainty was estimated as the error propagated via the NLO QCD DGLAP evolution.

Figure 8.2 presents $d\sigma/dQ^2$ compared with the SM predictions. In the upper plot(a), the cross sections are superimposed on the SM prediction with the CTEQ4D parton density. In the lower plot(b), the cross sections are presented as the ratios to the SM prediction with the CTEQ4D parton density. The SM predictions with other PDFs are also presented as the ratios in the lower plot. The shaded area(labeled "PDF band") in the lower plot represents the PDF associated uncertainty estimated from our QCD fit. Comparisons for the $d\sigma/dx$ and $d\sigma/dy$ are shown in Figures 8.3 and 8.4, respectively.

The $d\sigma/dQ^2$ was consistent with the SM predictions. The $d\sigma/dx$ showed a good agreement with the SM predictions up to x around 0.1, however, showed an excess in the higher x region than 0.1. The $d\sigma/dy$ agreed well with the SM predictions in all kinematic region of y.

8.3.2 The d-quark density

The charged current e^+p cross section is dominated by the d-quark contribution at high x. The observed excess in $d\sigma/dx$ at high x suggests that the d-quark density in the current PDFs may not be correct.

The main experimental inputs for the PDF fits at high x are provided by the low energy fixed target experiments. Tight constraint on the u-quark density is given by the precisely measured proton structure function(F_2^p). However, the d-quark density cannot be tightly constrained by F_2^p. It is mainly determined from the neutron structure function(F_2^n) extracted from the deuteron structure function(F_2^d). In addition, extra errors arise due to this extraction since there is a theoretical uncertainty in deuteron models. Hence, the d-quark density at high x is not well constrained. This can be seen in Figure 8.3 as the PDF band becomes large at high x. Our cross sections will provide a good constraint on the d-quark density for the PDF fits by the theory groups.

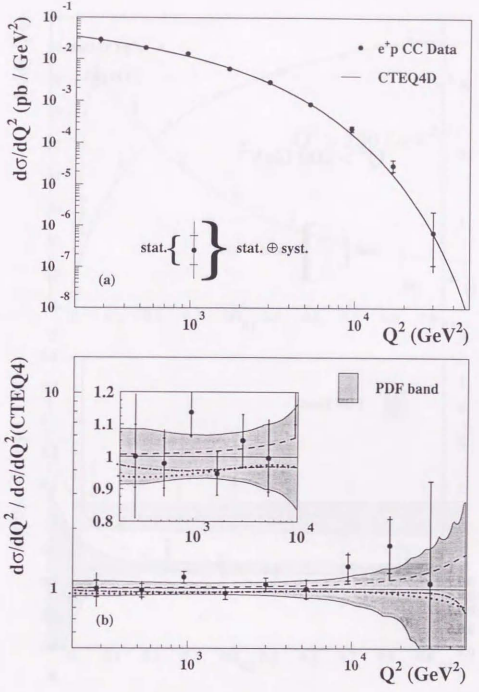

Figure 8.2: $d\sigma/dQ^2$ measured in the range of $200 < Q^2 < 60000$ GeV^2. The upper plot (a) shows the measured cross sections as closed circles and the SM prediction with the CTEQ4D PDF as curve. The lower plot (b) shows the cross section ratios to the SM prediction with CTEQ4D PDF. The dotted(dash-dotted) line represents the SM prediction with MRSA(GRV94) PDF. The dashed line represents the SM prediction with the d/u-corrected PDF.(see section 8.3.2.) The shaded area(labeled "PDF band") represents the uncertainty associated with the parton density.(see text)

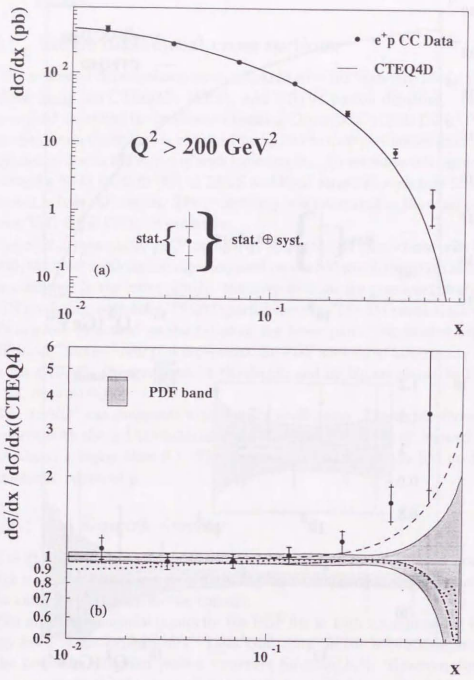

Figure 8.3: $d\sigma/dx$ measured in the range of $10^{-2} < x < 1$. The upper plot (a) shows the measured cross sections as closed circles and the SM prediction with the CTEQ4D PDF as curve. The lower plot (b) shows the cross section ratios to the SM prediction with CTEQ4D PDF. The dotted(dash-dotted) line represents the SM prediction with MRSA(GRV94) PDF. The dashed line represents the SM prediction with the d/u-corrected PDF.(see section 8.3.2.) The shaded area(labeled "PDF band") represents the uncertainty associated with the parton density.(see text)

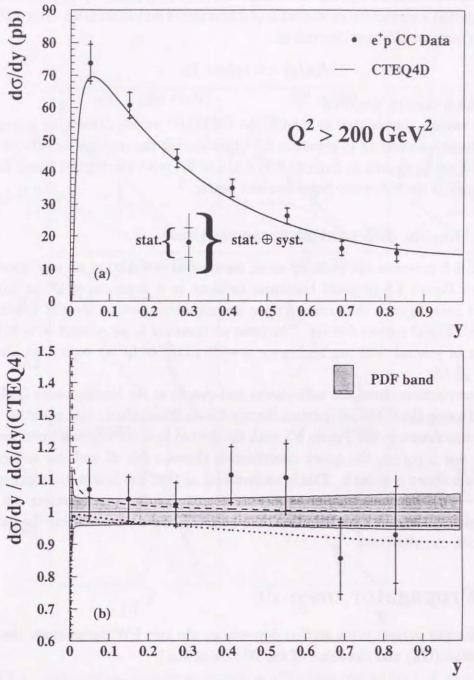

Figure 8.4: $d\sigma/dy$ measured in the range of $0 < y < 0.9$. The upper plot (a) shows the measured cross sections as closed circles and the SM prediction with the CTEQ4D PDF as curve. The lower plot (b) shows the cross section ratios to the SM prediction with CTEQ4D PDF. The dotted(dash-dotted) line represents the SM prediction with MRSA(GRV94) PDF. The dashed line represents the SM prediction with the d/u-corrected PDF.(see section 8.3.2.) The shaded area(labeled "PDF band") represents the uncertainty associated with the parton density.(see text)

Recently, there are re-analyses of NMC $F_2{}^d$ data correcting for the nuclear binding effect in the deuteron [69, 70]. This effect has been neglected in previous analyses. They suggested a correction on the ratio of d to u quark densities(d/u). An empirical correction term on d/u was derived as:

$$\delta(d/u) = 0.1x(x+1), \tag{8.3}$$

while u-quark density was fixed.

We've made a simple trial to modify the CTEQ4D parton density by increasing d-quark density according to equation 8.3 while leaving the u-quark density as it is. The results are presented in Figures 8.2, 8.3, and 8.4 with the dashed lines. In the $d\sigma/dx$ figure, it describes our cross sections better. [1]

8.3.3 Double differential cross sections

Figure 8.5 presents the reduced cross sections as a function of x at fixed Q^2 points and Figure 8.6 presents the cross sections as a function of Q^2 at fixed x points. In both figures, the cross sections are superimposed on the SM prediction with the CTEQ4D parton density. The cross sections are in agreement with the SM prediction in general, but are higher for a wide range of Q^2 at high x as already noted for $d\sigma/dx$.

The contributions from the anti-quarks and quarks at the leading order QCD are calculated using the CTEQ4L parton density for an illustration. (see equation 8.2.) They are also drawn in the Figure 8.5 with the dotted and dash-dotted lines, respectively. In low x region, the quark contribution shows a fall off and the anti-quark contribution shows a growth. This is understood as that the kinematic suppression factor $(1-y)^2$ becomes smaller as x decreases at fixed Q^2. (see equation 2.6.) In high x region, the quark contribution dominates. The data are well described as the sum of both contributions.

8.4 Propagator mass fit

The charged current cross section depends on the two EW parameters, the coupling constant(G_F) and the mass of the W-boson(M_W),

$$\frac{d\sigma}{dQ^2} \propto {G_F}^2 \cdot \left(\frac{{M_W}^2}{{M_W}^2 + Q^2}\right)^2. \tag{8.4}$$

Within the SM, these two parameters are related by one EW parameter of the weak mixing angle$(\sin\theta_W)$.

[1] If we use this modified PDF for the bin centering correction, the cross sections will be raised by 2.5% in the second highest x bin and by 5% in the highest x bin. The effect on the acceptance correction is negligible.

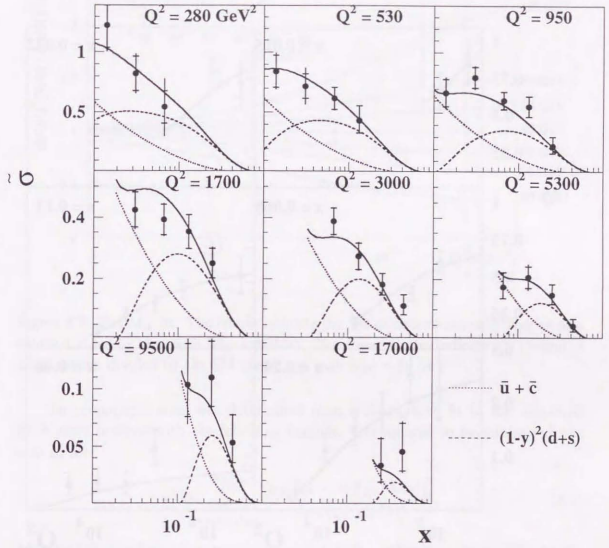

Figure 8.5: Measured reduced cross section as a function of x at fixed Q^2 points. The open closed circles indicate the data and the solid lines indicate the SM prediction with CTEQ4D PDF. The contributions from $\overline{u}+\overline{c}$ densities and from $(1-y)^2(d+s)$ densities, which are calculated with CTEQ4L PDF, are presented in dotted and dashed lines for illustration, respectively.

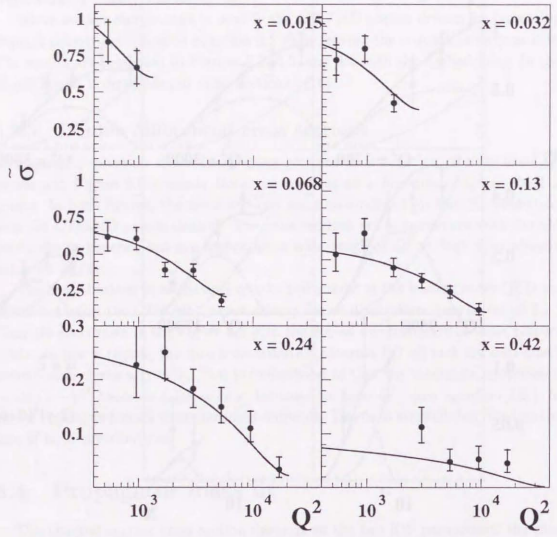

Figure 8.6: Measured reduced cross section as a function of Q^2 at fixed x points. The open closed circles indicate the data and the solid lines indicate the SM prediction with CTEQ4D PDF.

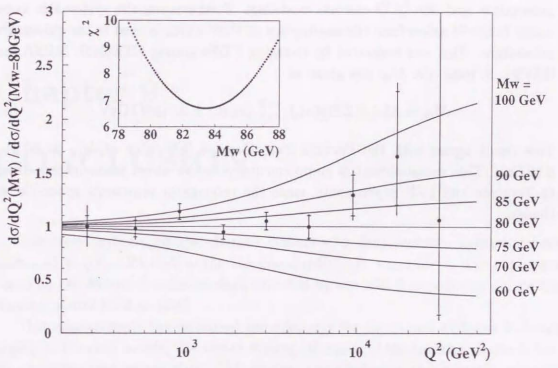

Figure 8.7: The M_W fit. The curves indicate the SM cross sections with various M_W values divided by that with $M_W = 80\,\text{GeV}$. The closed circles indicate the measured cross section divided by the SM prediction with $M_W = 80\,\text{GeV}$.

The propagator mass was determined from a chi-squared fit to the measured Born cross sections with the following manner. Chi-squared to be minimized was defined as:

$$\chi^2 \equiv \sum_{i=1\text{st-}Q^2\text{bin}}^{9\text{th-bin}} \frac{\left(\sigma_{BORN} - \sigma^{SM}_{BORN}(M_W)\right)^2_i}{\left(\delta\sigma_{BORN}(stat.)\right)^2_i}. \tag{8.5}$$

M_W was left as a free parameter in calculation of the SM cross section while the G_F was fixed to the Particle Data Group's [67] value($1.16639 \times 10^{-5}\,\text{GeV}^{-2}$).

Figure 8.7 represents the sensitivity of the fit. The curves indicate the SM cross sections calculated with different M_W values divided by that calculated with $M_W = 80\,\text{GeV}$. The closed circles indicate the measured cross sections divided by the SM prediction with $M_W = 80\,\text{GeV}$. The inset in Figure 8.7 shows the chi-squared calculated with different M_W. The statistical error of the fit was given by seeing how much M_W is altered so that the chi-squared is increased by unity from its minimum value. To evaluate the effect from the systematic errors in the cross section measurement, the fit was repeated with shifting the cross section values by the size

of the systematic errors. This was done each for the sources of the energy scale uncertainty and the QCD cascade modeling. Furthermore, the systematic uncertainty in the fit arises from the assumption of PDF which is used in the chi-squared calculation. This was evaluated by changing PDFs among CTEQ4D, MRSA, and GRV94. In total, the M_W was given as:

$$M_W = 83.4 \pm 2.8(stat.)\ ^{+1.6}_{-2.1}\ (syst.) \pm 2.7(pdf)\,\mathrm{GeV}. \tag{8.6}$$

This result agrees with the Particle Data Group's [67] value of $M_W = 80.41 \pm 0.10\,\mathrm{GeV}$. This measurement is complementary to the direct mass measurements at Tevatron and LEP experiments, since the propagator represents space-like exchange.

Chapter 9

CONCLUSION

The cross sections for the charged current e^+p deep inelastic scattering were measured at $\sqrt{s} = 300\,\mathrm{GeV}$ in the kinematic region $Q^2 > 200\,\mathrm{GeV}^2$. The analysis is based on the $46.6\,\mathrm{pb}^{-1}$ collision data collected by the ZEUS experiment during the running period 1994 to 1997.

This measurement has improved the efficiency for the events with low hadronic angle(γ). For such events, the vertex finding efficiency of the tracking device is low. By reconstructing vertex with CAL timing, the resolution of kinematic variables was kept moderate. At the same time, tighter background rejection algorithm was developed.

In total, 1088 events were selected as the final candidates. The background contamination was estimated to be at most 2-3% in all kinematic regions except for the lowest Q^2 region, where 10% order contamination was expected. The main backgrounds in the region were photoproduction events, which are the ep interaction with very low Q^2.

The single differential cross sections $d\sigma/dQ^2$, $d\sigma/dx$, and $d\sigma/dy$ were measured. The $d\sigma/dx$ and $d\sigma/dy$ are defined with $Q^2 > 200\,\mathrm{GeV}^2$. The statistical errors are typically less than 10%. The systematic errors are smaller than the statistical errors in all regions except for the lowest Q^2 region in $d\sigma/dQ^2$ measurement. The major contribution was from the energy scale uncertainty of the calorimeter. Compared with our previous measurement [30], both the statistical and systematic errors were reduced in this measurement. In addition, the explored kinematic region has been extended to high Q^2 and high x. The maximum Q^2 among the final candidates exceeded 40000 GeV^2 and $d\sigma/dQ^2$ was measured up to $Q^2 = 30000\ \mathrm{GeV}^2$. The $d\sigma/dx$ was measured up to $x = 0.65$ largely owning to the improvement of efficiency to the low γ region.

The double differential cross sections in terms of x and Q^2, $d^2\sigma/dxdQ^2$, were measured. The statistical errors are typically 15%. The systematic errors are smaller than the statistical errors in almost all kinematic region. This is the first measurement for the e^+p charged current interaction. In addition, this kinematic

region($Q^2 > 200\,\mathrm{GeV}^2$) has never been explored either by the fixed-target neutrino-beam experiments.

The measured cross sections were compared with the Standard Model predictions obtained using the CTEQ4D, MRSA, and GRV94 parton densities(PDFs). These PDFs were evolved according to the Next-to-Leading-Order(NLO) QCD DGLAP equation. The cross sections were consistent with the predictions except for the high x region, $x > 0.1$. The $d\sigma/dx$ exhibited an excess at $x > 0.1$ and the $d^2\sigma/dxdQ^2$ exhibited an excess at high x in a wide range of Q^2.

The charged current e^+p cross section is dominated by the d-quark contribution at high x. On the other hand, the measurements for high x in the low energy fixed target experiments are mainly sensitive to u-quark. The deviation observed at high x suggests that the d-quark at high x may be too underestimated in the current parton densities. This was also suggested from recent re-analyses of low Q^2 data [69, 70].

The propagator mass was extracted from the measured $d\sigma/dQ^2$ as $M_W = 83.4 \pm 2.8(stat.)\ ^{+1.6}_{-2.1}\ (syst.) \pm 2.7(pdf)\,\mathrm{GeV}$. The value was in agreement with the direct mass measurement at LEP and Tevatron.

Acknowledgments

It is a great pleasure to express my sincere gratitude to Prof. S. Yamada. I thank him for giving me the opportunity to study in this field. Special thanks are due to Prof. K. Tokushuku and Dr. M. Kuze for their guidance, discussions, valuable advice, and reading and correcting on this manuscript. I thank Dr. Y. Yamazaki for his guidance and advice.

I sincerely express my thanks to all members of the ZEUS collaborators. I thank Prof. A. Caldwell and Prof. S. Schlenstedt for their coordination and giving me the opportunity. Many thanks are for the charged current analysis team. I thank Mr. A. V. Sighem, Prof. K. Long, and Mr. R. Pawlak for the powerful collaboration. I thank Dr. F. Zarnecki for his support and thank Dr. G. Howell and Dr. M. Martinez for their pioneering study. I thank the Editorial Board members for the charged current paper, Prof. J. F. Martin, Prof. F. Sciulli, Prof. G. Wolf, Prof. G. Iacobucci, and Prof. B. Foster for their many valuable advice, useful suggestions and discussions. Also, many thanks are due to the neutral current analysis team, Dr. A. Quadt, Dr. J. G. Knetter, Dr. J. Edmonds, Dr. D. Williams, Dr. B. Straub, and Prof. D. Acosta.

I thank members of the ZEUS-TOKYO group, Prof. R. Hamatsu, Prof. S. Kitamura, Dr. T. Tsurugai, Dr. Y. Iga, Dr. K. Homma, Dr. T. Matsushita, Dr. K. Yamauchi, Dr. I. Suzuki, Dr. I. Fleck, Mr. M. Inuzuka, Mr. K. Umemori, Mr. T. Abe, Mr. T. Fusayasu, Mr. T. Yamashita, Mr. T. Nishimura, and Mr. G. Sato.

Appendix A

Rejection of non-*ep* processes

Since we are requiring an imbalance of the energy measurement, we are also collecting a lot of "unphysical" events at the same time. These types of events are; cosmic-ray induced events, proton beam halo muon induced events, events with some calorimeter cells sparking. Rejection becomes much more difficult for these events overlapped with some other *ep* processes, e.g. photoproductions, low Q^2 NCs, or beam-gas interactions. In general, these "strange" events have un-naturally localized large energy deposit, usual due to one cell, owes almost all of the imbalance of the transverse energy, $\not\!\!E_T$. We fight with them at first by applying cleaning cuts to reject such localized energy deposits, and then by applying sophisticated rejection algorithm.

A.1 Cleaning cuts

Large spark cell especially overlapped with an *ep* process gives also a large $\not\!\!E_T$, and would become backgrounds. The spark phenomena of the cell is due to a discharge of one of PMTs, and it gives a large energy imbalance measured between two PMTs, as a result. We already removed *isolated* cells with bad energy imbalance between two PMTs in the $\not\!\!E_T$ calculation, as described in the chapter 4. Remaining spark-induced events are: the spark cell is in some calorimeter activity, or, the other PMT than the spark PMT was dead. To remove further these contributions, $\not\!\!E_T$ is re-calculated excluding *all* of cells with bad imbalance between two PMTs and with a dead PMT. Requirement is as:

$$0.5 \leq \not\!\!E_T{}^{good}/\not\!\!E_T \leq 2.0, \tag{A.1}$$

where $\not\!\!E_T{}^{good}$ is the re-calculated one.

Muons of cosmic rays or beam-halos usually give signals of minimum ionized particles(*mip*) in the calorimeter, however, possibly happen to give a large energy deposits. These types of backgrounds will give more localized energy deposits in the

calorimeter, which gives us in turn a way to reject them as:

$$E^{HAC}_{BCAL}/E_{BCAL} \leq 0.9 \; .or. \; E_{BCAL} < 5\text{GeV}, \tag{A.2}$$
$$E^{HAC}_{RCAL}/E_{RCAL} \leq 0.9 \; .or. \; E_{RCAL} < 5\text{GeV}, \tag{A.3}$$

where E^{HAC}_{BCAL} denotes the energy deposited in the HAC sections of the BCAL, as same as for E^{HAC}_{RCAL} for RCAL.

The cell with the maximum transverse energy among all cells, which will be denoted as the *highest E_T cell*, is required not to be owning too much of the total transverse energy, based on the same idea:

$$E_{T^{cell}}^{MAX}/E_T < \begin{cases} 0.8 & \text{EMC} \\ 0.7 & \text{HAC} \end{cases} \tag{A.4}$$

$$\not\!\!E_T(-_{cell}^{MAX})/\not\!\!E_T > \begin{cases} 0.2 & \text{EMC} \\ 0.3 & \text{HAC} \end{cases} \tag{A.5}$$

where $E_{T^{cell}}^{MAX}$ is the transverse energy of the highest E_T cell, and $\not\!\!E_T(-_{cell}^{MAX})$ is a $\not\!\!E_T$ calculated excluding the highest E_T cell. The threshold is different if the highest E_T cell is a EMC or HAC cell.
The island energy which the highest E_T cell belongs is denoted as: $E_{T^{cell}}^{MAX}(island)$, and is required as:

$$E_{T^{cell}}^{MAX}/E_{T^{cell}}^{MAX}(island) < \begin{cases} 0.95 & \text{EMC, if the one of PMTs is dead, or overflown.} \\ 0.90 & \text{HAC} \end{cases} \tag{A.6}$$

When the highest E_T is a EMC cell, this requirement is limited to be applied only in case that one of the PMTs of the cell is dead or overflown.

A.2 Calorimeter timing cuts

Some of the non-*ep* backgrounds may give a timing measurement which is inconsistent with the *ep* collision.

The calorimeter timing is calculated from the PMTs with energy greater than 200 MeV. The number of PMTs used in the timing calculation is denoted as N_F, the sum of the energies of the used PMTs as E_F, and the measured timing is denoted as t_F in the followings for the FCAL measurement; i.e. the lower suffix denotes the calorimeter sections, B is at BCAL, R is at RCAL and G is at all calorimeters.

The cosmic rays usually shower from upward of the detector; it is useful to make timing measurement separately in upper and lower parts of the calorimeters. Time measured at the upper halve is denoted as: t^U_F, and the one at the lower halve is as: t^D_F, for example for the FCAL measurement.

We applied the timing cuts to be consistent with *ep* collisions as:

$$|t_F| < 6\,\text{nsec} \quad .or. \quad N_F < 2 \quad .or. \quad E_F < 0.6\,\text{GeV} \tag{A.7}$$
$$|t_F| < 5\,\text{nsec} \quad .or. \quad N_F < 2 \quad .or. \quad E_F < 10\,\text{GeV} \tag{A.8}$$
$$|t_B| < 6\,\text{nsec} \quad .or. \quad N_B < 2 \quad .or. \quad E_B < 0.6\,\text{GeV} \tag{A.9}$$
$$|t_B| < 5\,\text{nsec} \quad .or. \quad N_B < 2 \quad .or. \quad E_B < 10\,\text{GeV} \tag{A.10}$$
$$|t_R| < 6\,\text{nsec} \quad .or. \quad N_R < 2 \quad .or. \quad E_R < 0.6\,\text{GeV} \tag{A.11}$$
$$|t_R| < 5\,\text{nsec} \quad .or. \quad N_R < 2 \quad .or. \quad E_R < 10\,\text{GeV} \tag{A.12}$$
$$|t_G| < 6\,\text{nsec} \quad .or. \quad N_G < 2 \quad .or. \quad E_G < 2\,\text{GeV} \tag{A.13}$$
$$|t_G| < 5\,\text{nsec} \quad .or. \quad N_G < 2 \quad .or. \quad E_G < 10\,\text{GeV} \tag{A.14}$$
$$|t_G^U| < 6\,\text{nsec} \quad .or. \quad N_G^U < 2 \quad .or. \quad E_G^U < 10\,\text{GeV} \tag{A.15}$$
$$|t_G^D| < 6\,\text{nsec} \quad .or. \quad N_G^D < 2 \quad .or. \quad E_G^D < 10\,\text{GeV} \tag{A.16}$$
$$|t_F^U| < 6\,\text{nsec} \quad .or. \quad N_F^U < 2 \quad .or. \quad E_F^U < 10\,\text{GeV} \tag{A.17}$$
$$|t_F^D| < 6\,\text{nsec} \quad .or. \quad N_F^D < 2 \quad .or. \quad E_F^D < 10\,\text{GeV} \tag{A.18}$$
$$|t_F - t_R| < 6\,\text{nsec} \quad .or. \quad min.(N_F, N_R) < 2 \quad .or. \quad min.(E_F, E_R) < 1\,\text{GeV} \tag{A.19}$$
$$|t_G^U - t_G^D| < 6\,\text{nsec} \quad .or. \quad min.(N_G^U, N_G^D) < 2 \quad .or. \quad min.(E_G^U, E_G^D) < 1\,\text{GeV} \tag{A.20}$$
$$|t_F^U - t_F^D| < 6\,\text{nsec} \quad .or. \quad min.(N_F^U, N_F^D) < 2 \quad .or. \quad min.(E_F^U, E_F^D) < 1\,\text{GeV} \tag{A.21}$$
$$|t_R^U - t_R^D| < 6\,\text{nsec} \quad .or. \quad min.(N_R^U, N_R^D) < 2 \quad .or. \quad min.(E_R^U, E_R^D) < 1\,\text{GeV} \tag{A.22}$$

A.3 Barrel and Rear Muon Chamber cuts

Tracks reconstructed in the Barrel and Rear Muon Chambers are examined as if these are due to cosmic rays in a following manner.

All possible pairs of BRMU tracks are at first examined if they are due to single passing cosmic ray, if two or more tracks are reconstructed in the chambers. By connecting the two hit points each of which belongs to each track, the possible *cosmic line* is defined. An event is examined if it is due to a cosmic ray passing along the cosmic line. Followings are the criteria. The distance of the two hit points is evaluated by the angle distance between two hit points of a and b as:

$$\theta_{a-b} > 0.5 \text{ radian}, \tag{A.23}$$

where θ_{a-b} is the opening angle between the two points measured from the origin of the coordinate. The angle between the direction of the track measured by the BRMU chambers and the direction of the cosmic line is denoted as: θ_a and θ_b for the point a and b, respectively. And, the closest approach distance of the highest E_T cell to the cosmic line is denoted as: $D_{cell}^{MAX}(cosmicline)$. Events are rejected if

they satisfy *either of* the following two conditions:

$$\theta_a < 0.1 \text{ radian} \quad .and. \quad \theta_b < 0.1 \text{ radian} \tag{A.24}$$
$$D_{cell}^{MAX}(cosmicline) \quad < \quad 35\,\text{cm}. \tag{A.25}$$

Next, each BRMU tracks is extrapolated to be examined if it is due to a cosmic ray. The track is extrapolated from the hit point along the direction measured by the BRMU chambers passing through the calorimeter. The line is referenced also here as the cosmic line. The calorimeter cells which have closest distance of less than 35 cm to the cosmic line are regarded to belong the line. $\not{E}_T$, which is calculated only from the cells that belong to the cosmic line, is denoted as $\not{E}_T{}^{line}$. Events are regarded to be possibly induced by a cosmic ray if it satisfy the following condition at first, and will be examined in more detail further:

$$\not{E}_T{}^{line}/\not{E}_T{}^{line} \quad > \quad 0.8, \tag{A.26}$$
$$\Delta\phi_{\not{P}_T{}^{line}-\not{P}_T{}^{line}} \quad < \quad 12\,\text{degree}, \tag{A.27}$$

$\Delta\phi_{\not{P}_T{}^{line}-\not{P}_T}$ is an angle difference in ϕ between directions of $\not{E}_T{}^{line}$ and $\not{E}_T$. Then, if the closest approach of the interaction vertex to the cosmic line D_{vtz}^{line} is greater than 100 cm, the event is rejected as cosmic-ray induced;

$$D_{vtz}^{line} > 100\,\text{cm}. \tag{A.28}$$

Other events with $D_{vtz}^{line} < 100\,\text{cm}$ are examined more carefully. The calorimeter is divided in upper and lower with the plain which is defined with the interaction vertex and the cosmic line as the direction. The upper is defined as the one which includes the hit point of the BRMU track. The energy sum of the cells which belong to the cosmic line is calculated separately in upper and lower; denoted as E_{line}^{up} and E_{line}^{down} respectively. Events are rejected if:

$$E_{line}^{down} > E^{up}. \tag{A.29}$$

Even when above condition is not satisfied, the events are rejected if the following condition is satisfied:

$$E_{line}^{down} \quad > \quad 1.0\,\text{GeV}, \tag{A.30}$$
$$E_{out}^{down} \quad < \quad 0.5\,\text{GeV}, \tag{A.31}$$

where E_{out}^{down} is the energy sum of the cells which have closest approach distance to the cosmic line of less than 70 cm, but larger than 35 cm; i.e. do not belong to the cosmic line.

A.4 Hit pattern recognition in the calorimeter

Halo-mu induced events have a peculiar hit pattern in the calorimeter; the energy deposits align like a straight line along the z direction. The halo-muons passing through the BCAL are searched with the following criteria. Transverse of the energy deposits in the BCAL are summed up at first in the z direction separately for each section of EMC, HAC1 and HAC2 for each module. The unit of this division is called as z-tower, and the transverse energy of the z-tower is denoted as $E_T^{z-tower}$. If the maximum of $E_T^{z-tower}$ is large enough, and the z-tower is examined if it has a successive energy deposit-e structure in the z-direction as:

$$E_T^{z-tower} > 5\,\mathrm{GeV}, \tag{A.32}$$

$$N_{hit}^{z}/N_{tower}^{z} < 0.7, \tag{A.33}$$

where the N_{tower}^{z} is the total number of BCAL towers in z-direction, i.e. 32. The N_{hit}^{z} is the number of the towers which have energy deposits, however is scaled by 2.5 for EMC z-towers.

The cosmic rays passing through the calorimeter also give typical energy deposit pattern of aligning on a straight line. Starting from the highest E_T cell, a cluster is made by merging surrounding cells if they have energy deposits. The shape of this cluster is examined as a straight line, and the event is rejected the cluster is recognized to have line shape, if the highest E_T cell is in the FCAL or RCAL. The examination is done in two-dimension, while the clustering is done in three-dimension. The line is defined by connecting the position of the cells which have maximum and minimum of y coordinate values. The degree of straight line L_{clust} is defined as:

$$L_{clust} \equiv \frac{1}{2} \times \frac{D^{max}}{L_{clust}^{line}}, \tag{A.34}$$

where D^{max} is the maximum of closest distance to the line among all the cells in the cluster, and L_{clust}^{line} is the length of the line. Events are rejected if:

$$L_{clust} < \begin{cases} 0.05 & D_{BP} \\ 0.10 & D_{BP} \end{cases} \tag{A.35}$$

where D_{BP} is the closest approach distance to the Beam Pipe from the line.

Bibliography

[1] See e.g. F. Halzen and A. D. Martin, *Quarks and Leptons: An Introductory Course in Modern Particle Physics*, John Wiley & Sons, 1984.

[2] S. L. Glashow, Nucl. Phys. **22**(1961) 579,
S. Weinberg, *Phys. Rev. Lett.* **19**(1967) 1264.

[3] M. Gell-Mann, Phys. Lett. **8**(1964) 214.

[4] R. W. McAllister and R. Hofstadter, *Phys. Rev.* **102**, (1969) 851

[5] E. D. Bloom *et. al*, *Phys. Rev. Lett.* **23**(1969) 930,
M. Breidenbach *et. al*, *Phys. Rev. Lett.* **23**(1969) 935,
G. Miller *et. al*, *Phys. Rev.* D **5**(1972) 528.
A well-summarized write up is found e.g. J. Friedman, *The Rise of the Standard Model*, Cambridge Univ. Press 1997.

[6] J. D. Bjorken, Phys. Rev. **179**(1969) 1547.

[7] C. G. Callan and D. J. Gross, *Phys. Rev. Lett.* **22**(1969) 156.

[8] Gargamelle Collaboration, F. J. Hasert *et al.*, *Phys. Lett.* B **46**(1973) 121.

[9] BCDMS Collaboration, A. C. Benvenuti *et al.*, *Phys. Lett.* B **223**(1989) 485.

[10] NMC Collaboration, M. Arneodo *et al.*, *Phys. Lett.* B **364**(1995) 107,
NMC Collaboration, M. Arneodo *et al.*, *Nucl. Phys.* B **483**(1997) 3.

[11] E665 Collaboration, M. R. Adams *et al.*, *Phys. Rev.* D **54**(1996) 3006.

[12] CDHS Collaboration, H. Abromawicz *et al.*, *Z. Phys.* C **25**(1989) 29.

[13] CDHSW Collaboration, J. P. Berge *et al.*, *Z. Phys.* C **49**(1991) 187.

[14] CCFR Collaboration, R. Blair *et al.*, *Phys. Rev. Lett.* **51**(1983) 343,
CCFR Collaboration, P. S. Auchinloss *et al.*, *Z. Phys.* C **48**(1990) 411.

[15] CCFR Collaboration, E. Oltman *et al.*, *Z. Phys.* C **53**(1992) 51.

[16] BEBC Collaboration, G. T. Jones *et al.*, *Z. Phys.* C **62**(1994) 575.

[17] G. Wolf, DESY-preprint 94-022.

[18] H. Abramowics and A. C. Caldwell, *HERA Physics*, submitted to *Reviews of Modern Physics*.

[19] H1 Collaboration, T. Ahmed *et al.*, *Nucl. Phys.* B **439**(1995) 471

[20] ZEUS Collaboration, M. Derrick *et al.*, *Z. Phys.* C **65**(1995) 379

[21] H1 Collaboration, C. Adloff *et al.*, *Z. Phys.* C **74**(1997) 191

[22] ZEUS Collaboration, J. Breitweg *et al.*, *Z. Phys.* C **74**(1997) 207

[23] See e.g. G. Altarelli, J. Ellis, G. F. Giudice, S. Lola, and M. L. Mangano, hep-ph/9703276.

[24] G. Altarelli, G. F. Giudice, and M. L. Mangano, hep-ph/9705287.

[25] V. Barger, K. Cheung, K. Hagiwara, and D. Zeppenfeld, *Phys. Lett.* B **404**(1997) 147.

[26] T. Kon, T. Matsushita, and T. Kobayashi, *Modern Physics Letters A*, Vol. 12, No. 40(1997) 3143

[27] See e.g. M. Strovink, summary of RENCONTRES de MORIOND '98 QCD, hep-ex/9808004.

[28] H1 Collaboration, T. Ahmed *et al.*, *Phys. Lett.* B **324**(1994) 241

[29] H1 Collaboration, S. Aid *et al.*, *Z. Phys.* C **67**(1995) 565

[30] ZEUS Collaboration, M. Derrick *et al.*, *Z. Phys.* C **72**(1996) 47

[31] H1 Collaboration, S. Aid *et al.*, *Phys. Lett.* B **379**(1996) 319

[32] ZEUS Collaboration, M. Derrick *et al.*, *Phys. Rev. Lett.* **75**(1995) 1006

[33] F. E. Close, *An Introduction to Quarks and Partons*, Academic Press, 1979.

[34] A. M. Cooper-Sarkar, R. Devenishi, and A. de Roeck, *Int'l J. Mod. Phys.* A13(1998) 3385.

[35] V. N. Gribov and L. N. Lipatov, Sov. J. Nucl. Phys. **15**(1972) 438,
Y. L. Dokshitzer, Sov. J. Nucl. Phys. **46**(1977) 641,
G. Altarelli and G. Parisi, *Nucl. Phys.* B **126**(1977) 298.

[36] ZEUS Collaboration, The ZEUS Detector, Status Report 1993, DESY, 1993.

[37] K. Piotrzkowski and M. Zachara, ZEUS Note 94-167,
K. Piotrzkowski and M. Zachara, ZEUS Note 95-138.

[38] G. Schuler and H. Spiesberger, in *Physics at HERA*, Vol.3,(1991) 1419.

[39] G. Ingelman, in *Physics at HERA*, Vol.3,(1991) 1366.

[40] H. Spiesberger, HERACLES version 4.5.2. unpublished program manual,
A. Kwiatowski, H. Spiesberger and H. J. Moehring in *Physics at HERA*, Vol.3(1991) 1294,
A. Kwiatowski, H. Spiesberger and H. J. Moehring, *Z. Phys.* C **50**(1991) 165.

[41] PDFLIB: a CERN library package.
H. Plothow-Besch, Comput. Phys. Commun. **75**(1993) 396.

[42] L. Lönnblad, Comput. Phys. Commun. **71**(1992) 15,
L. Lönnblad, *Z. Phys.* C **65**(1995) 285.

[43] T. Sjöstrand, Comput. Phys. Commun. **82**(1994) 74.

[44] R. Brun *et al.*, GEANT 3.13, CERN DD/EE/84-1.

[45] H. L. Lai *et al.*, *Phys. Rev.* D **55**(1997) 1280.

[46] G. Wolf, DESY-preprint 97-047.

[47] A. Quadt and O. Ruske, ZEUS internal note.

[48] G. Marchesini *et al*, Comput. Phys. Commun. **67**(1992) 465.

[49] J. A. M. Vermaseren, *Nucl. Phys.* B **229**(1983) 347.

[50] U. Baur, J. A. M. Vermaseren, D. Zeppenfeld, *Nucl. Phys.* B **375**(1992) 3.

[51] ZEUS collaboration, M. Derrick *et al.*, *Phys. Lett.* B **316**(1993) 412

[52] ZEUS collaboration, *Measurement of High Q^2 Charged-Current e^+p Deep Inelastic Scattering Cross Sections at HERA*, in preparation.

[53] R. Pawlak, ZEUS-Note 98-040
R. Pawlak, private communication.

[54] F. Jacquet and A. Blondel,
Proc. of the study for an *ep* facility for Europe, DESY 79-48(1979) 391.

[55] ZEUS collaboration, *Measurement of High Q^2 Neutral-Current e^+p Deep Inelastic Scattering Cross Sections at HERA*, in preparation.

[56] S. M. Wang, ZEUS-Note 96-121

[57] G. Briskin, Ph.D. thesis, Tel Aviv University 1998.

[58] J. G. Knetter, ZEUS-Note 98-031.
J. G. Knetter, private communication.

[59] J. Edmonds, J. G. Knetter and A. Quadt, ZEUS-Note in preparation.
J. G. Knetter, private communication.

[60] H. Abramowicz, A. Caldwell, and R. Sinkus, *Nucl. Instrum. Methods* A **365**(1995) 508

[61] S. Catani, Yu. L. Dokshitzer, M. H. Seymour and B. R. Webber, *Nucl. Phys.* B **406**(1993) 187,
S. D. Ellis and D. E. Soper, *Phys. Rev.* D **48**(1993) 3160.

[62] ZEUS Collaboration, M. Derrick *et al*, *Phys. Lett.* B **315**(1993) 481

[63] See e.g. A. Levy, *Low-x physics at HERA*, DESY pre-print 97-013.

[64] A. D. Martin, R. G. Roberts, and W. J. Stirling, *Phys. Rev.* D **51**(1995) 4756

[65] M. Glück, E. Reya, and A, Vogt, *Z. Phys.* C **67**(1995) 433

[66] HECTOR program manual; DESY-preprint 95-185.

[67] Particle Data Group, C. Caso *et. al*, Euro. Phys. J. **C3**(1998) 1.

[68] M. Botje, program QCDNUM,
ZEUS Collaboration, Abstract 770 submitted to the XXIX Int. Conf. on High Energy Physics, Vancouver(1998).

[69] W. Melnitchouk and A. W. Thomas, *Phys. Lett.* B **377**(1996) 11,
W. Melnitchouk and J. C. Peng, *Phys. Lett.* B **400**(1997) 220.

[70] U. K. Yang and A. Bodek, hep-ph/9809480, submitted to *Phys. Rev. Lett.*